Fakultät für Elektrotechnik und Informationstechnik
Technische Universität München

Computer models of acoustical and electrical stimulation of neurons in the auditory system

Marek Rudnicki

Vollständiger Abdruck der von der Fakultät für Elektrotechnik und Informationstechnik der Technischen Universität München zur Erlangung des akademischen Grades eines Doktor-Ingenieurs genehmigten Dissertation.

Vorsitzender:
Prof. Dr.-Ing. Sami Haddadin

Prüfende der Dissertation:
1. Prof. Dr.-Ing. Werner Hemmert
2. Prof. Dr. Christian Leibold

Die Dissertation wurde am 26.06.2018 bei der Technischen Universtiät München eingereicht und durch die Fakultät für Elektrotechnik und Informationstechnik am 10.10.2018 angenommen.

Abstract

The main function of the ear is to convert sounds into electrochemical signals in the nervous system. Any disruption in this process causes hearing impairment or deafness. In particular, when the delicate sensory cells in the ear, the inner hair cells, are damaged by loud sound, infection, or drugs, then the auditory nerve is not stimulated and the flow of auditory information stops. However, if the auditory nerve is still functional, the hearing can be partially restored by a cochlear implant (CI), which stimulates the nerve electrically. The electrical stimulation of the nerves is not completely understood due to complex morphology and physiology of the neural tissue. Bilaterally implanted patients could benefit from better sound localization and improved "electrical" hearing in noisy conditions. Additionally, a better understanding of both synaptic and electrical stimulation could improve the future design of electro-acoustic CIs.

Chapter 2 of the thesis shows a multicompartment Hodgkin–Huxley-type auditory nerve fiber (ANF) model that can be stimulated synaptically and electrically. For the synaptic stimulation, the ANF model was combined with a biophysical model of an inner ear, where it replaced an artificial spike generator. The new hybrid model produced correct firing rates in response to acoustical stimuli. Unlike in the spike generators, the refractoriness emerged from the intrinsic membrane properties of the ANF model. The ANF model was also stimulated electrically with pulses of different shapes and rates, and successfully reproduced *in vivo* experiments. Finally, the model was used to simulate psychoacoustical experiments with CI patients and triphasic pulses. It explained how a local increase of the membrane capacitance (e.g. due to demyelination of the nerve or the unmyelinated soma), inverses the efficiency of the pulses with opposite polarities. Remarkably, all simulations were performed with the same model without any modification of its parameters.

Chapter 3 examines a part of the sound localization pathway by modeling globular bushy cells (GBCs) in the cochlear nucleus. GBCs are known for their temporally precise spiking, which is necessary for sound localization. They receive direct inputs from the ANFs through large synapses, endbulbs of Held, which show strong depression in *in vitro* experiments. However, when simulated with *in vitro*-like stimuli, the strongly depressing endbulbs could not drive the bushy cells to realistic firing rates. The study predicts that the majority of endbulbs have depression of less than 20 %, which is consistent with recent *in vivo* studies.

In summary, the thesis shows detailed models of the initial auditory pathway: inner hair cell synapse, auditory nerve fiber, endbulb of Held synapse, and globular bushy cell. It helps to better understand how auditory information is processed and transmitted to higher auditory centers. It also shows simulations of the electrical stimulation of the auditory nerve in *in vivo* and in psychoacoustic experiments. It explains effects observed in CI patients, which improves our understanding of the implants and might help to enhance them.

Contents

Glossary

2AFC two-alternative forced choice.

AC anodic-cathodic (biphasic pulse).

ACA anodic-cathodic-anodic (triphasic pulse).

ACE advanced combination encoder.

AN auditory nerve.

ANF auditory nerve fiber.

AP action potential.

BM basilar membrane.

BTE behind the ear.

CA cathodic-anodic (biphasic pulse).

CAC cathodic-anodic-cathodic (triphasic pulse).

CF characteristic frequency.

CI cochlear implant.

CIS continuous interleaved sampling.

CN cochlear nucleus.

EI entrainment index.

EPSC excitatory post-synaptic current.

EPSP excitatory post-synaptic potential.

FSP fine structure processing.

GBC globular bushy cell.

HRTF head-related transfer function.

HSR high-spontaneous rate.

IHC inner hair cell.

IPSP inhibitory post-synaptic potential.

ISIH inter-spike interval histogram.

LSR low-spontaneous rate.

MNTB medial nucleus of the trapezoid body.

MSR medium-spontaneous rate.

MTF modulation transfer function.

OHC outer hair cell.

PSTH peri-stimulus time histogram.

RMS root mean square.

SBC spherical bushy cell.

SG spiral ganglion.

SPEAK spectral peak.

SR spontaneous rate.

VCN ventral cochlear nucleus.

VS vector strength.

YXF09m is an endbulb of Held synapse model tuned to the mean data from Yang & Xu-Friedman (2009).

Chapter 1

General Introduction

In our daily life, we often forget that the major part of the perception of the world around us is derived from the sensory inputs. Sensory organs are particularly interesting, because they create the direct interface to the environment. When a sensory organ fails (causing blindness or deafness), the brain is isolated from the sensory input and a large portion of information about the environment is not available. Sensory organs are our only interface to the world and without them we are isolated from it.

In case of hearing, sensory transduction takes place in the inner ear and sensory information is further transmitted through the auditory nerve (AN) to the cochlear nucleus (CN) in the brainstem. Next, it travels further through the midbrain and thalamus up to the cerebral cortex. The auditory pathway is complicated with ipsi- and contralateral projections as well as feedback loops (Smith and Spirou 2002).

The auditory system is well described on different levels of organization (systemic, organ, tissues, and cellular) (Webster, Popper, and Fay 1992; Popper and Fay 1992). However, the interaction between the different levels is much less understood. For example, how does a given synaptic property influence an activity of a population of neurons in one of the auditory nuclei? Such questions might be difficult to answer, either because of difficulties in the measuring techniques (especially *in vivo*), or difficulties in changing of particular parameters in the biological system (e.g., pharmacologically or genetically). Computational modeling gives us the opportunity to bypass those difficulties and modify any parameter at will and to have access to all variables of the system. One of the main drawbacks of the virtual approach is a huge parameter space in biological models. However, knowing the constraints of systems helps to reduce the parameter space of even very complex systems to a manageable size (Markram 2006).

Why is it important to have detailed understanding of the auditory system? There are at least two strong reasons. First, the human auditory system has a remarkable performance as shown in Table 1.1. Understanding the secrets of hearing

Property	Value
Frequency range	20 Hz to 20 000 Hz
Dynamic range	>120 dB
Hearing threshold (at 1000 Hz)	4 dB re 20 µPa
Min. interaural time difference	10 µs

Table 1.1: Specifications of the human auditory system (Gelfand 2010).

might enable us to learn from them and engineer better communication systems. Second, if hearing fails because of aging or disease, the quality of life is severely reduced. "Blindness separates people from things; deafness separates people from people."[1] When vision fails, then we are separated from our environment. If hearing fails, then communication with other people breaks. Repairing the sensory pathway is not an easy task and requires very detailed mechanistic understanding of the hearing process. The knowledge of the problem enables directed work towards a solution.

Can computational modeling help with those issues? As Richard Feynman said "What I cannot create, I do not understand," I learned that this rule also applies to biological systems and modeling. The starting point of Chapter 3 were synapses carefully fitted to *in vitro* experiments. They were driven by realistic *in vivo*-like inputs and stimulated a bushy cell model. But when combined, the models did not produce realistic results. This unexpected outcome triggered a detailed investigation and challenged the "known" assumptions. As a result, a detailed analysis of the interaction between different synaptic parameters and the activity of the bushy cell was born. The analysis showed that synaptic parameters from *in vitro* studies might not always be used directly in *in vivo*-like conditions. The results are also consistent with more recent *in vivo* measurements.

In addition to the modeling study of bushy cells, Chapter 2 shows how a relatively simple models of an ANF and an electrode can explain phenomena observed in psychoacoustic experiments with patients provided with cochlear implants. It is quite remarkable, because the model links the morphology of the ANFs and a position of an electrode to effects that were found in a psychophysical experiments with cochlear implant users. Chapter 2 also shows that the same model can be used to describe synaptic and electric stimulation of the AN.

[1] Immanuel Kant

1.1 Structure of the Thesis

The main content of the thesis is located in mostly self-contained Chapters 2 (Modeling of Synaptic and Electrical Stimulation of Auditory Nerve Fibers) and 3 (Comparison of Globular Bushy Cell Models with Different Levels of Synaptic Depression in *in vivo*-like Simulations). Each chapter has its own specific introduction, methods, results, and discussion. Those main chapters are preceded by a general introduction (Chapter 1). The introduction provides the necessary foundations about the mammalian auditory system and computational neuroscience. If a reader has a basic knowledge in those fields, it is possible to skip the general introduction and start reading the two main chapters. Finally, Chapter 4 summarizes the main results and conclusion of the thesis.

1.2 The Cochlea

One of the main functions of the ear is to convert sounds to biochemical signals in the auditory nervous system. This process is necessary to enable hearing. In mammals, the ear can be divided into three parts: outer, middle, and inner ear. The structure of a human ear is shown in Figure 1.1.

The outer ear consists of the pinna and the ear canal. The function of the outer ear is to funnel sound from the environment and to conduct it into the middle ear. The pinna is the external and visible part. Its main function is to enhance the directional sensitivity. Due to the shape of the pinna, head and torso, sounds are amplified or attenuated depending on direction and frequency. This effect can be described by a head-related transfer function (HRTF), which is a set of linear filters for different directions of the sound source. Generally, there is a relatively large variability between individual HRTFs due to variation in size and shape of the pinna and the head. The ear canal is a tube of approximately 25 mm in length that conducts sounds from the pinna to the middle ear. Due to the quarter wavelength resonance in the ear canal (combined with the middle ear impedance), 2 kHz to 4 kHz is the most sensitive frequency range of the ear (Wiener and Ross 1946; Dillon 2001).

Next, there is the middle ear that consists of the tympanic membrane (also known as the eardrum), the ossicles, and two small muscles located in the tympanic cavity. The ossicles are three little bones named after three objects that they resemble: malleus (hammer), incus (anvil), and stapes (stirrup). The main function of the middle ear is to efficiently transfer the sound energy from the outer ear to the entrance of the inner ear, the oval window. This transfer requires impedance matching, because at the outer ear, sound propagates in air and in the cochlea it propagates in fluid. Without proper impedance matching, most of the sound energy

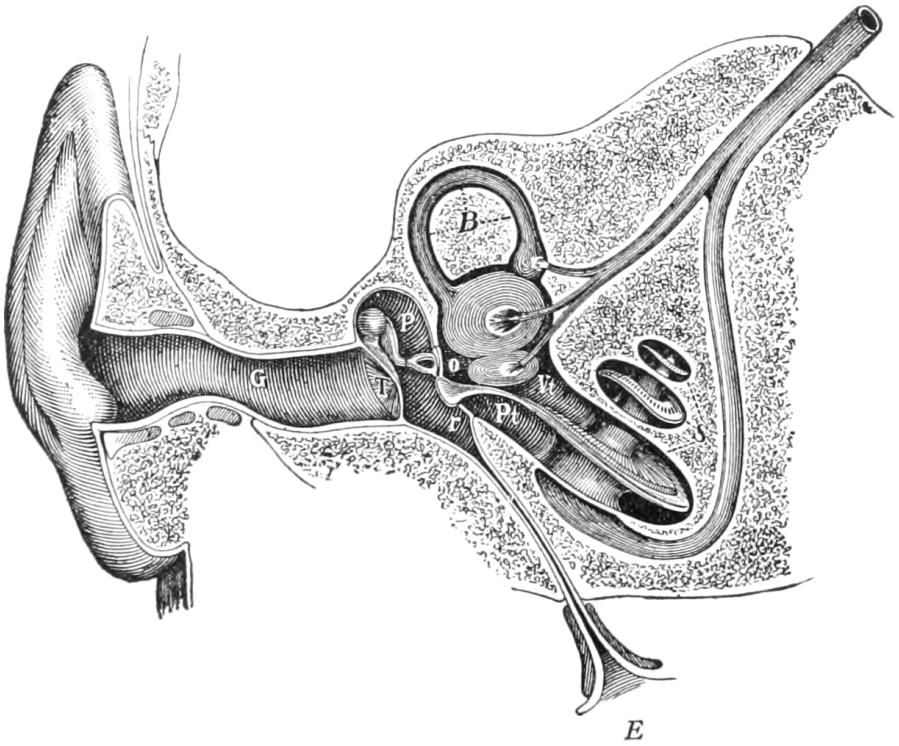

Figure 1.1: Cross section of the right human ear. **G** is the ear canal, **T** is the tympanic membrane, **P** is the tympanic cavity, **o** is the oval window, **r** is the round window, **B** marks the semicircular canals (part of the vestibular system), **S** is the cochlea, **Vt** is the scala vestibuli, **Pt** is the scala tympani, and **E** is the Eustachian tube. The drawing was adapted from Howell (1911).

would be reflected. The mechanical impedance matching is accomplished by a lever built from the ossicles, the difference in size between the tympanic membrane and the oval window, and the curvature of the eardrum. As a result, a small force and large movement at the tympanic membrane is converted to a smaller movement but larger force at the oval window. In addition to the acoustic impedance matching, the middle ear can attenuate excessively loud sounds with the two small muscles attached to the ossicles and protect the inner ear from damage. It is called the acoustic reflex. However, this attenuation is effective only up to 1 kHz. The delay of the reflex is also quite long (10 ms to 100 ms). Therefore, sounds with loud onsets can still get through and damage the delicate sensory organ in the inner ear.

The inner ear is the most sophisticated part of the ear. In mammals, it has two functional parts: auditory and vestibular. They are both innervated by the vestibulocochlear nerve (the eighth cranial nerve). The inner ear itself is enclosed by the bony labyrinth within the temporal bone, see Figure 1.1 and Figure 1.2 for more detail. The bony labyrinth is filled with fluid (perilymph) and a membranous structure called the membranous labyrinth. Let us focus on the cochlea, which is the auditory portion of the inner ear. The name "cochlea" comes from an ancient Greek word meaning snail shell and is describes its peculiar shape. Human cochlea is curved and makes approximately 2.75 turns around the modiolus. It is approximately 32 mm long and has a diameter of 2 mm. The cochlea contains three chambers (scalae) that run along it:

1. *scala vestibuli*, which begins at the oval window,
2. *scala tympani*, which begins at the round window, and
3. *scala media*, (*ductus cochlearis*, cochlear duct) that runs between the scala vestibuli and the scala tympani.

Figure 1.3 shows a cross section of a human cochlea. It captures five cross sections of the scalae due to 2.75 turns around the modulus. Furthermore, scala tympani and scala vestibuli merge at the apex of the cochlea. Scala media is completely separated from both scala vestibuli by Reissner's membrane (vestibular membrane) and from scala tympani by the basilar membrane (BM). Scala media is filled with endolymph, which differs chemically and electrically from perilymph. Most significantly, the endolymph has a high concentration of K^+. Scala media also contains the organ of Corti, which is the actual sensory organ of hearing. The organ of Corti sits on top of the BM.

The vibrations are coupled into the cochlea through the oval window into the fluid of scala vestibuli (perilymph). The movement of the perilymph causes vibrations of the membranes including the BM. The BM is not uniform along its length. At the base it is stiffer and narrower than at the apex. As a result,

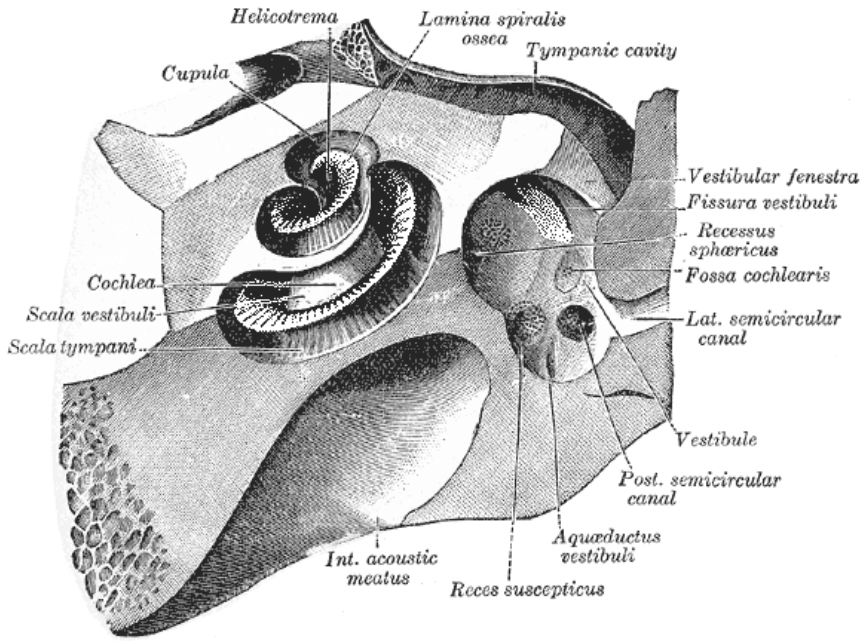

Figure 1.2: Bony and membranous labyrinth in the temporal bone. The cochlear and the vestibular parts are visible. The drawing was adapted from Gray (1918).

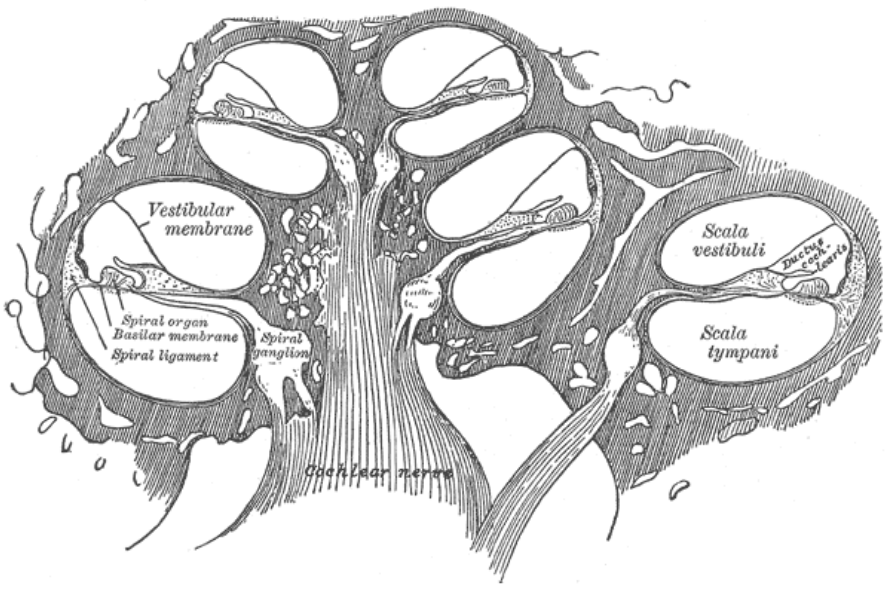

Figure 1.3: Cross section of the cochlea. The Rosenthal's canal was cut in five different places because of its spiral shape. The drawing was adapted from Gray (1918).

different portions of the membrane resonate with different sound frequencies. High frequencies cause strong vibrations at the base, while low frequency sounds cause vibrations at the apex. The vibration pattern of the BM is called the traveling wave and results in a spectral decomposition of sounds by the cochlea. The BM can be viewed as a filter bank, where each location along the membrane is associated with a different filter. The center frequency of that filter at low stimulus intensities is called characteristic frequency (CF). The mapping between stimulation frequencies and the position is called the "place code," and is the root cause of the tonotopic organization of the auditory system up to the auditory cortex.

The actual transduction of the mechanical vibrations to electrochemical signals happens at the organ of Corti. It is placed on the BM and contains hair cells that extend their stereocilia into the fluid filled scala media as shown in Figure 1.4. There are four rows of hair cells: one row of the inner hair cells (IHCs) and three rows of the outer hair cells (OHCs). The IHCs are the actual sensory cells. Generally, the motion of the BM and the associated organ of Corti causes stereocilia of the IHCs to move synchronously with the vibrations. A bundle of stereocilia is shown in Figure 1.5. Each hair cell has from 10 to 300 stereocilia and there are approximately 3500 IHCs in a human cochlea. The stereocilia are rigid because of actin filaments and bend only at the base. Additionally, they are connected to one another by extracellular tip link filaments (Figure 1.5). As a result, they do not move independently from each other but rather as a unit. The motion of the stereocilia and the stress of the tip links causes spring-gated ion channels located at the link site to open. K^+ ions from the endolymph can enter IHCs and depolarize their membrane. In short, the movement of the stereocilia depolarizes and hyperpolarizes membrane of the IHCs. On the basolateral side, the IHCs are contacted by the ANFs through the IHC ribbon synapses (Rutherford and Moser 2015). This is where the graded receptor potential of the IHCs is converted to discrete action potentials (APs) in the ANFs. The changes in the receptor potential influence the probability of the neurotransmitter release into the synaptic cleft. When released, the neurotransmitter in the synaptic cleft binds with receptors at the post-synaptic site and causes opening of the associated channels in the post-synaptic membrane of the the ANFs. The depolarization of the membrane in the spiral ganglion (SG) neurons initiates an AP, which propagates along the AN to the central nervous system. In summary, there are two key stages of the transduction of mechanical vibrations to the APs:

1. Conversion of the mechanical vibrations to graded receptor potential by the stereocilia.

2. Conversion of the graded receptor potential to APs at the IHC synapse.

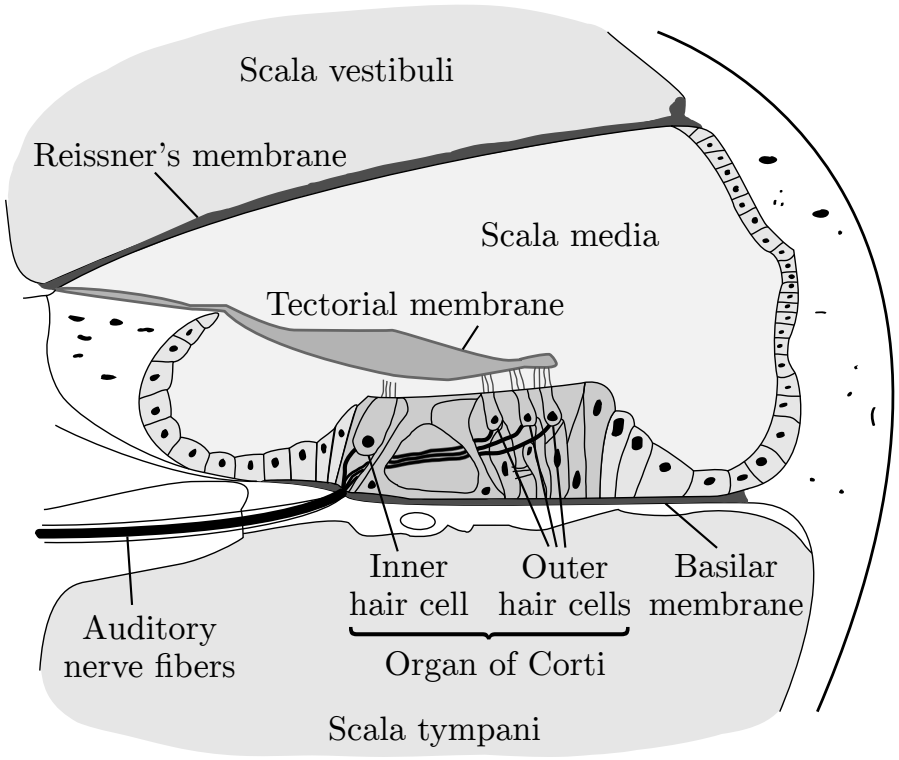

Figure 1.4: Cross section of the organ of Corti and the surrounding cochlear structures. Figure modified from *Cross section of the cochlea* by Oarih Ropshkow and Fred the Oyster, Wikimedia Commons, CC BY-SA 3.0.

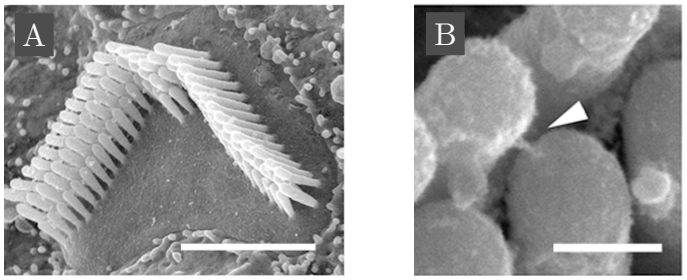

Figure 1.5: High resolution scanning electron microscope images of (A) stereocilia bundles and (B) a tip link on a hair cell. Scale bars correspond to 2 µm in panel (A) and to 200 nm in panel (B). Figure adapted from Hertzano et al. (2008).

The OHCs play a different role than IHCs. They are an essential part of the *cochlear amplifier*, which is a local feedback mechanisms that amplifies the vibration of the BM. The cochlear amplifier is responsible for an amplification of 35 dB to 58 dB and sharpening of the tuning of the BM filters (Robles and Ruggero 2001). The mechanical amplification by the OHC is possible because their membrane contains special motor proteins (prestin), which can change its length depending on the transmembrane voltage. As a result, the shape of the OHCs can actively change depending on the membrane potential, which is in turn modulated by movement of the stereocilia. The changes of the length due to prestin are very rapid and can follow the vibrations up to the highest audible frequencies (Frank, Hemmert, and Gummer 1999). It is crucial for the amplification that the OHCs are located between two membranes: basilar and tectorial. They sit on the BM and their stereocilia touch the tectorial membrane in scala media. Finally, because OHCs are not the actual sensory cells, they are only sparsely contacted by efferent nerve fibers.

1.3 Cochlear Implants

In a healthy cochlea sounds are converted to electrochemical signals by sensory cells known as the inner hair cells (IHCs). During the process of sensory transduction, the IHCs stimulate synaptically the AN. However, if the delicate IHCs are damaged, then the transduction stops and the AN remains mostly silent. As a result, an individual looses the ability to hear. The source of IHC damage can vary from genetic defects, infections, ototoxic drugs, to autoimmune disease, or trauma.

When all or almost all IHCs are damaged, but the AN remains mostly functional, the damage can by bypassed by a cochlear implant (CI) (Zeng, Popper, and Fay 2004; Wilson and Dorman 2008). It uses electrical impulses to stimulate the AN and elicit APs, which travel to the central nervous system. The stimulation can be perceived by patients and enables partial restoration of hearing. Figure 1.6 shows a drawing of an implanted CI device. It consists of an external part that is visible around the pinna and an internal that is implanted in the body. The stimulating electrodes belongs to the internal part and are inserted into the cochlea.

The function of the CI is to convert sounds into electrical signals and stimulate the AN. The sound conversion and stimulation should be done in a way that enables patients to comprehend the sensations and identify sounds. The performance of CIs varies a lot and is highly individual. Some patients can hardly discriminate any sounds and some excel in the performance. Overall, the majority of patients score above 80 % in contextual speech recognition and can, e.g., use a telephone (NIH Consens Statement 1995; Gifford, Shallop, and A. M. Peterson 2008).

Figure 1.7 shows a block diagram of a CI (Wilson 2004). The external part is

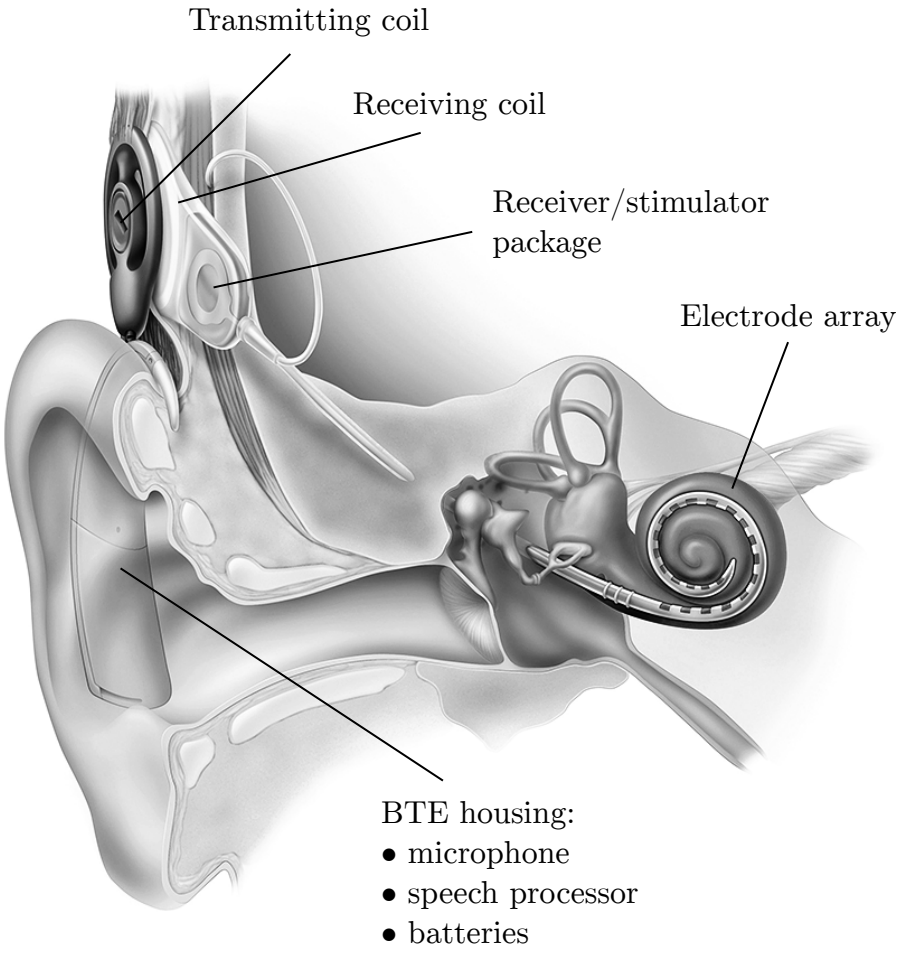

Figure 1.6: A realistic drawing of a human ear with a CI. Figure modified from *Cochleaimplantat.jpg*, Wikimedia Commons, CC BY-SA 3.0.

made of a microphone, a speech processor, external encoder, and a transmitting coil. The internal part is made of a receiving coil, a receiver, a decoder, a stimulator, a ground electrode, and an electrode array. A microphone is usually located close to the ear within the behind the ear (BTE) housing. Its function is to convert sound to an electrical signal. The BTE unit also contains a speech processor and batteries. The main function of the speech processor is to convert audio signal to patterns of electrical stimulation. Those patterns should retain relevant bits of information of the original signal and be compatible with the neural coding in the AN. The algorithm that does this conversion is often called a *coding strategy*. Next, the stimulation patterns are sent to the internal part of the CI by a radio transcutaneous link. It is made of transmitting and receiving coils. The transmitting (external) coil is mounted and aligned by a pair of magnets to the receiving (internal) coil. In modern CIs the transmission can be bidirectional, i.e., the speech processor can not only send but also receive signals from the implanted part of the device. The received signals can contain information about status of the receiver, impedance of the electrodes, and neural evoked potentials. The neural evoked potentials can help to asses the degradation of the AN. Finally, the stimulating electrodes are most frequently implanted in the scala tympani. The flexibility and the diameter of the electrode array should facilitate its insertion into the cochlea. The number of electrodes in the array is typically between 12 and 22 and depends on the CI model. The electrodes can be stimulated either in the monopolar or bipolar configurations. In the monopolar configuration, the reference electrode is a ground electrode that is remote to the cochlea. In the bipolar configuration, each electrode is stimulated with respect to one of its neighboring electrodes. The key consideration in the design and placement of the electrodes is to stimulate non-overlapping populations of the SG neurons with each electrode.

There can be different coding strategies implemented in the CIs. Some of them include: continuous interleaved sampling (CIS) (Wilson, Finley, et al. 1991), spectral peak (SPEAK) (Skinner et al. 1994), advanced combination encoder (ACE) (Kiefer et al. 2001), and n-of-m (Finley et al. 1988). As already mentioned, the tasks of a coding strategy is to convert an analog signal to a stimulation pattern that can be used to stimulate an AN and comprehended by a patient. For example, the CIS algorithm consist of the following steps:

1. The output of the microphone with an optional automatic gain control is connected to a preemphasis filter, which emphasizes consonants by attenuating frequencies below 1.2 kHz.

2. The pre-filtered signal is split into band-pass channels and each channels undergoes:

   (a) band-pass filtering,

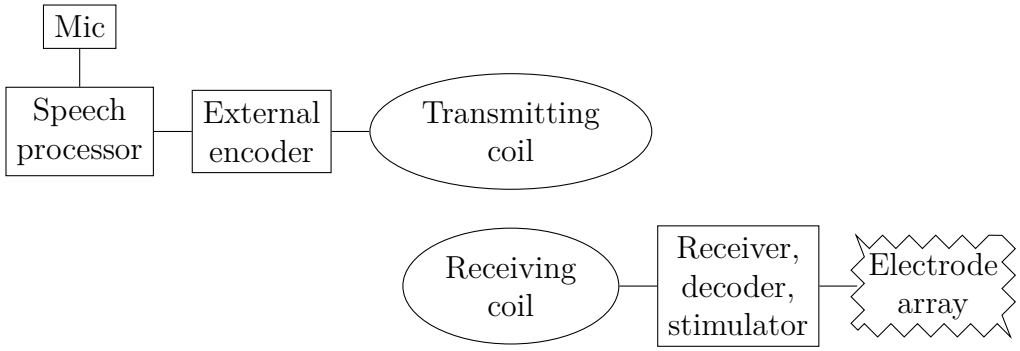

Figure 1.7: Block diagram of a CI. The external part of an implant consists of a microphone, speech processor, encoder, and a transmitting coil. The internal part of a CI consists of a receiving coil, receiver, decoder, stimulator, and an electrode array. (Wilson 2004)

   (b) envelope detection (low-pass filter or Hilbert transform),

   (c) compression.

3. The channel outputs modulate trains of biphasic pulses, which stimulate the electrodes. Low frequency channels are associated with apical electrodes, whereas the high frequency channels are associated with the basal electrodes. Such arrangement tries to preserve the tonotopic organization of the auditory system.

A key property of the CIS strategy is that the bipolar stimulating pulses are interleaved. As a result, no two electrodes are stimulated at the same time. It simplifies complex interaction of multiple stimulating electrodes with a neural tissue and prevents overstimulation. A typical pulse rates in the CIS strategy are 1000 pulses/s per electrode or higher.

Another property of the CIS strategy is that it encodes only the envelope of the sound and discards the fine temporal structure, which is important for pitch perception and sound localization. This fact is particularly important for bilaterally implanted patients that could localize sound better given a coding strategy that encodes the fine temporal structure. This problem is addressed by newer coding strategies such as fine structure processing (FSP) (Magnusson 2010).

1.4 Hodgkin–Huxley Neuron Model

Signals in the nervous system are propagated mainly by means of APs. They travel along the neurons' elongated projections—axons—as rapid changes in the membrane's electric potential. Hodgkin and Huxley (1952) described the mechanisms

underlying initialization and propagation of APs in the squid giant axon. Modified Hodgkin–Huxley models are commonly used to describe the behavior of neurons in different species. However, the main principles of operation remains the same in the original and modified Hodgkin–Huxley models (M. Nelson and Rinzel 2003).

Neurons, like other cells, are enclosed by a cell membrane which separates the inside of the cell from its environment. The cell membrane is a lipid bilayer with embedded proteins. By itself it makes a nearly perfect electrical insulator. However, ions can pass through some of the embedded proteins, which can be subdivided into ion pumps and ion channels. Ion pumps actively transport ions across the membrane utilizing energy. They maintain ion gradients across the membrane. Channels allow ions to diffuse back and diminish the gradients (Bear, Connors, and Paradiso 2007).

Due to the ion pumps, the concentration of potassium ions (K^+) is approximately 20 times higher inside the cell than in the extracellular liquid. The difference in concentration gives rise to a diffusion potential, which is called the Nernst potential or the reversal potential of K^+. The same happens for other ions, e.g., Na^+. Generally, the Nernst potential for an ion equals

$$E_{\text{ion}} = \frac{kT}{q} \ln \frac{[\text{ion}_o]}{[\text{ion}_i]}, \tag{1.1}$$

where k is the Boltzmann constant, T is the temperature, q is the charge of an ion, and $\text{ion}_o/\text{ion}_i$ is the ratio of ion concentrations outside and inside the cell. For K^+ the Nernst potential is approximately $-80\,\text{mV}$ at body temperature. For Na^+ it equals to $62\,\text{mV}$, because the Na^+ concentration inside the cell is smaller than outside. Similarly, the Nernst potentials can be calulated for other ions (Ca^{2+}, Cl^-) based on their inside and outside concentrations. Taking into accout all ions, permeabilities, and concentrations, the resulting resting potential can vary in different neurons and it is typically in the range from $-70\,\text{mV}$ to $-60\,\text{mV}$ (Gerstner and Kistler 2002).

The Hodgkin–Huxley biophysical model quantitatively describes ion currents through a small patch of a squid giant axon. The membrane patch can be modeled by an equivalent circuit shown in Figure 1.8. The capacitor describes the electrical properties of the lipid bilayer. The resistors correspond to the various ion channels and the voltage sources to the reversal potentials due to gradients in ion concentrations. Some of the channels are gated, i.e., whether they are open or closed depends on the state of one or more internal "gates." Generally, the currents in the Hodgkin–Huxley circuit in Figure 1.8 can be written as

$$I(t) = I_C(t) + I_{\text{L}}(t) + I_{\text{K}}(t) + I_{\text{Na}}(t), \tag{1.2}$$

where I is the overall membrane current, I_C is the capacitive portion of the current, I_{L} is a leak current composed mostly of Cl^- ions, I_{K} is the potassium current, and

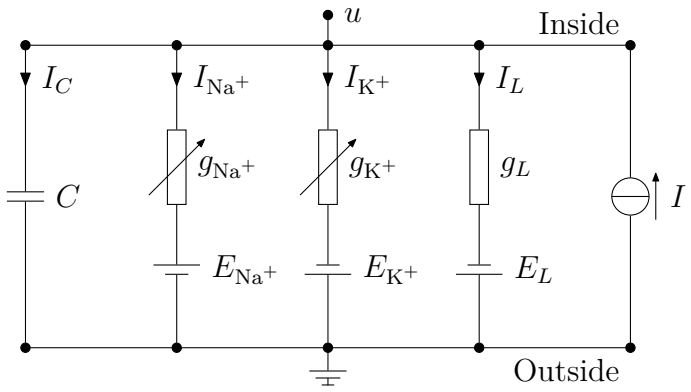

Figure 1.8: The equivalent electrical circuit of the Hodgkin–Huxley model.

I_{Na} is the sodium current. In the case of Na^+ and K^+ channels, the gates' states depend on the membrane voltage. Equation 1.2 can be further expanded to

$$I(t) = C\frac{du}{dt} + g_{\mathrm{L}}(u - E_L) + \bar{g}_{\mathrm{K}}n^4(u - E_{\mathrm{K}}) + g_{\bar{\mathrm{Na}}}m^3h(u - E_{\mathrm{Na}}), \tag{1.3}$$

where u is the voltage across the membrane, C is the capacity of the patch. E_{L}, E_{K}, and E_{Na} are reversal potentials. g_{L}, g_{Na}, and g_{K} are peak conductances for leak, Na^+, and K^+ currents respectively. Finally, n, m, and h describe the gating state of the voltage-gated channels and determine whether a channels is open or closed. They are probabilities that certain gates allow ions to get through. In Equation 1.3, the Na^+ and K^+ channels have four gates each. K^+ channels are described by four n gating variables and Na^+ channels by three m and one h gating variables.

The gating variables follow Boltzmann functions and change according to the following differential equations:

$$\frac{dn}{dt} = \alpha_n(u)(1 - n) - \beta_n(u)n, \tag{1.4}$$

$$\frac{dm}{dt} = \alpha_m(u)(1 - m) - \beta_m(u)m, \tag{1.5}$$

$$\frac{dh}{dt} = \alpha_h(u)(1 - h) - \beta_h(u)h, \tag{1.6}$$

where the α and β functions depend on the membrane voltage u and can be measured empirically. The Hodgkin–Huxley's $\alpha(u)$ and $\beta(u)$ functions, after adjusting the

resting potential to $-65\,\mathrm{mV}$, are given by

$$\alpha_n(u) = \frac{0.01(-55-u)}{\exp(\frac{-55-u}{10})-1} \tag{1.7}$$

$$\alpha_m(u) = \frac{0.1(-40-u)}{\exp(\frac{-40-u}{10})-1} \tag{1.8}$$

$$\alpha_h(u) = 0.07\exp(\frac{-65-u}{20}) \tag{1.9}$$

$$\beta_n(u) = 0.125\exp(\frac{-65-u}{80}) \tag{1.10}$$

$$\beta_m(u) = 4\exp(\frac{-65-u}{18}) \tag{1.11}$$

$$\beta_h(u) = \frac{1}{\exp(\frac{-35-u}{10})+1}. \tag{1.12}$$

Note that in the original paper of Hodgkin and Huxley (1952) the value of the resting potential was set to $0\,\mathrm{mV}$. Nowadays, it is more common to set the extracellular potential to $0\,\mathrm{mV}$. As a result, the $\alpha(u)$ and $\beta(u)$ functions need to be shifted by the value of the resting potential ($-65\,\mathrm{mV}$).

Equations 1.4, 1.5, and 1.6 are often rewritten in the following form for better understanding:

$$\frac{dn}{dt} = -\frac{1}{\tau_n(u)}\left(n - n_0(u)\right), \tag{1.13}$$

$$\frac{dm}{dt} = -\frac{1}{\tau_m(u)}\left(m - m_0(u)\right), \tag{1.14}$$

$$\frac{dh}{dt} = -\frac{1}{\tau_h(u)}\left(h - h_0(u)\right), \tag{1.15}$$

where $n_0(u)$, $m_0(u)$, and $h_0(u)$ indicate steady state values of n, m, and h at a given membrane voltage u. $\tau_n(u)$, $\tau_m(u)$, and $\tau_h(u)$ are time constants at which the gating variables approach steady state. The relationship between the gating variables and α and β functions is given by

$$n_0(u) = \alpha_n(u)/\left(\alpha_n(u)+\beta_n(u)\right) \tag{1.16}$$

$$m_0(u) = \alpha_m(u)/\left(\alpha_m(u)+\beta_m(u)\right) \tag{1.17}$$

$$h_0(u) = \alpha_h(u)/\left(\alpha_h(u)+\beta_h(u)\right) \tag{1.18}$$

$$\tau_n(u) = 1/\left(\alpha_n(u)+\beta_n(u)\right) \tag{1.19}$$

$$\tau_m(u) = 1/\left(\alpha_m(u)+\beta_m(u)\right) \tag{1.20}$$

$$\tau_h(u) = 1/\left(\alpha_h(u)+\beta_h(u)\right). \tag{1.21}$$

The steady state and the time constant functions are plotted in Figures 1.9 and 1.10 respectively.

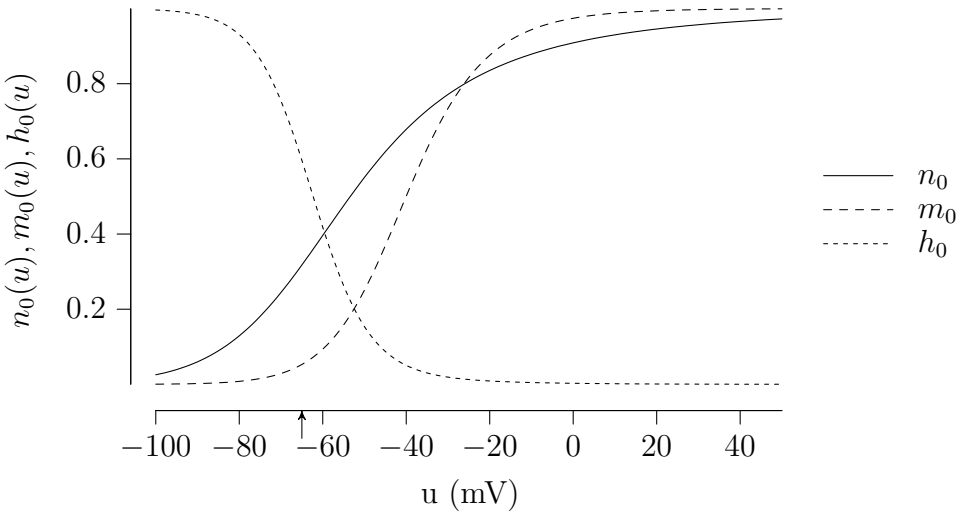

Figure 1.9: Asymptotic values for n, m, and h in the Hodgkin–Huxley model. The resting potential was adjusted to −65 mV and is marked by an arrow.

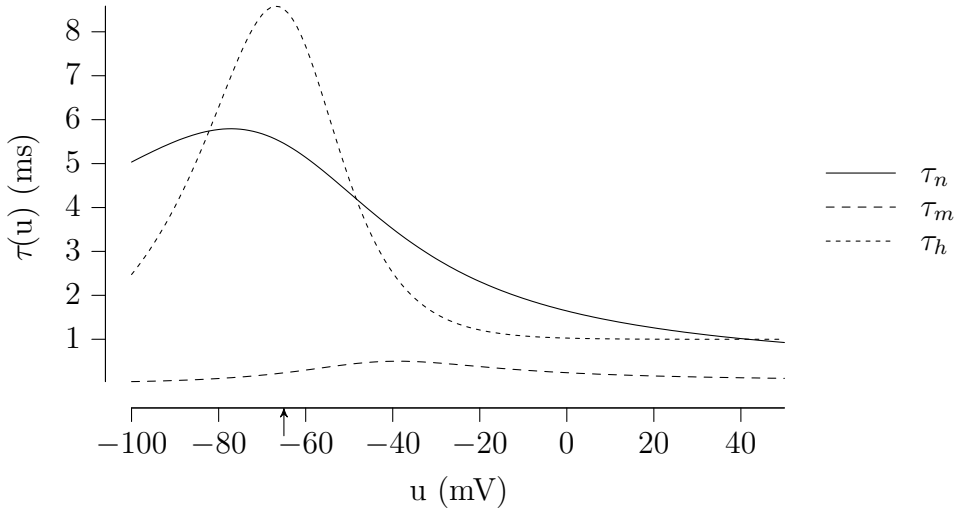

Figure 1.10: Time constants for n, m, and h in the Hodgkin–Huxley model. The resting potential was adjusted to −65 mV and is marked by an arrow.

1.4.1 Action Potentials

APs are brief but large changes in the membrane potential. Because of their shape they are often called *spikes*. As the APs travel robustly along the axon of neurons, they encode and carry information in the nervous system. The Hodgkin–Huxley equations describe quantitatively the process of eliciting and fading of an APs. A typical waveform of an AP is shown in Figure 1.11. Let us first consider the asymptotic values of gating variables in Figure 1.9. The increase in membrane voltage due to a stimulus causes m_0 to increase, causing m to increase (Figure 1.11, Equation 1.14). Increase of m increases the conductance of the Na^+ channel (Equation 1.3). The Na^+ current causes u to increase further. As a result of this positive feedback, there is a rapid increase of the membrane voltage u, which reaches its peak amplitude. Next, the positive feedback is interrupted by the inactivation of the Na^+ channels. The inactivation is modeled by a decrease in h with increasing u (Figure 1.9). At the same time, there is an increase of n and associated increase of conductance of K^+ channel conductance. The increased K^+ current is in the opposite direction to the Na^+ current and contributes to the decrease of the membrane voltage u. At the end of an AP, the K^+ current causes a brief negative overshoot. It is essential that both inactivation of the Na^+ channels (h) and the activation of the K^+ channels (n) are slower than the initial activation of the Na^+ channels (m). This timing leads to a delayed "shut down" of the Na^+ current, return of the membrane to the resting potential, and is directly responsible for the characteristic shape of an AP (Figure 1.11).

Generally, all APs are similar looking brief depolarizations of the membrane. However, different stimuli will cause different numbers of spikes and firing patterns. First, to elicit an AP, the stimulus has to reach a certain threshold. If it is too small, the membrane voltage will quickly return to its equilibrium without large depolarization. Second, once an AP occurs, a prolonged stimulus, e.g., a current step, can cause further APs. Higher stimulation amplitudes can cause an increased firing frequency of the neuron. However, the firing frequency does not increase infinitely and is limited by the refractoriness of the membrane. It is caused by the temporary inactivation of Na^+ channels (h) and the hyperpolarization from the K^+ current (n). The membrane needs a certain time to recover to fire another AP.

The above considerations refer to the giant axon of a squid and are not directly applicable to other neurons. Empirical observations showed that various neurons have different sets of ion channels with different properties. Therefore, for the Hodgkin–Huxley model to be useful, it is necessary to extend it with additional ion channels. Such generalizations show the robustness of the approach by Hodgkin and Huxley (1952) and are directly used in Chapters 2 and 3.

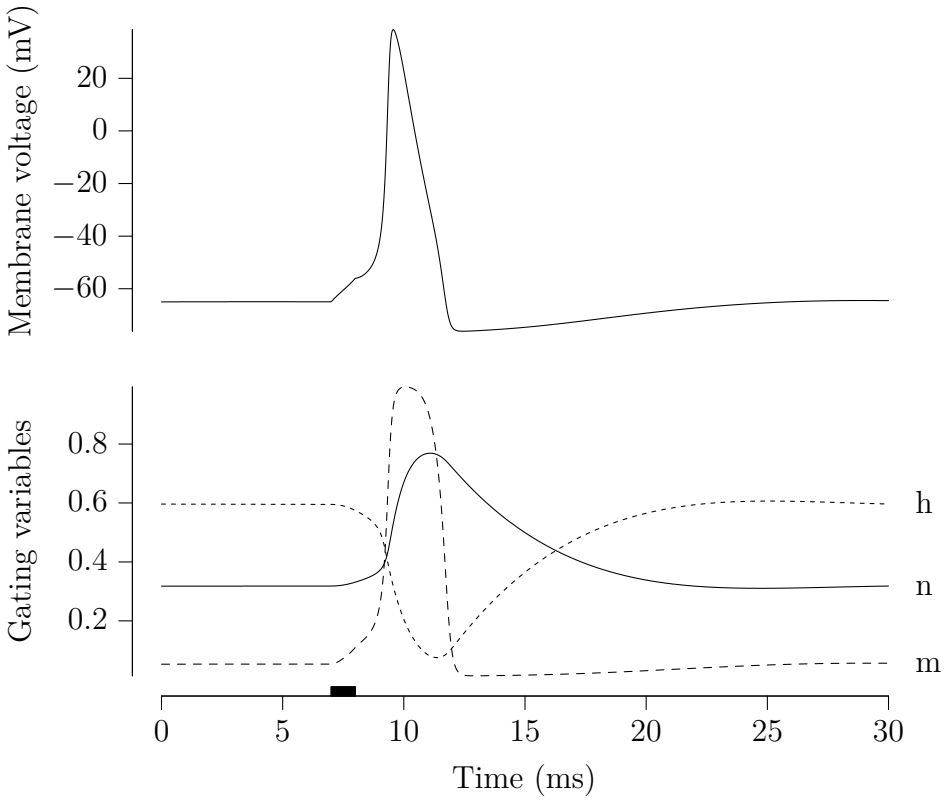

Figure 1.11: Membrane potential during an AP (top) and corresponding values of gating variables m, h, and n (bottom). The model of the membrane had the original parameters from Hodgkin and Huxley (1952) and was stimulated by a current pulse of $10\,\mu A\,cm^{-2}$, duration of 1 ms, and is marked by a black bar in the figure.

1.5 Synapses

In addition to the voltage-gated ion channels, there also exist transmitter-gated ion channels. They are essential in synapses, which enable neurons to communicate with each other. The synaptic transmission is a complex process and will be only described briefly (Bear, Connors, and Paradiso 2007).

Synapses are asymmetric with respect to information flow. Information flows from the pre-synaptic neuron to the post-synaptic one. A typical synapse consists of a pre-synaptic membrane of an axon, a synaptic cleft, and the post-synaptic membrane. A schematic of a chemical synapse is shown in Figure 1.12. Synaptic transmission is initiated by an AP at the pre-synaptic membrane. Due to membrane depolarization, voltage-gated calcium channels open and let calcium enter the pre-synaptic cell. The increased calcium concentration activates calcium-sensitive proteins in the cell and causes the fusion of synaptic vesicles with the cell membrane. The fusion of the synaptic vesicles releases neurotransmitter into the synaptic cleft, where it can freely diffuse. The neurotransmitter in synaptic cleft binds to the receptors in the post-synaptic membrane. The receptors control the opening of ion channels. Depending which ions are permitted through the channels in the post-synaptic membrane, they can either briefly depolarize or hyperpolarize the membrane. If the post-synaptic membrane depolarized, then the synapse is excitatory and the brief depolarization is called excitatory post-synaptic potential (EPSP). If the post-synaptic membrane hyperpolarizes, then the synapse is inhibitory and the brief depolarization is called inhibitory post-synaptic potential (IPSP).

Finally, the neurotransmitter from the cleft is partially recycled by the pre-synaptic membrane and partially lost (and eventually metabolized). On the whole, synapses enable APs in one neuron to change the membrane potential of another neuron. In the simplest case the EPSP can be integrated by the membrane and cause a new AP. However, the situation in the human brain is far from simple and neurons can have thousands of excitatory and inhibitory synapses, interacting in a complex manner (Drachman 2005).

All synapses in this thesis were modeled phenomenologically, i.e., the models describe the overall effect in the post-synaptic membrane without detailed mechanisms behind them. Pre-synaptic events, APs, caused a direct change in the post-synaptic conductance. It lead to a post-synaptic current and changes in post-synaptic membrane potential (EPSP or IPSP). Depending on the model, the activation of the conductance was either instantaneous with an exponential decay (endbulbs of Held) or had an exponential rise and decay (IHC synapse). In both cases, the synaptic current i_{syn} was described by

$$i_{\text{syn}}(t) = g_{\text{syn}}(t) \cdot (u - e), \tag{1.22}$$

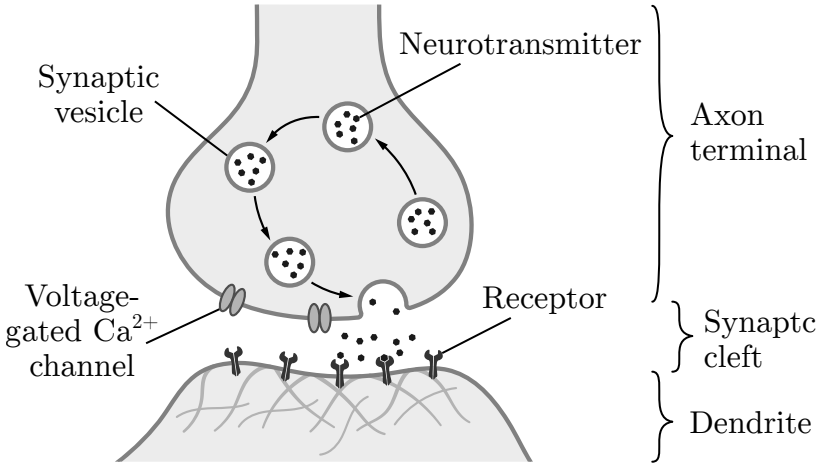

Figure 1.12: Structure of a chemical synapse. Drawing was adapted from *Synapse schematic* by Thomas Splettstoesser, Wikimedia Commons, CC BY-SA 4.0.

where g_{syn} is the synaptic conductance, e is the reversal potential, u is the membrane voltage, and t denotes time. For excitatory synapses, the reversal potential e was set to 0 mV. The peak value of $g_{\text{syn}}(t)$ is called the *synaptic weight* or the *synaptic strength* and was usually denoted with w. An example of an excitatory post-synaptic current is shown in Figure 2.4.

1.6 Q_{10} Temperature Coefficient

The rate of reactions in chemical and biological systems depends on temperature. However, most *in vitro* experiments with neurons are performed at a lower temperature. Therefore, data obtained from *in vitro* experiments cannot be used directly to describe *in vivo* phenomena. This discrepancy is particularly true for the membrane currents.

Empirical observations show that most chemical reactions "roughly double or triple" their rate for every 10 °C rise in temperature (van 't Hoff 1898). Therefore, the rate of a reaction can be calculated with the equation

$$R_2 = R_1 Q_{10}^{(T_2 - T_1)/10}, \tag{1.23}$$

where R_1 and R_2 are the reaction rates at temperatures T_1 and T_2 respectively, and Q_{10} is the temperature coefficient. As mentioned, the typical values of Q_{10} for biological systems are in the range of 2 to 3.

This temperature dependence can be applied directly to the Hodgkin–Huxley model by scaling the time constants of the gating variables (τ_n, τ_m, τ_h). As a result, a model that was fitted at a lower temperature T_1 can be scaled and simulate

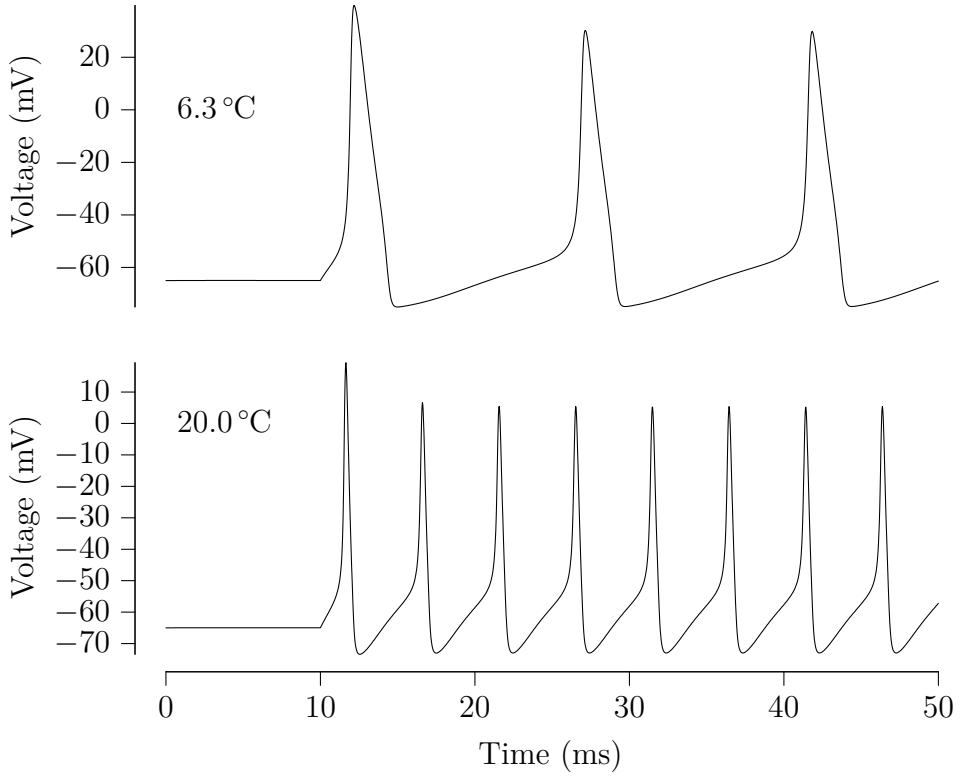

Figure 1.13: Membrane potential of a Hodgkin–Huxley neuron model simulated at two different temperatures (6.3 °C and 20 °C). The time constants of the gating variables were scaled with Equation 1.23 where Q_{10} was 3. The reversal potentials were not updated with the temperature. The stimulus was a current step of $10\,\mu A\,cm^{-2}$ that started at 10 ms.

membrane currents at a higher temperature T_2. Figure 1.13 shows a simulation of a neuron at two different temperatures. In both cases the stimulus was a current step with an amplitude of $10\,\mu A\,cm^{-2}$. The higher temperature caused the time constants to decrease, the width of individual APs to decrease, and the firing rate to increase. The reversal potentials were not updated with the temperature.

1.7 Properties of Spike Trains

Sensory stimuli are encoded in the nervous system with sequences of APs, which are called spike trains (e.g., Figure 1.13). Because all APs in a spike train look mostly alike, they are often represented only by their occurrence time, which is the most important property in sensory and neural encoding (Dayan and Abbott 2005;

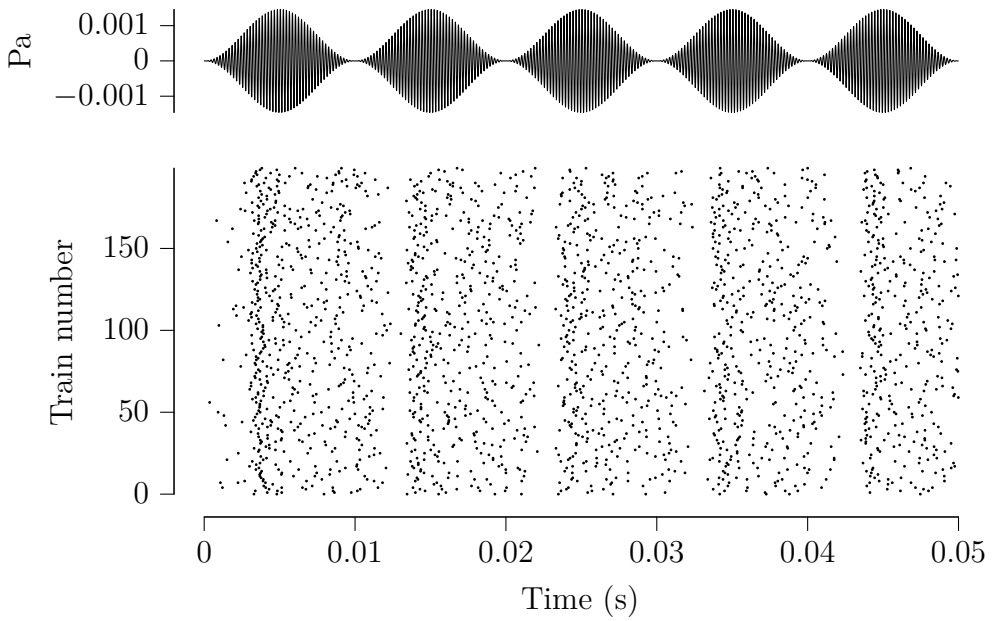

Figure 1.14: The top panel shows an amplitude modulated tone (carrier frequency of 5 kHz, modulation depth of 1, modulation frequency of 100 Hz) that was used as an input to the inner ear model (M. S. A. Zilany, Bruce, and Carney 2014). The lower panel shows a raster plot of the neural activity generated by the model. Each dot represents an AP and each row an activity of a single ANF. The carrier frequency of the simulus was matched with the CF of the neurons (5 kHz).

Rieke et al. 1999). A common way to visually represent multiple responses of a neuron or responses of multiple neurons to a stimulus is by drawing a raster plot. In a raster plot each row corresponds to a single spike train and APs are marked by dots as shown in Figure 1.14.

One of the basic properties of the spike trains is the firing rate. The firing rate R is defined as

$$R = \frac{n}{T}, \tag{1.24}$$

where n is the spike count in the interval T. Firing rate is often plotted as a function of the stimulus level as shown in Figure 1.15. It is a useful overall measure how neurons respond to a given stimulus. However, the drawback is that the temporal information of the responses is discarded. Neurons also exhibit a *spontaneous rate* which is the firing rate in the absence of any stimulus. The *driven rate* is the firing rate in response to a stimulus.

Another way to represent spike trains, which is related to both the raster plot and the firing rate, is the peri-stimulus time histogram (PSTH). PSTH is calculated

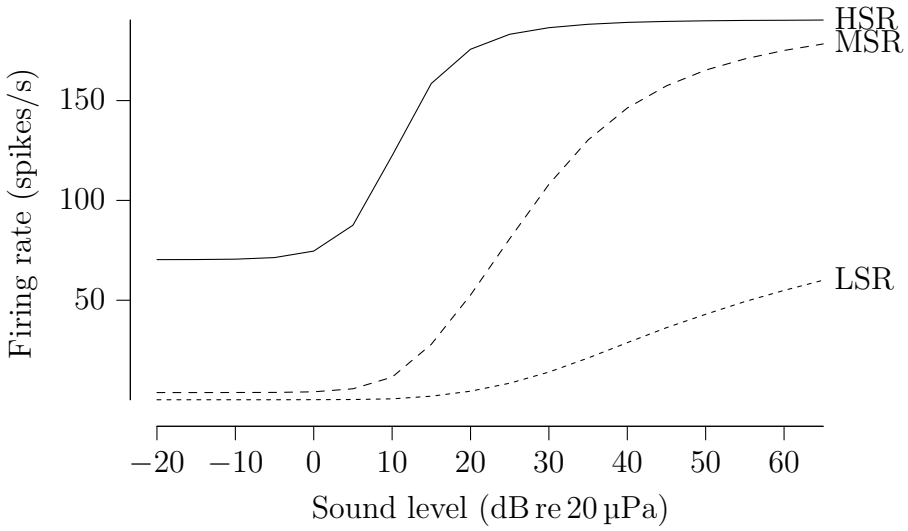

Figure 1.15: Rate-level functions of low-spontaneous rate (LSR), medium-spontaneous rate (MSR), and high-spontaneous rate (HSR) ANFs generated by a model by M. S. A. Zilany, Bruce, and Carney (2014). The stimulus was a pure tone of 5 kHz and was equal to the CF for all fibers.

by binning the time axis and counting the number of spikes from the raster plot that fall into each bin. Next, the spike count in each bin can be normalized by the number of the original spike trains and the bin size to get an average firing rate in each bin. Figure 1.16 shows an example PSTH in response to a pure tone.

The inter-spike interval histograms (ISIHs) are used to visualize the distribution of distances between adjacent spikes in the spike trains. It is constructed by calculating the time differences between all adjacent spikes in all spike trains. Next, the range of possible time differences is binned and the number of time differences in each bin is calculated. In this study all ISIHs are normalized so that they approximate the probability density function, i.e., the plot are is equal to 1. An example ISIH is shown in Figure 1.17.

The vector strength (VS) is a measure that quantifies phase locking, i.e., the tendency of neurons to fire APs at a certain phase of periodic stimuli (usually pure tones). The vector strength (VS) is calculated assuming that each spike represents a unit vector $\hat{v}$ with a phase equal to the phase of the stimulus at which it occurred. VS is equal to the magnitude of the sum of all such vectors normalized by the number of vectors n:

$$VS = \frac{|\sum \hat{v_i}|}{n}. \tag{1.25}$$

Due to normalization, the values of VS are in the range of 0 to 1. VS of 0 indicates that spikes are uniformly distributed over the stimulus period, i.e., there's no phase

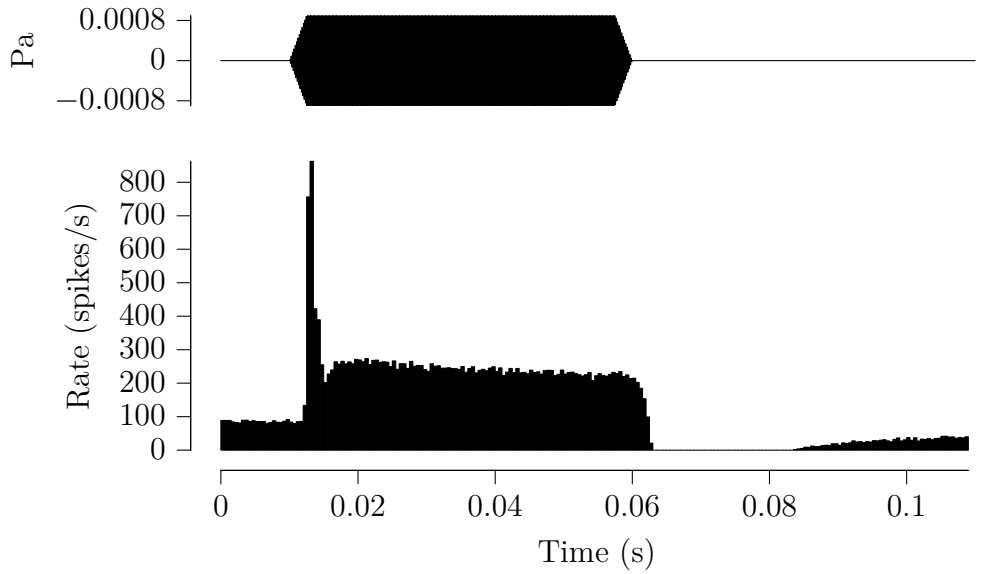

Figure 1.16: The top panel shows a ramped pure tone that was used as a stimulus. It had a duration of 50 ms and the level of 30 dB re 20 µPa. The lower panel shows a PSTH from 10 000 spike trains of an ANF (M. S. A. Zilany, Bruce, and Carney 2014) in response to that stimulus. The CF of the neuron was equal to the frequency of the stimulus, which was 5 kHz. The bin size equals 0.5 ms.

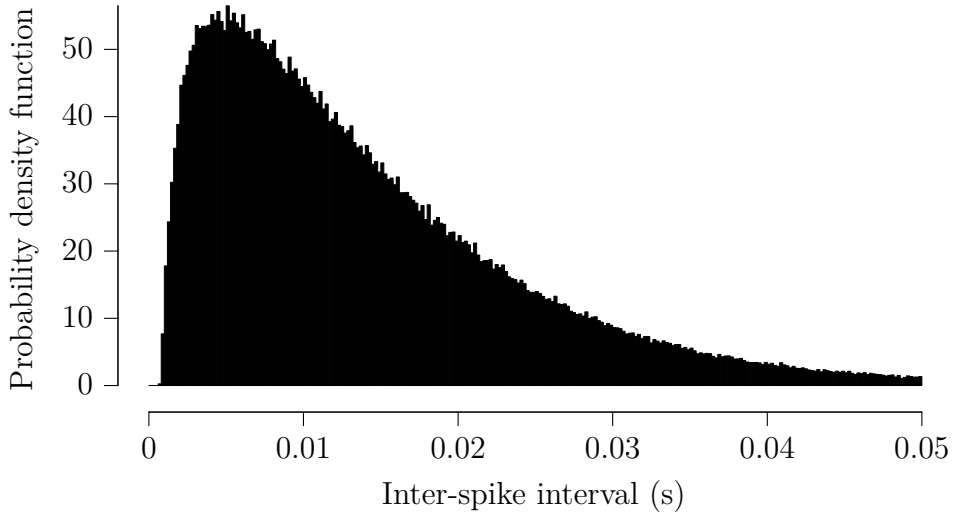

Figure 1.17: ISIH from spontaneous activity of a simulated HSR ANF (M. S. A. Zilany, Bruce, and Carney 2014). The bin size equals 0.2 ms.

locking. The VS of 1 means that all spikes occur at exactly the same phase of the stimulus, which indicates prefect phase locking.

The entrainment index (EI) specifies whether a neuron fired APs once for every period of the stimulus or less. The entrainment index (EI) can be calculated using the method described by Joris, Carney, et al. (1994). First, an ISIH is constructed. Then the number of inter-spike intervals k that fall between 0.5 and 1.5 of the stimulus period is divided by the total number of inter-spike intervals n:

$$EI = \frac{k}{n}. \tag{1.26}$$

The values of EI are also in the range of 0 to 1. A value of 1 indicates that the neuron fired at least one spike during each stimulus period. Entrainment falls to 0 when the neuron can no longer fire APs for adjacent stimulus periods.

The modulation transfer function (MTF) characterizes neural response to amplitude modulated tones of different modulation frequencies. The values of the modulation transfer function (MTF) are found by playing a modulated tone with the carrier frequency equal to the CF of a neuron. The level of the stimulus should be 10 dB above threshold. Then, for each modulation frequency, a modulation gain is calculated as

$$G_{\text{mod}} = 20 \log_{10} \frac{\text{modulation depth of response}}{\text{modulation depth of stimulus}} = 20 \log_{10} \frac{2 \cdot VS}{m}. \tag{1.27}$$

The modulation depth m was always equal to 1 in this thesis.

Chapter 2

Modeling of Synaptic and Electrical Stimulation of Auditory Nerve Fibers

2.1 Introduction

The AN is an essential part of the mammalian auditory system. It conveys sensory information from the ear (inner ear, cochlea) to the central nervous system (brainstem). The AN is made of axons of the SG neurons, also known as the auditory nerve fibers (ANFs). The ANFs are bipolar, i.e., they have two neural processes: an axon and one dendrite protruding from the soma. Each dendrite receives inputs from the IHCs in the cochlea and forwards it through axons to the neurons in the auditory brainstem (Webster, Popper, and Fay 1992). Figure 2.1 shows a block diagram of the initial stages of the auditory pathway.

If the delicate IHCs are damaged, then the ANFs are not stimulated and the sensory flow to the brain stops. In cases when the AN is functional, hearing sensations can be partially restored by bypassing the damaged sensory cells with a CI. A CI consists of a microphone, a signal processor, a battery, and electrodes surgically inserted into the cochlea. The function of a CI is to convert sounds, transform them into electrical pulses, and stimulate the AN with electricity. A modified block diagram of the auditory pathway stimulated by a CI is shown in

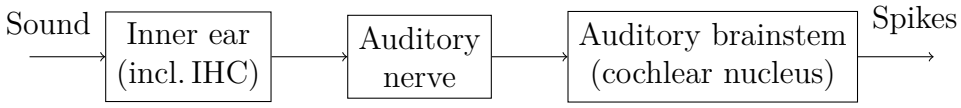

Figure 2.1: Block diagram of the initial stages of a healthy auditory pathway.

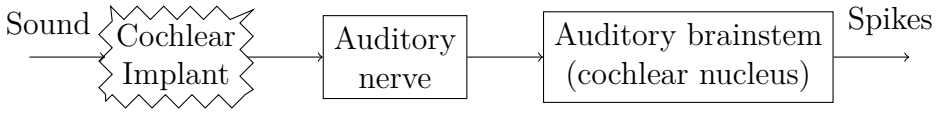

Figure 2.2: Block diagram of the initial part of a auditory pathway stimulated by a cochlear implant.

Figure 2.2.

In the majority of modeling studies, the authors focus either on synaptic (Holmberg 2007; M. S. A. Zilany, Bruce, and Carney 2014; Sumner et al. 2002; Hossain et al. 2005; Rudnicki, Schoppe, et al. 2015) or on electrical stimulation (Negm and Bruce 2008; Negm and Bruce 2014; Woo, Miller, and Abbas 2009; Rattay, Lutter, and Felix 2001; J. Frijns, Snoo, and Kate 1996). Generally, such a division is well justified, because SG neurons receive either synaptic inputs in healthy subjects or electrical stimulation in patients with CIs. However, in particular cases, patients with residual hearing can receive an electro-acoustic implant systems (Ilberg et al. 2011). They can be implanted in a way that the CI electrodes do not damage the remaining sensory cells in the apical portion of the cochlea. As a result, some of the ANFs are stimulated synaptically by the IHCs and the remaining portion is stimulated by the implanted electrodes. In practice, as the electric current spreads wide in the cochlea, bimodal stimulation might also occur for some ANFs.

Is it possible to build a SG neuron model that is capable of synaptic, electric, and mixed stimulation? How complex does it have to be? Can we constrain parameters using data from both modalities? Those questions motivated the study and development of such an ANF model here. This thesis shows how a relatively simple multi-compartment model can simulate *in vivo* experiments including recordings of single units in acoustical and electrical stimulations, as well as some psychophysical experiments with human CI patients. This thesis focuses on simulations of single ANFs and can be extended to population models and more complex cochlear anatomies in the future.

The first block in Figure 2.1 represents an inner ear, which includes a BM, IHCs, and IHC synapses. It is connected with the input of the second block representing ANFs. Typically, in the modeling studies of the inner ear, most of the development effort is spent on the first block, i.e., the BM and the organ of Corti. The ANFs are usually modeled with simplistic phenomenological spike generators, which focus solely on their dynamics (Holmberg 2007; M. S. A. Zilany, Bruce, and Carney 2014; Sumner et al. 2002). This study extends this approach and combines a biophysical model of the inner ear (Holmberg 2007) with a biophysical multi-compartment Hodgkin–Huxley-type ANF model. Both the inner ear and the ANFs are coupled

with synapses, which were carefully adjusted to *in vitro* measurements form Li et al. (2009). The performance of the hybrid model was evaluated against experimental *in vivo* data.

In addition to the synaptic stimulation, the same ANF model was used for electrical stimulation (Figure 2.2). In this case, the whole inner ear block from Figure 2.1 was replaced by the CI block. The model of a CI included only electrodes placed in the vicinity of the AN. The positioning of the electrodes plays an important role in the electrical stimulation. For example, the further away the electrodes are from the neuron, the weaker is the stimulation of the neuron. The morphology of the neuron influences the stimulation (Rattay, Lutter, and Felix 2001; Rattay, Leao, and Felix 2001) too. For example, a response of a straight neuron differs from a response of a bent neuron, even though the geometric distance to the electrode is the same. The interplay between the distance between the electrode and the neuron and the pulse polarity can result in unintuitive firing patterns (Ranck 1975). For example, a cathodic pulse from an electrode next to an axon will depolarize the membrane in the region closest to the electrode (main stimulation lobe) and hyperpolarize it in the neighboring regions on both sides (side lobes). If the stimulus is strong enough it will initialize an AP in the main lobe. However, if the stimulus strength is further increased, the hyperpolarizing side lobes might block the conduction of the ANs. As a result, increasing the stimulus might actually decrease the neural activity. A good model has to take those factors into account to make valid predictions.

This study shows how to find positions of electrodes in a model by fitting responses of electrical stimulations in the model to *in vivo* experimental results from a cat. Similarly, the position of the electrode in the model of a human cochlea was determined by fitting the model responses to psychoacoustic results.

In summary, the main conclusions of the study are:

- A single ANF model can be used for both synaptic (Section 2.3.1) and electrical (Sections 2.3.2, 2.3.3, and 2.3.4) stimulation. The same model was used to simulate both *in vivo* and psychophysical experiments.

- The position of the electrode strongly influences excitation of the neurons. This fact can be used to locate electrodes in the model (Sections 2.3.2 and 2.3.4).

- The model provides a possible explanation of the results of psychophysical experiments with CI patients (Karg et al. 2013). In the experiments, the patients were able to hear the difference in the loudness between anodic-cathodic-anodic (triphasic pulse) (ACA) and cathodic-anodic-cathodic (triphasic pulse) (CAC) pulses at the middle electrode but not at the apical one (Section 2.3.4).

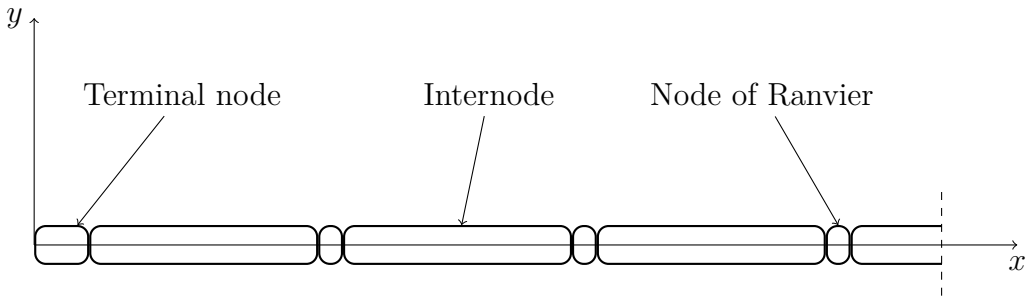

Figure 2.3: The initial segments of a multi-compartment model of an ANF. The model consisted of 40 compartments: 20 nodes of Ranvier and 20 internodes. The first node of Ranvier made the terminal node. The axis indicate the coordinate system used in this work. Dimensions in the figure are not in proportion.

2.2 Methods

The ANF model in this study consisted of alternating nodes of Ranvier and myelinated internodes. All sections were connected as illustrated in Figure 2.3. For simplification, the model did not include a cell body and consisted of a single axon only.

The model was stimulated in two ways: acoustically and electrically. For the acoustical experiments, an IHC synapse was attached at the terminal node and was used directly to activate the neuron. This arrangement corresponds to normal hearing. For "electrical hearing" an electrode was placed in the vicinity of the neuron. Its currents spread in the conducting medium surrounding both the electrode and the neuron. This setup corresponds to the cochlea stimulated by a CI. The parameters of the ANF model were the same for both stimulations and did not change throughout the simulations.

2.2.1 Model of the Auditory Nerve Fiber

This chapter is based on simulations of a multi-compartment model of an ANF. The ANF consisted of 20 nodes of Ranvier interchanged with 20 myelinated internodes. The inner diameter of all sections of the neuron was 1.5 µm. The nodes of Ranvier had a length of 1 µm. The length of the internodes was 250 µm. The synaptic ending of the peripheral axon, also called the terminal node, was longer compared to the nodes of Ranvier and had the length of 10 µm (Rattay, Lutter, and Felix 2001). Nodes of Ranvier and the terminal node contained sodium and potassium voltage gated ion channels described by Hodgkin–Huxley equations and were corrected for a temperature of 37 °C (Schwarz and Eikhof 1987; Mino et al. 2004). The current

I through a single compartment can be expressed as

$$I = C_m \frac{dV}{dt} + I_{\mathrm{Na}} + I_{\mathrm{K}} + I_{\mathrm{leak}}, \tag{2.1}$$

where C_m is the membrane capacitance, V is the membrane voltage, and $I_{\{\mathrm{Na,K,leak}\}}$ are the ionic currents of each channel type. The membrane capacitance of the nodes was set to $0.9\,\mu\mathrm{F\,cm^{-2}}$ and of the myelinated internodes to $1\,\mathrm{nF\,cm^{-2}}$. The resting membrane potential was $-78\,\mathrm{mV}$. The exact parameter values for the Hodgkin–Huxley equations can be found in Appendix A. The internodes included passive leakage channels only and their membrane current I_i is described by

$$I_i = C_i \frac{dV}{dt} + I_{\mathrm{leak}}, \tag{2.2}$$

where C_i is the capacity of the internode membrane, V its membrane voltage, t denotes time, and I_{leak} is the leakage current.

As such the ANF model was simplified and did not include a soma. This study demonstrates that a sole axon is sufficient to simulate many experiments that include synaptic and electrical stimulation. However, because the elongated unmyelinated terminal node have similar electrical properties to an unmyelinated soma in a human spiral ganglion, some results could be interpreted as coming from a model with a soma.

The model was simulated in the NEURON simulation environment (version 7.4) (Carnevale and Hines 2006) and the Python programming language. The source code of the model is freely available online at (Rudnicki and Hemmert 2018–).

2.2.2 Inner Hair Cell Synapse

To enable acoustic stimulation of the ANF model, it was necessary to attach a synapse to the terminal node of the neuron. The synapse was implemented as a conductance and was activated by presynaptic events. An event was a release of a neurotransmitter associated with a fusion of synaptic vesicle in the presynaptic membrane.

The synaptic current I_{syn} is described by

$$\begin{cases} I_{\mathrm{syn}} = g \cdot (V - E) \\ g = w \cdot f \cdot \left(e^{(-t/\tau_2)} - e^{(-t/\tau_1)} \right), \end{cases} \tag{2.3}$$

where V is the membrane voltage, E is the reversal potential and g is the synaptic conductance. The rise time is described by a time constant τ_1 and the decay time by the constant τ_2. The factor f was chosen such that the normalized peak was equal to 1. The synapse is implemented in NEURON's standard library as `Exp2Syn`.

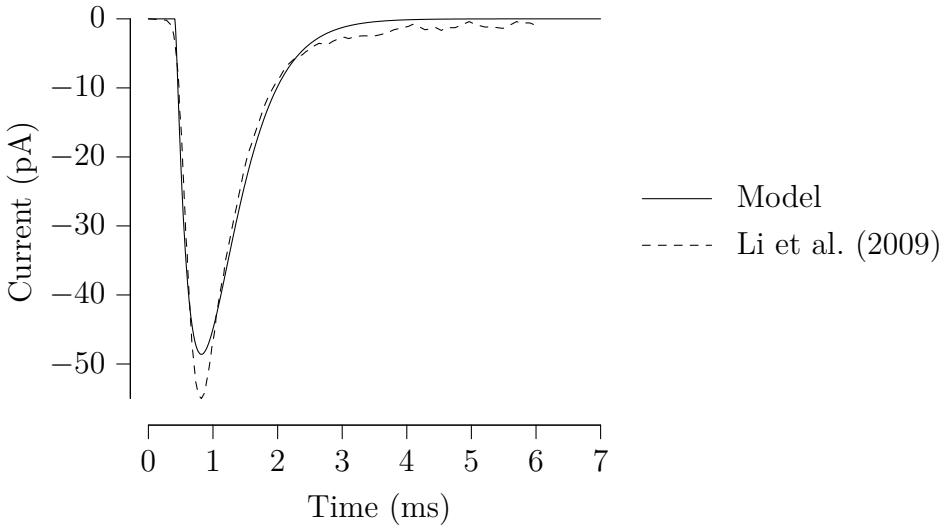

Figure 2.4: *In vitro* recording of a EPSC at a IHC synapse by Li et al. (2009) and the best model fit (Equation 2.3). The optimal parameters of the model are shown in Table 2.1.

Parameter	Value
Rise time constant τ_1	0.3928 ms
Decay time constant τ_2	0.3929 ms
Synaptic weight w	0.56 nS

Table 2.1: The optimal parameters of the `Exp2Syn` synapse model that were fitted to *in vitro* recordings of an EPSC at an IHC synapse (Li et al. 2009) at 22 °C. Both the optimal model and the experimental data are shown in Figure 2.4.

The synapse model was fitted to the measurements of the excitatory post-synaptic currents (EPSCs) at the IHC synapses (Li et al. 2009). The optimization parameters included w, τ_1, and τ_2. The goal of the optimization was to minimize the sum of squares of the measured and simulated EPSC. The optimization was performed by the Levenberg–Marquardt algorithm, which is implemented in the Scipy package (Jones, T. Oliphant, and P. Peterson 2001–). The target function of the *in vitro* recordings as well as the best fit of the synapse model are shown in Figure 2.4. The optimal parameters of the fitted synapse are given in Table 2.1.

The *in vitro* experiments of Li et al. (2009) were performed at a temperature of 22 °C. To simulate *in vivo* conditions, it was necessary to adjust the model to human body temperature. A temperature correction factor Q_{10} of 2.4 was used to adjust the time constants τ_1 and τ_2 (Postlethwaite et al. 2007). The synaptic weight

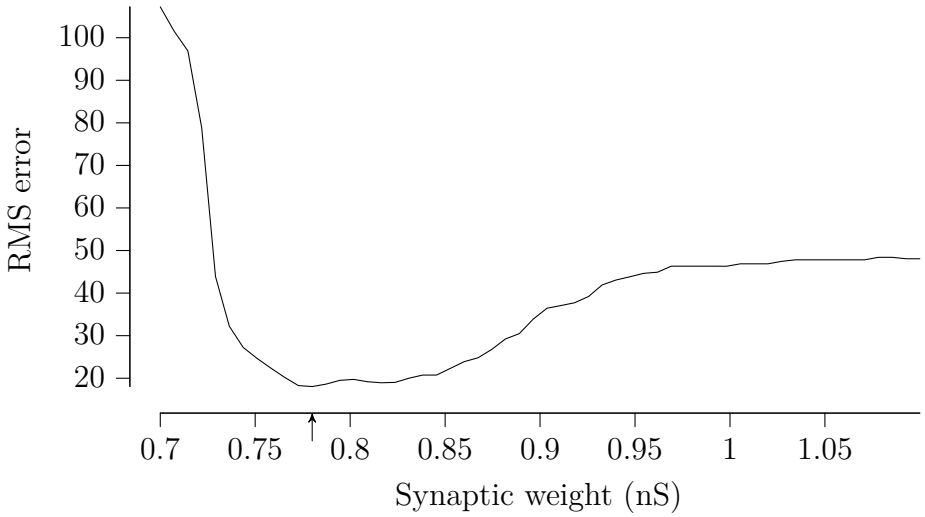

Figure 2.5: RMS errors between the rate-level functions of the hybrid model and the reference inner ear model by Holmberg (2007) for different synaptic weights. The synaptic weight determines the coupling strength between the inner ear and the ANF in the hybrid model. The optimal value of the synaptic weight was approximately 0.78 nS at 37 °C (marked with an arrow). The resulting rate-level functions are shown in Figure 2.6.

was adjusted differently, because it was necessary to make sure that the coupling between the inner ear and the ANF was appropriate. The optimal synaptic weight at body temperature was found by fitting the rate-level function of the hybrid model at 37 °C to the rate-level function of the original model from Holmberg (2007).

The root mean square (RMS) error between the simulated and reference rate-level functions for different synaptic weights is shown in Figure 2.5. It was used as the fitness function to find the optimal synaptic weight. The reference rate-level function was from the HSR fibers of the original inner ear model (Holmberg 2007). The rate-level functions were generated by stimulating the models with pure tones of 100 ms at different levels for a CF of 1 kHz. The scan of the parameter space showed that the optimal synaptic weight was approximately 0.78 nS at 37 °C. The optimal rate-level function of the hybrid model and the reference model (Holmberg 2007) are shown in Figure 2.6. Based the on optimal synaptic weights at 22 °C and at 37 °C, the Q10 factor for the synaptic weight was calculated and equaled to 1.25.

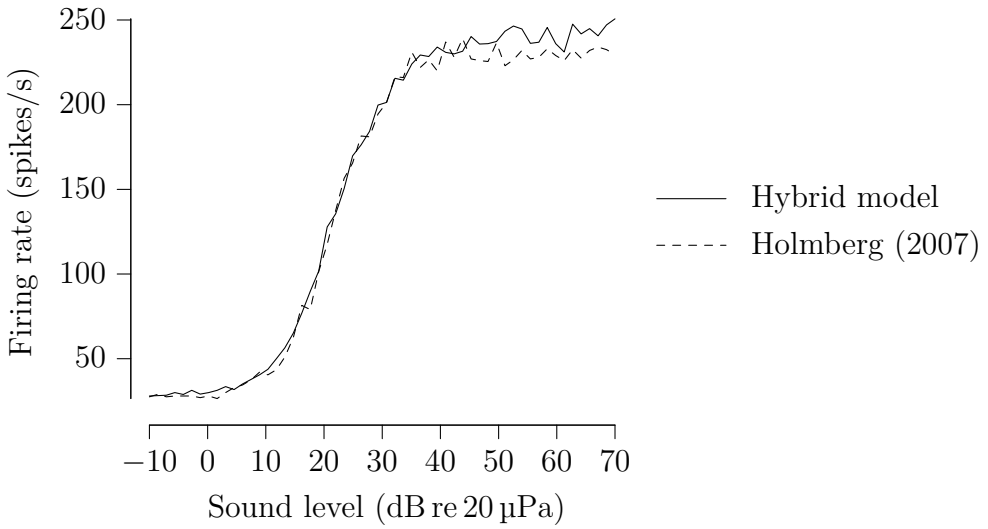

Figure 2.6: Rate-level functions of the HSR fibers of the tuned hybrid inner and the reference inner ear model (Holmberg 2007).

2.2.3 Models of the Electrodes and the Extracellular Fluid

The SG neurons are surrounded by the extracellular fluid with relatively high conductivity. It enables electrodes in the cochlea to effectively stimulate the SG neurons and elicit APs. To simulate this process, it is necessary to calculate the electric potential along the neuron in a heterogeneous cochlea (Durand 2000). On the one hand, the currents can spread relatively easily in the fluid of scala tympani ($1.43\,\mathrm{S\,m^{-1}}$). On the other hand, to reach the AN, the currents have to cross the bony surrounding of the cochlea which has much lower conductivity ($0.156\,\mathrm{S\,m^{-1}}$) (Briaire and J. H. Frijns 2000). Taking those two phenomena into account, a model of the electric field in the cochlea was constructed. The model took advantage of the coaxial configuration of the scala tympani around SG neurons, which enabled to "unroll" the cochlea as shown in Figures 2.7 and 2.8.

Calculation of the electric potentials along the neuron was performed in two steps. In the first step, the decay of the stimulating current along the scala tympani (z-axis) was computed. Kral (1998) showed experimentally that the currents have an exponential decay along the cochlea (z-axis). So the current I' in the cochlea at the z-coordinate of the neuron z' was calculated by

$$I' = I \cdot 10^{\frac{G \cdot \Delta z}{20}}, \tag{2.4}$$

where I is the electrode current, G is the gain ($-1\,\mathrm{dB\,mm^{-1}}$), and Δz is the distance between a projection of the electrode and the neuron onto the z-axis ($|z - z'|$) in mm.

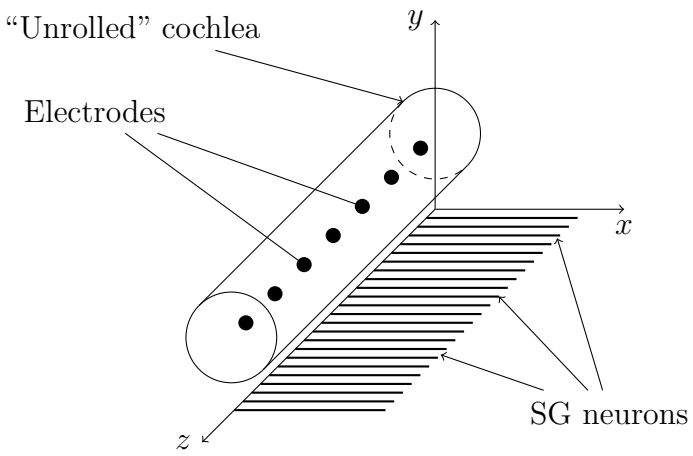

Figure 2.7: A segment of an "unrolled" cochlea with inserted electrodes and the coordinate system as used in the model of electrical stimulation. The thin solid lines mark the outline of the cochlea. ANFs are shown as thick parallel lines and black dots indicate an array of electrodes. Figure 2.8 shows the same drawing projected onto xy- and yz-planes for clarity. Dimensions in the figure are not in proportion.

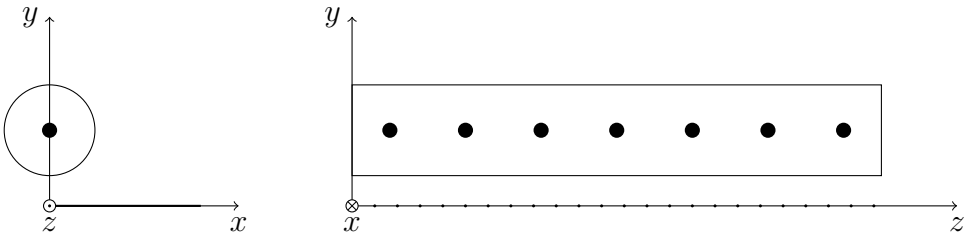

Figure 2.8: A projection of the model of an "unrolled" cochlea onto the xy- and xy-plane. The projections include: the outline of the cochlea, the stimulating electrodes, and SG neurons. Dimensions in the figure are not in proportion.

In the second step, it was assumed that the medium surrounding the electrode and the neuron is homogeneous, isotropic, and infinite conductor in the xy-plane (Figure 2.8). The electrode was treated as a monopole source (Malmivuo and Plonsey 1995). With those assumptions, the electric potential Φ was calculated with

$$\Phi = \frac{I'}{4\pi\sigma r}, \tag{2.5}$$

where σ is the conductivity of the medium ($1/\sigma = 300\,\Omega\,\mathrm{cm}$, Geddes and Baker (1967)), and r is the distance between the neuron and the projection of the electrode onto the xy-plane.

2.2.4 Electrical Stimulation of a Neuron

Once the electric potentials at each section of the model were calculated, they were used to stimulate the Hodgkin–Huxley model of the SG neuron. The field calculations were implemented in Python (T. E. Oliphant 2007) and the simulations of the electrical stimulation of the ANF were performed in the NEURON simulation environment (Carnevale and Hines 2006). In particular, the `extracellular` mechanism from NEURON's standard library was used to stimulate the Hodgkin–Huxley model. It enabled a direct application of the pre-calculated electric potentials to the neuron. The numerical simulations used the backward Euler method at a sampling frequency of 500 kHz.

A schematic of an equivalent circuit of the `extracellular` mechanism is shown in Figure 2.9. Each compartment of the neuron is connected with its neighbors by a resistivity R_a of $100\,\Omega\,\mathrm{cm}$. The internode compartments contain a capacitor and a passive resistor. The node compartments contain additional voltage gated sodium and potassium channels as described in Section 2.2.1. The pre-calculated electric field potentials Φ (Equation 2.5) were applied to the extracellular terminals at each section as v_{ext} in Figure 2.9.

2.2.5 Finding Detection Thresholds

The goal of most electrical and some acoustical simulations required finding of the ANF detection threshold for given stimuli. The detection threshold is defined here as the weakest stimulus that could be detected by a neuron. In the case of electrical stimulation, the neurons did not have any spontaneous activity. Therefore, the detection threshold was the weakest stimulus that caused a neuron to fire an AP. In acoustical experiments, the threshold detection was not as straightforward and required modification due to the spontaneous activity of SG neurons. In this case, the detection threshold was determined as the level of the weakest acoustical signal that caused the neurons to fire at the rate of $\mu + \sigma$, where μ was the mean

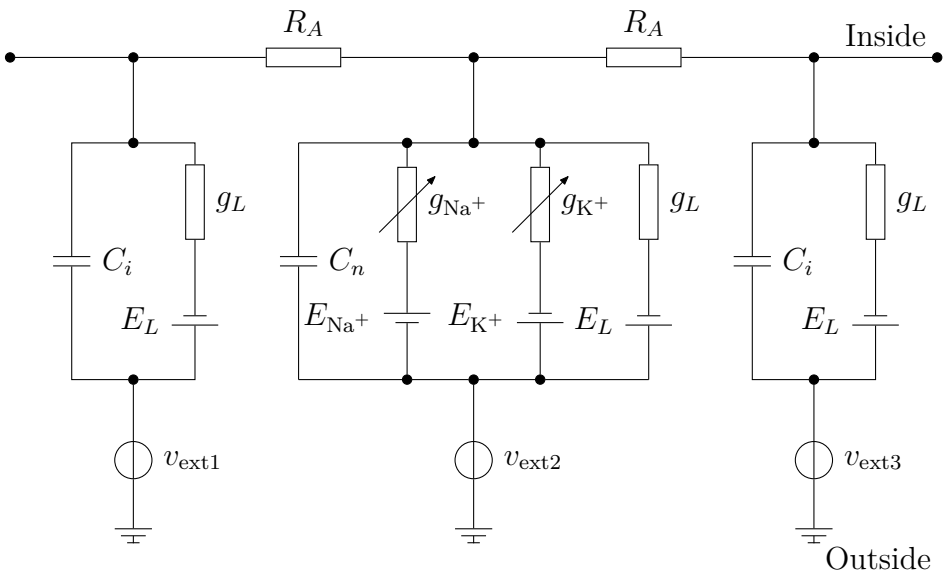

Figure 2.9: A schematic circuit representing a node of Ranvier and two internodes of the ANF model stimulated by an electric field. The electrical stimulation was implemented in the NEURON simulation environment using `extracellular` mechanism. R_a is the axial resistivity coupling the sections. the electric field was applied to each section at v_{ext}.

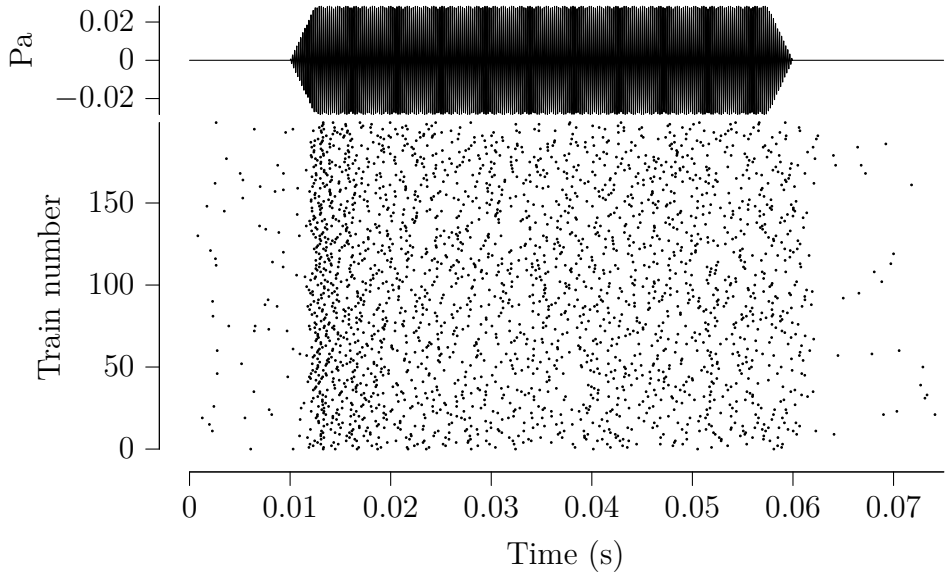

Figure 2.10: Responses of 200 HSR ANFs to a pure tone of approximately 5 kHz and the duration of 50 ms. Each dot in the raster plot corresponds to an AP fired by an ANF model.

spontaneous firing rate and σ was the standard deviation of the spontaneous rate (Geisler, Deng, and S. R. Greenberg 1985). In both cases a binary search algorithm (Burden and Faires 1985) was used to find thresholds efficiently.

2.3 Results

2.3.1 Responses to Acoustical Stimuli

The main motivation of the initial simulations was to examine responses of the model to simple acoustical stimuli. Responses of 200 HSR fibers to ramped pure tones of approximately 5 kHz, a 50 ms duration, and an intensity of 60 dB re 20 µPa are shown in Figure 2.10. Each row of the raster plot corresponds to a different ANF and each dot represents an AP. The stimulating tone started at 0.01 s and lasted until 0.06 s. The stimulus caused a visible increase in the firing rate, especially at the onset. The response of the neurons was not immediate. It is related to the delay of the traveling wave on the BM. For the same reason, the response lasted longer than the stimulus itself.

The effect of the traveling wave delay is even more visible on the PSTH plot in Figure 2.11. There is a sharp onset in the response where the neuron reached the firing rate of almost 700 spikes/s. It decayed exponentially within approximately

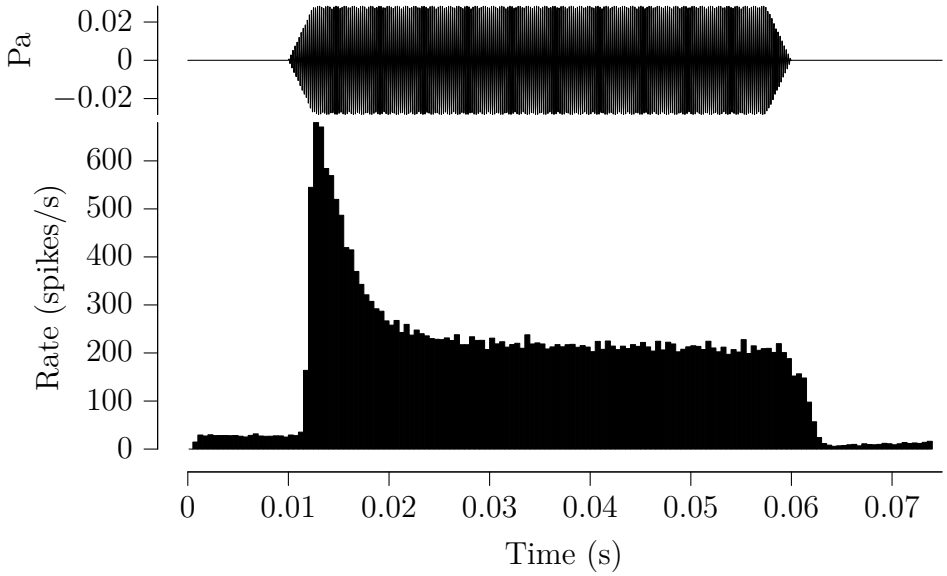

Figure 2.11: PSTH of the same spike trains as in the raster plot in Figure 2.10. This is a typical primary-like response to the ≈5 kHz pure tone including a sharp onset response followed by a mostly constant firing rate.

10 ms to a driven firing rate of ≈200 spikes/s. The spontaneous firing rate was approximately 30 spikes/s. This is a typical primary-like response of ANFs to an acoustic stimulus (Kiang 1965; Heil and A. J. Peterson 2015). One property missing in the simulated PSTH but often present in *in vivo* data is *offset adaptation*. The offset adaptation is a brief pause in the spontaneous activity after the stimulus. The hybrid model shows only a brief reduction of the spontaneous rate directly after the stimulus offset. This behavior is due to the underlying pool model of the IHC synapse (Holmberg 2007; Sumner et al. 2003). The driven and spontaneous rates are matching the rates from simulations in Figure 2.6.

Spike trains in the total duration of 1000 s of spontaneous activity were used to generate an ISIH which is plotted in Figure 2.12. The smallest inter-spike interval from the histogram was equal to 0.78 ms. This value approximates the absolute refractory period of the hybrid neuron model and was close to the refractory period "hard coded" in the spike generator of the model from Holmberg (2007). In the hybrid model, it emerged from the intrinsic properties of the cell membrane.

The temporal precision of the model was analyzed by calculating the VS in response to pure tones at various CFs. The frequency of the stimulus always corresponded to the CF of a neuron. There were 100 CFs ranging from 50 Hz to 14 000 Hz. For each CF 100 HSR ANFs were simulated. The stimulus duration was 100 ms. The ANFs were stimulated at three different levels (20 dB re 20 µPa,

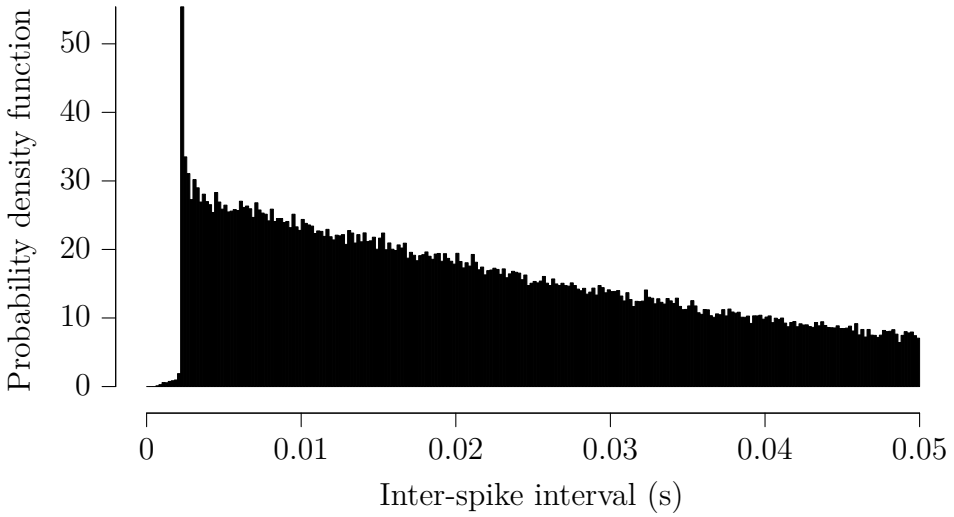

Figure 2.12: ISIH of spontaneous activity of a HSR fiber. The simulation time was 1000 s. The minimum interval approximates the absolute refractory period and is equal to 0.78 ms.

40 dB re 20 µPa, and 60 dB re 20 µPa) and only the largest VS from the three resulting values was taken into account. The VS of the responses is plotted in Figure 2.13. The plot also includes experimental data from a cat (Johnson 1980), from a guinea pig (Palmer and Russell 1986), and simulated data from Holmberg (2007) for reference. The results show that both models failed to reach the highest synchronization levels above 500 Hz. They replicated only the lowest VS values of the guinea pig data. The hybrid model had lower synchronization than the reference model by Holmberg (2007).

In addition to simple pure tones, the model was also stimulated with amplitude modulated tones to further examine precision of the temporal coding. The stimulus had a carrier frequency equal to the CF (≈10 kHz), modulation depth of 100 %, and duration of 600 ms. The modulation frequency varied from 10 Hz to 2000 Hz. For each modulation frequency the spikes of 100 HSR ANFs of the hybrid model were recorded. The spike trains were used to calculate the modulation gains, which are shown in Figure 2.14. Modulation transfer functions of the original (Holmberg 2007) and the experimental data from cat (Joris and Yin 1992) are plotted for reference. Both the original (Holmberg 2007) and the SG neuron model performed similarly. They both failed to reach high values of modulation gain measured by Joris and Yin (1992). The deviation between the models and data grew larger than 5 dB for frequencies higher than 300 Hz.

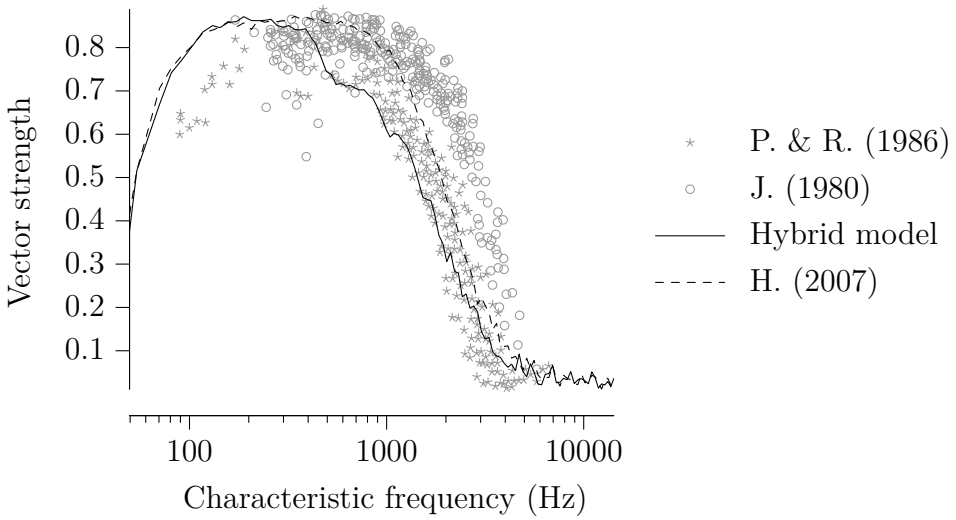

Figure 2.13: VS as a function of CF for the hybrid inner ear model and the original model from Holmberg (2007). The reference *in vivo* data comes from a cat (Johnson 1980) and a guinea pig (Palmer and Russell 1986).

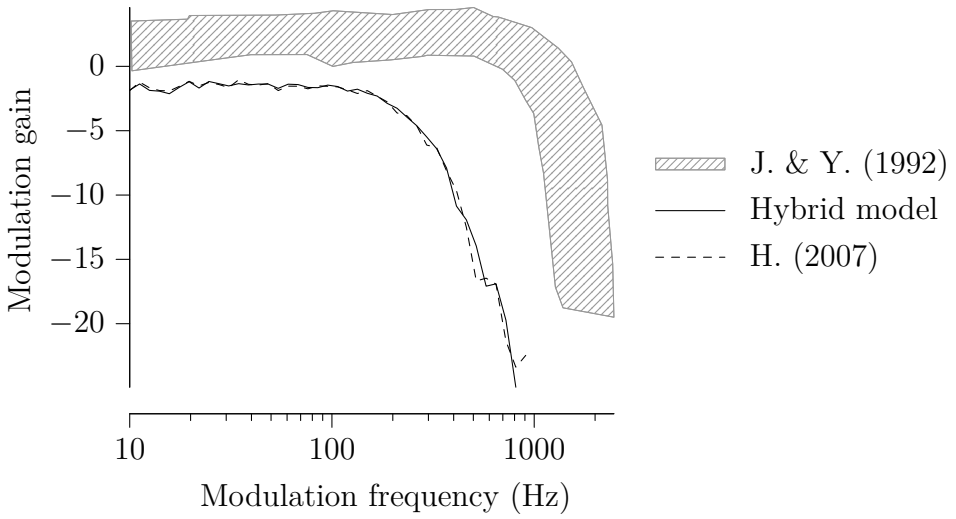

Figure 2.14: Modulation transfer function of the hybrid inner ear model, the original model from Holmberg (2007), and measurement data from a cat (Joris and Yin 1992). The experimental data is plotted as a filled area to indicate the spread of the *in vivo* recorded values.

2.3.2 Electrode Position: Cat

Relative positions of neurons and electrodes have direct influence on the electrical stimulation. Therefore, it was necessary to carefully identify the position of the electrode in the model. First, the set of possible positions was restricted mostly by the geometry of the cochlea. Second, the position was fine-tuned using data from *in vivo* experiments. In the this step, the position of the electrode was varied and the best fit to the experimental data was found. Finally, the model was validated with additional data that was not used in the tuning of the model.

To find the optimal position of the electrode, the input-output characteristics were calculated for a range of x and y values. At each position the response probabilities of a neuron for four different pulse shapes (A, C, anodic-cathodic (biphasic pulse) (AC) and cathodic-anodic (biphasic pulse) (CA)) of different amplitudes were calculated. Next, the results from each location of the electrode were compared to the experimental data from Shepherd (1999) by calculating the RMS error. Shepherd (1999) found that the thresholds of C, AC, and CA pulses were similar and the threshold of an anodic pulse was approximately 5 dB higher. The parameter scan indicated the optimal position of the electrodes at x equal to 350 µm and y equal to 820 µm. Figure 2.15 shows the input-output characteristics of the model with an electrode at these location and the reference data from Shepherd (1999). As expected, the model did not capture the dynamic range of single neurons due to a lack of a stochastic process. It showed "on-off" behavior at each threshold. This feature could be obtained by adding membrane noise to increase the dynamic range to the desired level of <3 dB (Shepherd and Javel 1997; Shepherd 1999).

Figure 2.16 shows thresholds for all four pulse shapes at locations varying from the optimal x and y values. In the top panel the y coordinate was equal to the optimal value of 820 µm and the x coordinate was variable. In the lower panel the x coordinate was fixed at the optimal value of 350 µm and the y coordinate was variable. The optimal values of the variable coordinates are marked with arrows in each panel.

2.3.3 Dynamic Range in the Electrical Stimulation

The goal of the following experiment was to validate the thresholds of the model in response to trains of electrical pulses. The ANF was stimulated by biphasic pulses at various rates as described by Shepherd and Javel (1997) in their experiments. The ANF model was placed on the x-axis starting at the origin and the electrode at the previously determined coordinates: $x = 350$ µm, $y = 820$ µm, and $z = 0$ µm. The stimuli were trains of 100 CA pulses with a duration of each phase of 100 µs. The pulses were repeated at different rates: 100 Hz, 200 Hz, 400 Hz, 600 Hz, 800 Hz,

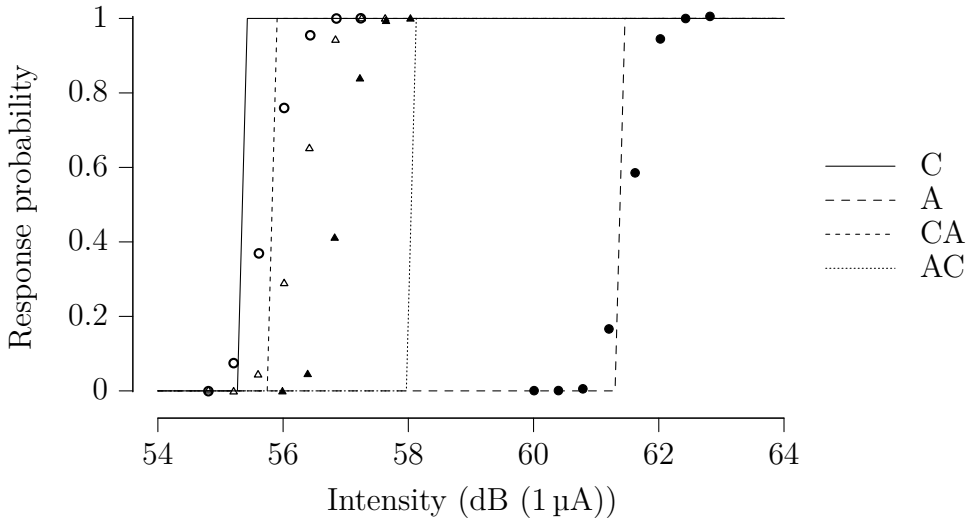

Figure 2.15: Input-output characteristic of the SG neuron model for the optimal electrode position (350 µm, 820 µm). The stimuli were monophasic (C and A) and biphasic (CA and AC) electrical pulses at different intensities. The data points were adopted from Figure 4 of (Shepherd 1999).

and 1000 Hz.

Figure 2.17 shows the rate-intensity characteristics of the model and the reference data from (Shepherd and Javel 1997). The dynamic range of the model (2 dB) was comparable with the experimental data from Shepherd and Javel (1997). Because the absolute thresholds were not finely tuned to this particular data set, and were not of the primary interests, the experimental data was shifted by 4.5 dB and overlaid onto the simulation results.

2.3.4 Electrode Position: Human

Because *in vivo* data is not available from human subjects, it was necessary to refer to psychophysical experiments. The goal was to approximate the position of the electrode in a human model of the cochlea. The simulations were based on measurements with triphasic pulses from Karg et al. (2013). The experimental data indicated a difference in perception of near-threshold levels between two different electrodes. Patients could hear, on average, a difference in loudness between ACA and CAC pulses at the apical electrode, but not at the middle electrode. Additionally, an attempt to simulate psychophysical experiments based on low-level neuronal processes gave the opportunity to investigate psychophysical measurements in more detail and find a possible explanation for some of the observed effects.

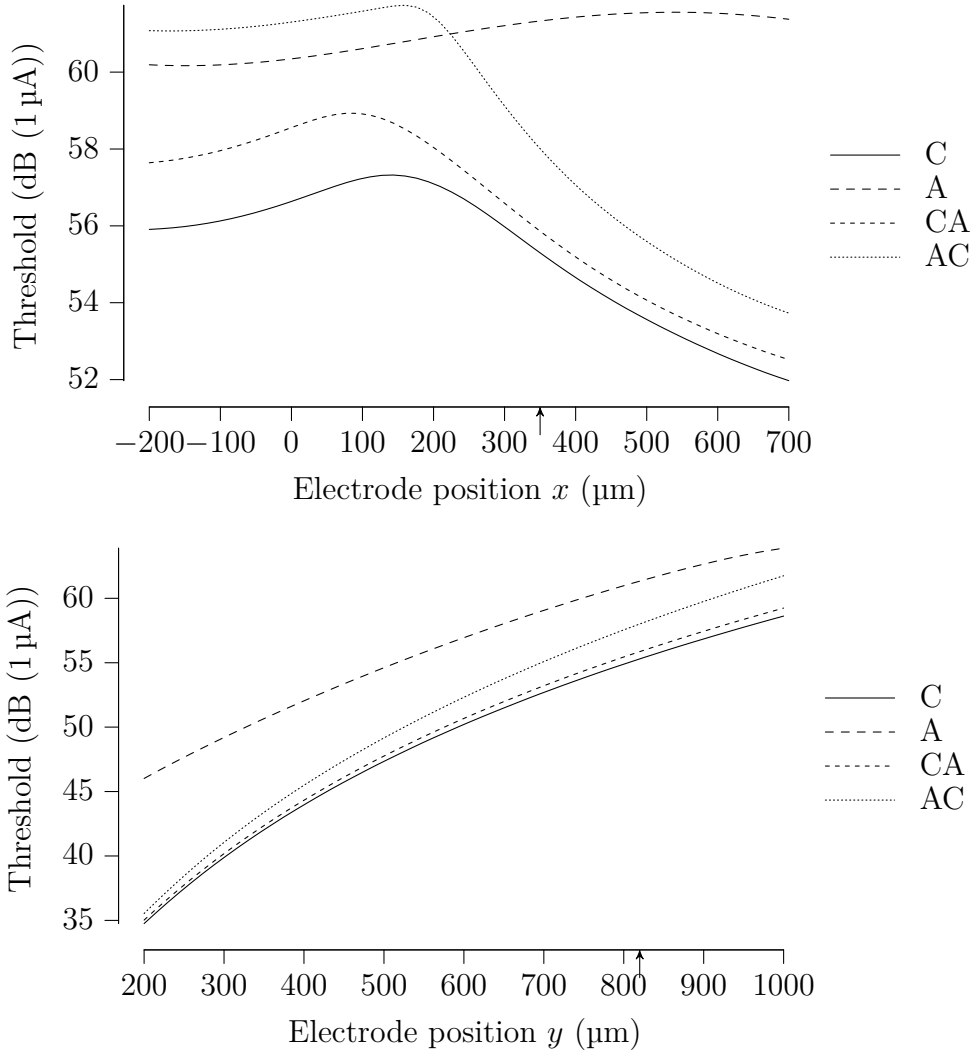

Figure 2.16: Thresholds of monophasic (C, A) and biphasic (CA, AC) pulses for electrode positions at various locations. The top panel was calculated by varying only the x coordinate of the optimal electrode position. The lower panel represents thresholds by varying the y coordinate of the optimal electrode position. The arrows in both panels mark the optimal values of x and y.

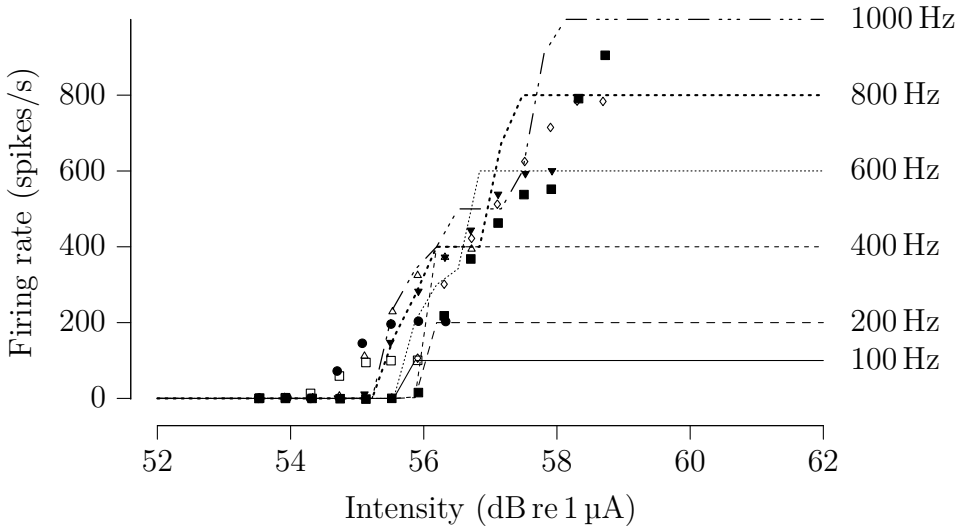

Figure 2.17: Electrical rate-instensity characteristic of the ANF model stimulated with pulse trains of 100 Hz, 200 Hz, 400 Hz, 600 Hz, 800 Hz, and 1000 Hz. The experimental data (Figure 18 from (Shepherd and Javel 1997)) was shifted by 4.5 dB to match the absolute threshold of the model and overlaid for comparison.

The psychoacoustic experiment from Karg et al. (2013) started by determining the detection threshold of biphasic stimuli for each patient. The detection threshold of CA pulses plus 25 µA was used as a reference for all further measurements. The task of the subjects was to compare the loudness of the reference pulse with the loudness of the varying triphasic pulses in an adaptive two-alternative forced choice (2AFC) procedure (Jesteadt 1980). In short, the subjects were comparing loudness of single pulses that were slightly above the detection threshold. Because the reference loudness was close to the detection threshold in experiments, it was compared directly to the detection threshold in the model.

The experimental data from Karg et al. (2013) for individual subjects (S1–S7) is shown in Figure 2.18 as points. The averaged experimental results are shown in Figure 2.19 and are also plotted with points. The averaged results show that at the apical electrode there was a significant difference in the efficiency of CAC and ACA pulses for symmetric triphasic pulses ($|Q_1/Q_2| = 0.5$). At the middle electrode there was no significant threshold difference between ACA and CAC pulses for all pulse shapes. Symmetric triphasic pulses were still less efficient than biphasic pulses ($|Q_1/Q_2| = 0$ and $|Q_1/Q_2| = 1$), both polarities showed similar efficiency.

The goal of the simulations was to calculate the optimal position of an electrode in the model based on the psychoacoustic data from Figure 2.18. For that purpose, the ANF was stimulated by an electrode at various positions around the neuron

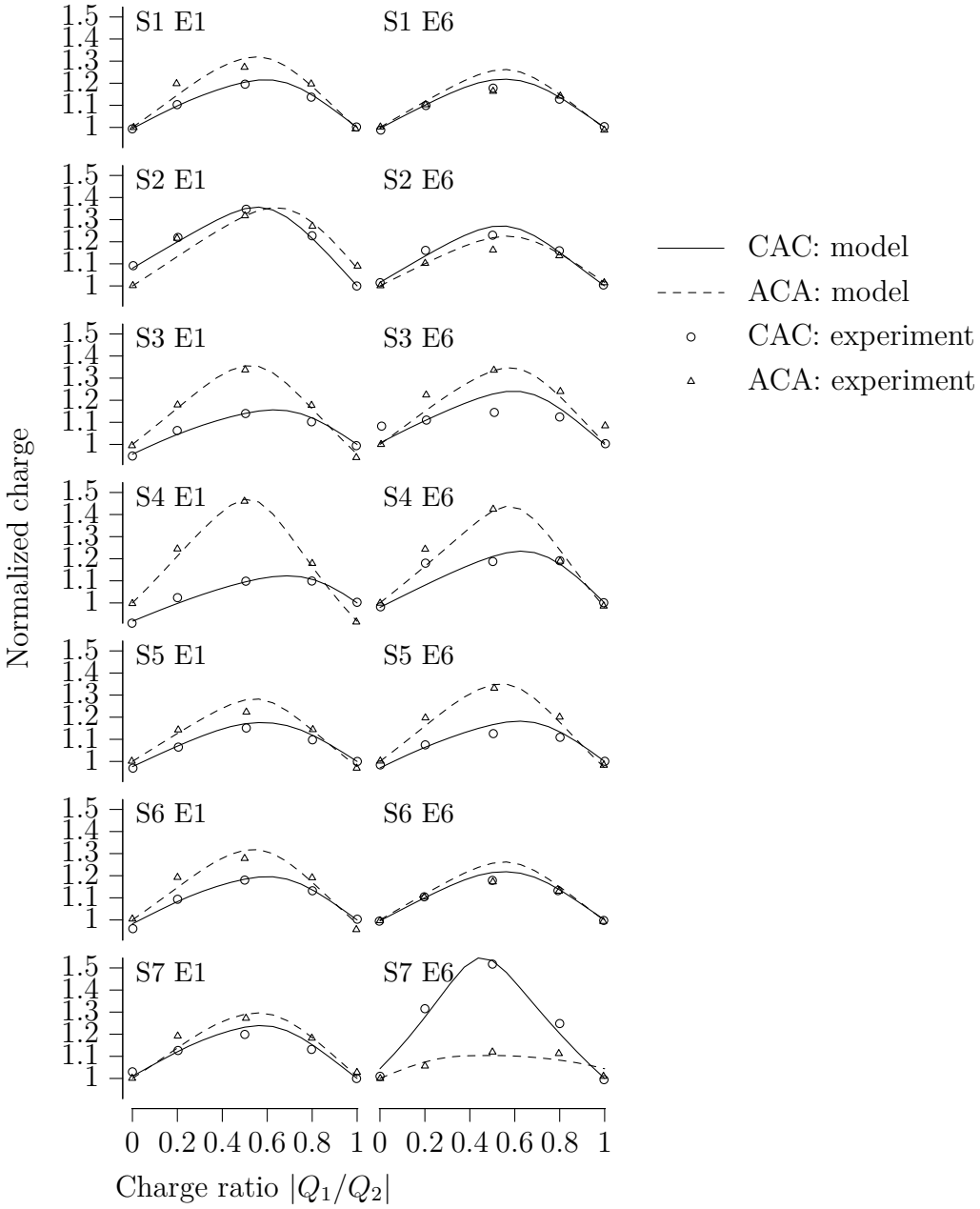

Figure 2.18: Individual hearing thresholds for subjects S1–S7 (Karg et al. 2013) and ANF model firing thresholds for triphasic pulses at the apical (E1) and the middle (E6) electrodes. Points indicate the reference experimental data. Lines correspond to fitted simulation results.

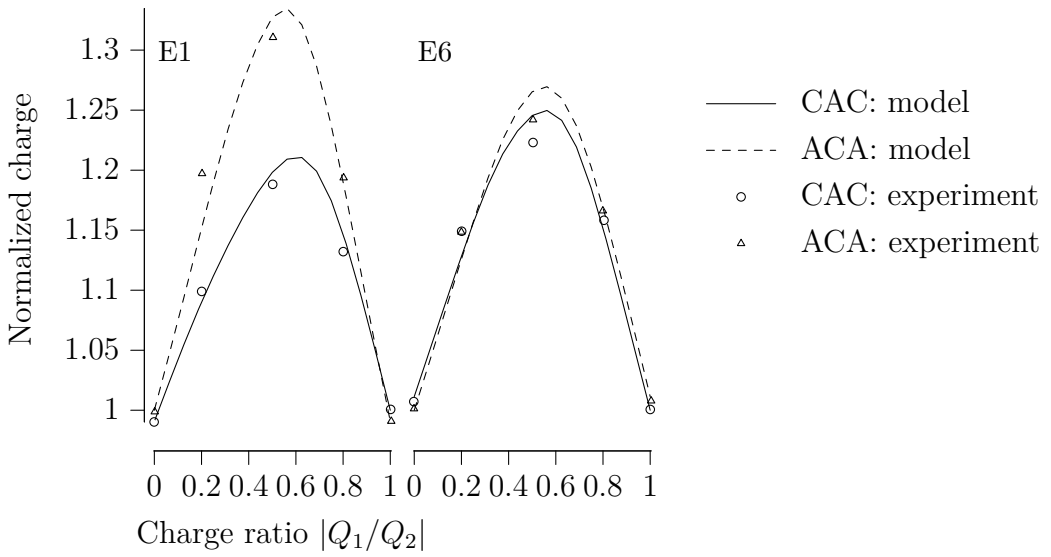

Figure 2.19: Averaged hearing (Karg et al. 2013) and firing (ANF model) thresholds for a range of triphasic pulses at the apical (E1) and the middle (E6) electrodes. Points mark the reference experimental data. Lines correspond to fitted simulation results.

using the same pulses as in the corresponding experiments. In the first step, the firing thresholds of the ANF model for all combinations of

- polarities: ACA, CAC,
- pulse shapes: $|Q_1/Q_2| \in \{0, 0.2, 0.5, 0.8, 1\}$,
- and positions of the electrode around the SG neuron

were calculated. Next, for each subject and electrode from the experiments, i.e., for each individual subplot in Figure 2.18, the RMS error between the psychoacoustic thresholds and the simulated thresholds at every location of the electrode are calculated. Finally, the electrode locations in the model that resulted in the smallest values of the error were selected and are shown in Figure 2.18. Additionally, the same procedure was repeated for the mean experimental results and is shown in Figure 2.19.

The optimal locations of the electrodes in the model are shown in Figure 2.20. The locations of the individual electrodes are marked using normal width arrows. Each arrow corresponds to a single subject (S1–S7). The origins of the arrows correspond to the apical electrodes (E1) and the arrowheads mark the locations of the middle electrodes (E6). The thick continues arrow shows the fit for the mean

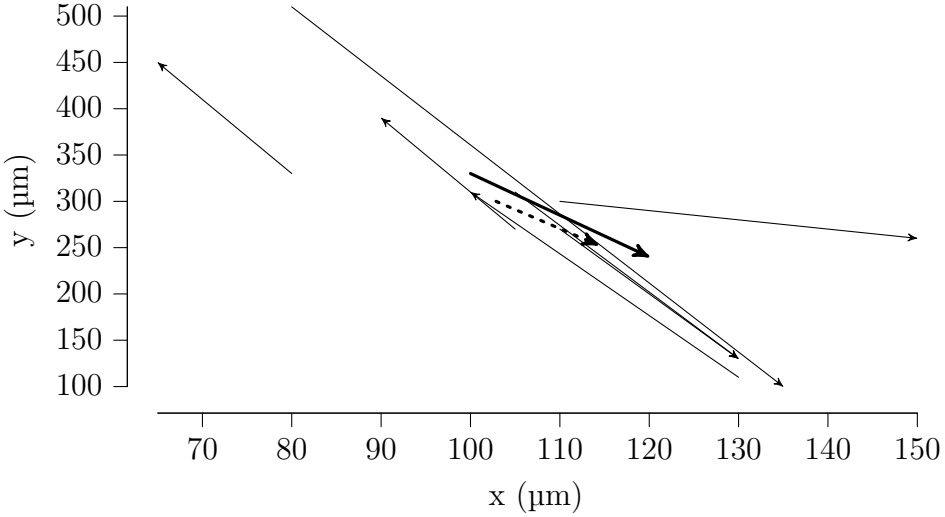

Figure 2.20: Each arrow with a normal width represent the optimal electrode positions in the model for each subject (S1–S7) from Figure 2.18. The origins of the arrows correspond to the apical electrodes (E1) and the arrowhead mark the middle electrodes (E6). The thick continues arrow shows the fit for the mean experimental results from Figure 2.19. The thick dashed arrow is an average vector of all individual arrows. The x- and y-axes are scaled differently.

experimental results. The thick dashed arrow represents an average vector of all individual arrows. Both the average vector and the vector fitted to the average data have similar directions, origins, and magnitudes. The x- and y-axes do not have the same scale. On average the E1 electrodes were located further away from the neuron than the E6 electrodes in the model.

To better understand the locations of the electrodes in the model, the normalized difference between thresholds of symmetric ACA and CAC pulses around the neuron was plotted in Figure 2.21. The values can be interpreted as the distance between the threshold curves at $|Q_1/Q_2| = 0.5$ in Figures 2.18 and 2.19 for all locations around the neuron. Figure 2.21 shows that there were two regions around the neuron:

1. Along the neuron, where the difference between ACA and CAC thresholds was negative. In this region, the ACA pulses were more efficient.

2. Close to the neuron's end and beyond, where the CAC pulses were more efficient than ACA pulses (positive difference).

On the border between both regions, the difference was close to zero and both polarities were equally efficient. On average, the apical electrode (E1) was located

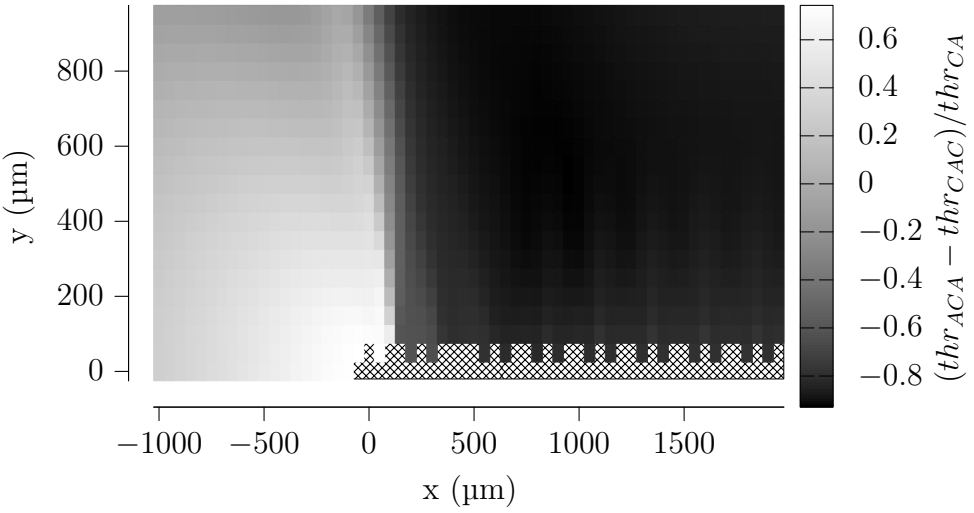

Figure 2.21: Normalized threshold difference between ACA and CAC triphasic pulses for various positions of an electrode around the neuron. The ANF was located on the x-axis and threshold values from electrode's positions closer than 65 µm were discarded (patterned pixels). The simulations show two regions around the neuron: (1) beside the neuron, where the threshold difference was negative and (2) close to the neuron's end and beyond, where the difference was positive.

deeper towards the region surrounding the terminal node. The middle electrode (E6) was located close to the border of both regions.

2.4 Discussion

2.4.1 Single Neuron Model for Synaptic and Electric Stimulation

This study shows that a single ANF model can be used both for synaptic and electrical stimulation with the same parameters. This contrasts with previous studies where models were tuned only to a single mode of stimulation. In the case of synaptic stimulation, the ANF model had to be integrated with a model of a healthy cochlea (Holmberg 2007). In the electrical stimulation, the ANF model was excited by a CI electrode. The model successfully reproduced various data from *in vivo* and psychophysical experiments. The focus of the model was

- to integrate the ANF with an existing inner ear model of Holmberg (2007),
- to properly determine the position the electrodes,

- and to explain psychophysical experiments with CI patients.

The ANF model required careful fitting of the synaptic weight (Figure 2.5 and 2.6). It assured a proper coupling between two independent parts of the model:

- the inner ear (Holmberg 2007)
- and the ANF neuron itself.

The synaptic weight was fitted at a single CF, which was sufficient for other CFs. During the fitting procedure, a wide range of levels was taken into account. Pure tone stimuli generated plausible raster plots (Figure 2.10) and PSTHs (Figure 2.11).

One of the main deficiencies of the model was the phase locking to pure tones above 500 Hz. Figure 2.13 shows that both the original inner ear model (Holmberg 2007) and the presented ANF model failed to reproduce synchronization of cat's ANFs (Johnson 1980). This is due to the fact, that both models were derived from the inner ear model of a guinea pig (Sumner et al. 2002). The current ANF model could reproduce only the lowest values of the guinea pig data (Palmer and Russell 1986). Both Holmberg (2007) and the presented ANF models aimed at human-like performance which is closer to that of a cat. The improvement of the phase locking remains an open task.

An essential part of the electrical stimulation of the neuron was the calculation of the electric field (Section 2.2.4). The calculation was based on a two-step procedure:

1. Calculate the exponential field decay along the cochlea (z-axis).
2. Calculate electric field decay that is inversely proportional to the distance in the plain perpendicular to the cochlea (xy-plane).

The main motivation behind this approach is that the cochlea is a heterogeneous structure. On the one hand, the currents spread easily along the scala tympani. On the other hand, to reach SG neurons, they have to cross a bony tissue, which has much higher resistivity. The exponential decay along the cochlea was motivated by measurements of Kral (1998). He showed a decay of $3\,\mathrm{dB\,mm^{-1}}$ in a cochlea of a cat. It is likely to be even weaker in CI patients ($1\,\mathrm{dB\,mm^{-1}}$). In the xy-plane, I assumed an infinite homogeneous medium with resistivity of $300\,\Omega\,\mathrm{cm}$ (Geddes and Baker 1967) and therefore a $1/r$ field decay. A disadvantage of the hybrid field calculation is that both functions $(e^x, 1/x)$ are not commutative and the result depends on the order in which the calculation is performed. In most cases it was not an issue, because the simulations were done for a single electrode and neurons located in the same xy-plane. Possible improvements include using a lumped element model (Kral 1998) or numerical calculation of the filed in the carefully reconstructed cochlea using the finite element method (Rattay, Leao, and Felix 2001; Bai et al. 2017; Encke, Bai, et al. 2017).

2.4.2 Literature on ANF Modeling

The presented ANF model was strongly influenced by a previous model of Bade (2009), which in turn was inspired by a single compartment model of Negm and Bruce (2008). Bade (2009) conducted a comprehensive study of a multi-compartment SG neuron model including peripheral and central axons, a soma, a synapse, and stimulating electrodes. The author stimulated the model acoustically and electrically. However, the model of Bade (2009) was focused mostly on correct initialization and propagation of single APs. Particularly, it included a soma, which influences spike propagation and in some cases can block them (Rattay, Lutter, and Felix 2001). The current model is a simplified iteration of the model from Bade (2009), i.e., it does not contain a soma and uses different membrane channels (Schwarz and Eikhof (1987) instead of Negm and Bruce (2008)).

Holmberg (2007), M. S. A. Zilany, Bruce, and Carney (2014), and Sumner et al. (2002) developed complete inner ear models where the AN is just the final stage of the model. The ANFs are implemented as simple phenomenological spike generators. The main function of the implementation is to capture the absolute and relative refractoriness of the neurons. For example, the spike generator from (Sumner et al. 2002) converts a stream of synaptic vesicle releases into a stream of APs. First, it drops all events within the absolute refractory period (0.75 ms). Second, it decreases probability of an AP directly after that period. The spike generator was implemented by integrating an exponential recovery with a time constant of 0.8 ms. M. S. A. Zilany, Bruce, and Carney (2014) showed an alternative approach to a spike generator. Their spike generator accepts an expected firing rate as an input and uses a random variable to generate times of APs. They use a double exponential recovery from the relative refractory period with time constants of 1 ms and 12.5 ms. Holmberg (2007) reused both approaches and could freely switch between them. This study shows that in many cases a simplistic spike generator is equivalent in function to a multi-compartment ANF model. In particular, the ISIH (Figure 2.12) showed that the absolute refractory period was very similar (0.78 ms) to the other studies and physiological recordings. Interestingly, the absolute refractory period in the presented model emerged just from the intrinsic properties of the membrane without further adjustments.

Hossain et al. (2005) studied the distribution of various Na^+ channels in the cochlear nerve of a mouse. Based on their measurements, they constructed a complex SG neuron model that included several compartments representing soma and different parts of the axon with Hodgkin–Huxley channels. The neurons were stimulated by phenomenological synapses implemented as the alpha function conductance. The authors focused on spike generation in a SG neuron. However, they did not examine realistic *in vivo*-like stimulation patters which sets it apart from the current study.

In a recent publication, Bruce, Erfani, and M. S. Zilany (2018) presented an updated model from M. S. A. Zilany, Bruce, and Carney (2014), which included changes in the IHC synapse. Their newest model had a more realistic presynaptic membrane with a reduced number of synaptic vesicle docking/release sites and longer redocking time as suggested by A. J. Peterson and Heil (2017). Those additions replaced the exponential adaptation and a part of the spike generator from M. S. A. Zilany, Bruce, and Carney (2014). As a result, several basic statistics, forward masking, and rate-level functions of the ANF responses were improved. The model of Bruce, Erfani, and M. S. Zilany (2018) creates an opportunity to further improve the current hybrid model by replacing the Holmberg (2007) part with Bruce, Erfani, and M. S. Zilany (2018). As a result the last stage from the model of Bruce, Erfani, and M. S. Zilany (2018)—refractoriness—could be replaced by the ANF model from the current study. This swap could improve some of the responses of the model, especially synchronization to pure tones and amplitude modulated tones.

Negm and Bruce (2008), Negm and Bruce (2014), and Woo, Miller, and Abbas (2009) focused their efforts on modeling the electrical stimulation of neurons. Those studies tackled the problem of adaptation to the electrical stimulation (Zhang et al. 2007). Adaptation is especially important when neurons are stimulated with trains of electrical pulses at high frequencies. Similarly to the acoustic stimulation, the response to a continuous stimulus becomes weaker over time and reaches a steady state. The mechanism of this adaptation is not included in the models with only Hodgkin–Huxley (Na^+ and K^+) channels, which is a limitation of the described model. Negm and Bruce (2008) and Negm and Bruce (2014) showed a single compartment model and a simplified electrical stimulation using intracellular current injection. The novelty of their model was an inclusion of membrane channels that are also present in CN neurons (I_{h} and I_{Klt}). Particularly, hyperpolarization-activated cation channels (I_{h}) caused at least some adaptation of the model across all stimulation rates. Woo, Miller, and Abbas (2009) had a different approach and showed a detailed multi-compartment model that included a mechanism where local accumulation of the external potassium ion concentration replicated responses with adaptation. Both models were able to successfully produce adaptation and are a good entry point to introduce adaptation in the current ANF model. However, more experiments are required to determine physiological reasons of the adaptation.

Rattay, Lutter, and Felix (2001) also presented a multi-compartment model of human SG neurons with electrical stimulation. Their model was built of a peripheral axon, soma, and a central axon. Nodes of Ranvier contained Hodgkin–Huxley ion channels, which were adjusted for faster gating processes in mammalian axons. Rattay, Lutter, and Felix (2001) implemented electrical stimulation using an activating function and assumed an infinite homogeneous medium. The main

goals of their study were to analyze spike generation as well as the influence of the morphology (unmyelinated soma, loss of the peripheral axon) on spike propagation. The main contributions of a soma in the model were increased delays during spike propagation and blocking of spikes for weaker stimuli.

As mentioned in Section 2.3.3, the current ANF model could fire APs at rates of 1000 Hz and higher in response to strong stimuli. Such rates are sustained only by a limited number of fibers and generally too high to represent an average ANF (Zhang et al. 2007). Better modeling of the general ANF population requires further studies to identify physiological mechanisms which limit the firing rate. One possible solution is to incorporate adaptation as shown by Negm and Bruce (2008), Negm and Bruce (2014), and Woo, Miller, and Abbas (2009). It would naturally reduce firing rates for continuous stimuli. However, Bade (2009) showed that the inclusion of I_{h} ion channels had a only limited effect on a multi-compartment model. The soma in the SG model (Woo, Miller, and Abbas 2009; Rattay, Lutter, and Felix 2001) could also reduce the maximum firing rate. However, if the stimuli become stronger, they would also stimulate the central axon and effectively bypass the soma (Bade 2009). The most promising approach to model adaptation is therefore tracking of the extracellular potassium concentration during numerical calculations as shown by Woo, Miller, and Abbas (2009).

Another comprehensive review of biophysical single- and multi-compartment ANF models is given by O'Brien and J. T. Rubinstein (2016).

2.4.3 Electrode Position: Cat

Generally, the ranges of parameters in biophysical models are bounded by experimental data and measurements. This is also true for the relative position of the electrode and the ANF. For example, it is safe assume that the distance between them should not be greater than the dimensions of the cochlea. In most cases the electrodes are located in scala tympani and their position is limited by the morphology of the cochlea. Hatsushika et al. (1990) showed that the diameter of the scala tympani in cat varies from 1 mm to 3 mm.

The exact position of the electrode in the cat cochlea was determined with the help of input-output curves for AC, CA, C, and A pulses from Shepherd (1999). First, the input-output curves were simulated at various locations of the electrode around the neuron. Second, the location that resulted in the smallest RMS error was selected. The optimal fit is shown in Figure 2.15 with the optimal position of (350 µm, 820 µm). This position is compatible with the dimensions of the cat cochlea (Hatsushika et al. 1990).

The model was completely deterministic and did not contain stochastic processes in the membrane. As a result, if the electrical stimulus was larger than a certain threshold, it always produced an AP. If the stimulus was below that threshold,

there was no spike at all. This "on-off" behavior is visible in the input-output characteristic (Figure 2.15). In the figure the dynamic range of the simulated responses is 0 dB. However, a typical *in vivo* neuron has a transition region around the threshold. In this region the firing probability varies continuously from 0 to 1. Shepherd (1999) measured a dynamic range of 1 dB to 2 dB. One possibility to improve the model is to include stochastic process in the membrane, e.g., by using Markov process for gating kinetics (Negm and Bruce 2008; Negm and Bruce 2014) or stochastic differential equation models (Goldwyn et al. 2011).

2.4.4 Electrode Location: Human

The ANF model was also used to simulate electrical stimulation of the AN in the human cochlea, which happens in CI patients. The position of the CI electrodes in the model could be determined based on the results of psychophysical experiments in humans. A suitable experiment was designed by Karg et al. (2013) where subjects were measuring stimulation thresholds at the middle and the most apical electrodes. Karg et al. (2013) reported a statistically significant difference between the thresholds (low-level loudness) of symmetric ACA and CAC pulses at the most apical electrode. At that electrode, the CAC pulses were more efficient (had lower threshold) than the ACA pulses. However, at the middle electrode, there was no significant difference between the ACA and CAC pulses.

The main challenge was to reproduce the psychophysical experimental setup as a computer simulation. On the one hand, the model consisted of a single ANF. On the other hand, the psychophysical experiments involved a living organism with a complex nervous system (cochlea, nerves, brainstem, and brain). Still, such a comparison is plausible, because the experiments focused on basic stimuli: single triphasic pulses close to the hearing threshold. For simple stimuli and a pure detection task, the low level effects at the ANFs are most likely dominant and do not require higher cognitive functions, e.g., discrimination between different stimulus types or speech understanding. In the presented experiments, patients only had to compare loudness of different pulses at low levels. This task was simulated as signal threshold detection in the model.

A parameter space scan indicated two types of areas around the model neuron as shown in Figure 2.21.

1. An area beside the neuron where the difference between ACA and CAC thresholds was negative, i.e., the ACA pulses were more efficient than CAC pulses.

2. An area closer to the neuron's end where the difference was positive, i.e., the CAC pulses were more efficient than ACA pulses.

A similar effect was described in a review paper by Ranck (1975). The author described an inversion of the efficiencies for both polarities depending on the location of the electrode:

1. near an axon,

2. or near to the soma on the opposite side in a monopolar neuron.

Those results suggest that the apical electrode should be located in the region closer to the neuron's end. The middle electrode could be located at the border between both regions where CAC and ACA pulses have similar thresholds. Figure 2.20 shows optimal electrode positions in the model for each subject from Karg et al. (2013). The simulations are consistent with the experimental data. However, it is difficult to make a definitive conclusion regarding position of the electrodes due to the small number of measurements.

Efficiency inversion of the pulse polarities was also analyzed analytically by J. Rubinstein (1993) with a passive cable model. J. Rubinstein (1993) showed that "stimulation near the end of a fiber may result in lower thresholds and may reverse the anodal/cathodal threshold ratio obtained with stimulation in the mid-portion of the fiber." They showed a similar effect, but not entirely the same, because it was located exclusively at the neuron's end. As it is later explained, the presented effect is linked to a high-capacitance section which in this case is the terminal node. However, such high-capacitance regions do not need to be located at the end of the neuron. For example, the high capacity of the cell body could cause this effect too. Another source of high-capacitance could be demyelination of the auditory nerve. This finding means that there might be more than two distinct regions where the efficiencies of different pulse polarities can change.

2.4.5 Efficiency Inversion of Electrical Stimuli

To explain the phenomenon and how the inversion of efficiency is related to the end of the neuron, two simplified models of an ANF were analyzed:

1. A model with two compartments and only capacitive membrane elements that was analyzed analytically.

2. A model with three compartments that contained both capacitance and passive resistance. It was solved numerically.

Finally, the same phenomenon was shown in detail using the actual ANF model with Hodgkin–Huxley channels.

Let's consider two patches of the neuron's membrane. In an oversimplified model each patch could be represented as a capacitance (C_1 and C_2). The existence of

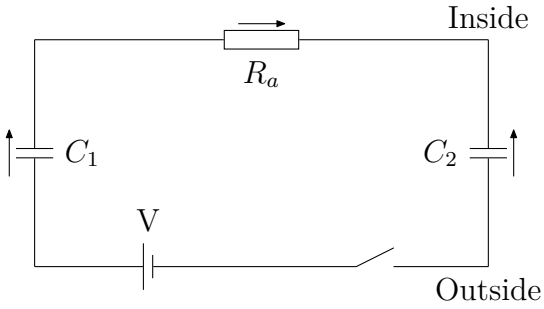

Figure 2.22: Simplified two-compartment model of an ANF stimulated extracellularly with a step function. Each compartment consist only of a capacitance. Ion channels were ignored.

membrane channels is ignored. Those two patches are connected electrically inside of the neuron through intracellular liquids (resistance R_A) as shown in Figure 2.22. Next, the model is stimulated extracellularly by applying a positive potential (step function) at the time $t = 0$. The stimulus V can be modeled as the voltage source E with a switch. How is the membrane voltage V_1 going to look like after a while?

By applying Kirchhoff's voltage law

$$V_1(t) + V_A(t) - V_2(t) + V(t) = 0 \tag{2.6}$$

and the Kirchhoff's current law (the currents through all elements are equal), we get

$$C_1 \frac{dV_1(t)}{dt} = -C_2 \frac{dV_2(t)}{dt} \tag{2.7}$$

and

$$C_1 \frac{dV_1(t)}{dt} = \frac{V_A(t)}{R}. \tag{2.8}$$

Equations 2.6, 2.7, and 2.8 can be Laplace transformed into the complex S-domain to simplify the analysis. $V(t)$ is a step function and gives E/s in the S-domain:

$$\begin{cases} v_1 + v_A - v_2 + \frac{E}{s} = 0 \\ sC_1 v_1 = -sC_2 v_2 \\ sC_1 v_1 = \frac{v_A}{R} \end{cases} \tag{2.9}$$

The system of equations 2.9 can be solved for v_1, which gives

$$v_1 = \frac{-EC_2}{s^2 R_A C_1 C_2 + s(C_1 + C_2)} = \frac{a}{s^2 b + sc}, \tag{2.10}$$

where

$$\begin{cases} a = -EC_2 \\ b = R_A C_1 C_2 \\ c = C_1 + C_2. \end{cases} \tag{2.11}$$

Applying the inverse Laplace transform to v_1 yields

$$\mathcal{L}^{-1}\{v_1\} = V_1(t) = \frac{a}{c}\left(1 - e^{-ct/b}\right). \tag{2.12}$$

As time increases the term $\left(1 - e^{-ct/b}\right)$ approaches 1 which gives

$$\lim_{t\to\infty} V_1(t) = \frac{a}{c} = -E\frac{C_2}{C_1 + C_2}. \tag{2.13}$$

The limit and therefore the steady state membrane voltage at the first segment depends on the ratio between C_1 and C_2 in the following way:

$$\begin{array}{rcl} C_1 \approx C_2 & \Rightarrow & \lim_{t\to\infty} V_1(t) \approx -0.5 \cdot E \\ C_1 \gg C_2 & \Rightarrow & \lim_{t\to\infty} V_1(t) \approx 0 \\ C_1 \ll C_2 & \Rightarrow & \lim_{t\to\infty} V_1(t) \approx -E. \end{array} \tag{2.14}$$

Typically, in electrical stimulation the highest voltages are applied to the segments that are closest to the electrode. When the capacitance is uniform along the neuron, then the section closest to the electrode has the highest absolute voltage. The sign of the voltage at the main stimulation lobe is opposite to the stimulus (E). However, if the capacitance of the neuron is not uniform and the electrode is located close to a segment with high capacitance ($C_1 \ll C_2$), then the absolute value of the membrane voltage at that segment is lower compared to the neighboring segments. The membrane potential of the neighboring segments has the same sign as the stimulus. As a result, the main stimulation lobe has a smaller amplitude compared to the side lobes.

This effect can be shown using numerical methods in a model with membrane resistance. The membrane model consisted of three compartments as shown in Figure 2.23. This time the stimulus was a monophasic anodic (positive) pulse (duration 1 ms, amplitude 1 mV). The simulation was implemented in NEURON with the parameters shown in Table 2.2.

In the first simulation, all segments had the same capacitance of $1\,\mathrm{nF\,cm^{-2}}$. The resulting membrane potentials are shown in Figure 2.24. The stimulating electrode was connected only to the first segment. The results agree with the previous analytic solution, i.e., $C_1 < C_2$ for which the asymptotic value of V_1 should be between $-E$ and $-0.5E$. The capacitance C_2 from the analytic solution can be considered as an equivalent capacitance of parallelly connected C_2' and C_3' from

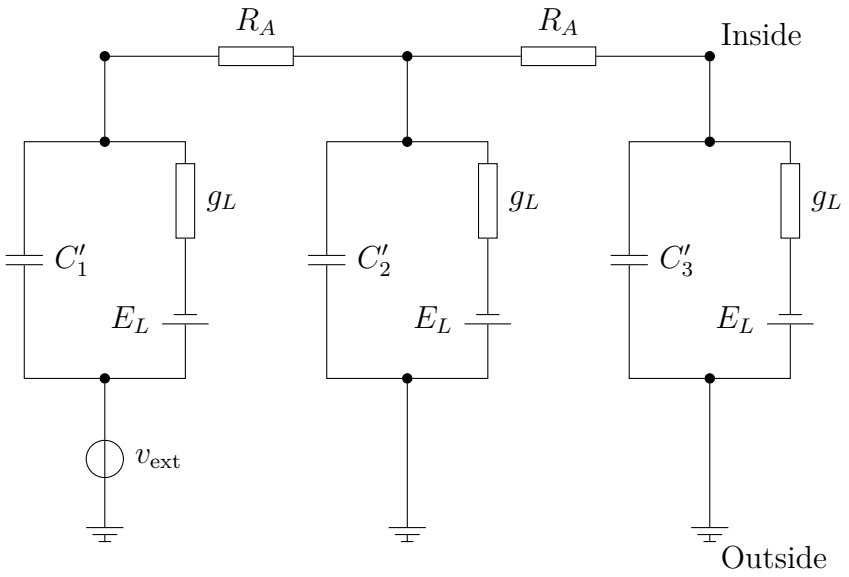

Figure 2.23: Simplified three-compartment model of an ANF. The model includes capacitance $C'_{\{1,2,3\}}$ and passive conductance g_L.

Parameter (NEURON symbol)	Value
Segment's length (L)	$10\,\mu\text{m}$
Segment's diameter (diam)	$1.5\,\mu\text{m}$
Axial resistivity (Ra)	$100\,\Omega\,\text{cm}$
Passive conductance (g_pas)	$1 \times 10^{-5}\,\text{S}\,\text{cm}^2$
Reversal potential (e_pas)	$-78\,\text{mV}$
Capacitance (cm)	$1\,\text{nF}\,\text{cm}^{-2}$

Table 2.2: Parameters of a simplified three-compartment ANF model used in numerical NEURON (Carnevale and Hines 2006) simulations.

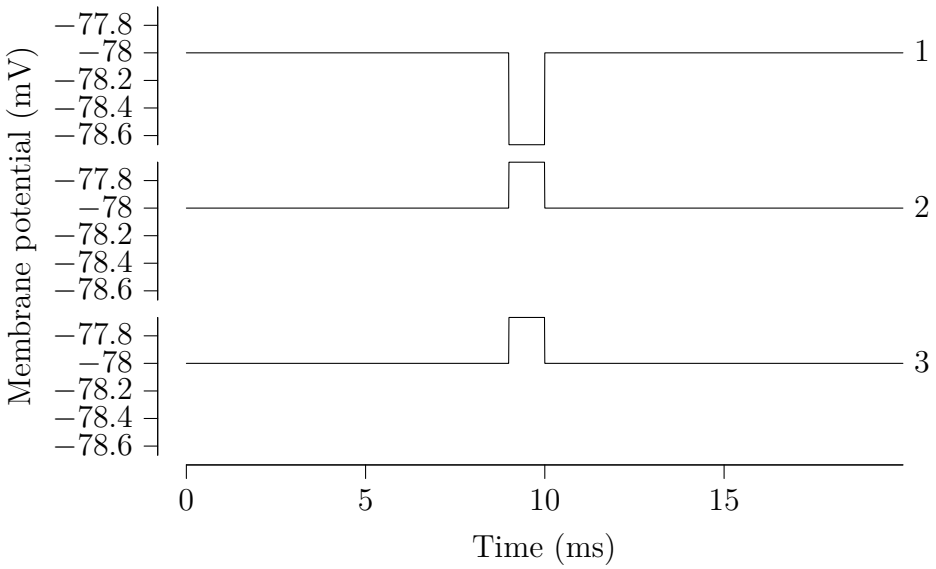

Figure 2.24: Membrane potentials of a simplified neuron model with three compartments during stimulation by an anodic pulse. All sections have equal capacitance.

the numerical solution. The polarity of the directly stimulated section is inverse compared to the stimulus. The polarity of the neighboring compartments is in phase with the stimulus. Most importantly, the absolute membrane potential of the directly stimulated section is higher than that of the other sections.

When the capacitance of the fist section increased 100 times ($0.1\,\mu\mathrm{F\,cm^{-2}}$), the membrane potentials of the segments changed as shown in Figure 2.25. It is equivalent to the analytic case where $C_1 \gg C_2$ which implies that the membrane voltage V_1 at the first compartment is small and the peak voltages at the other sections were higher.

The key result of the analysis and the simulations of the two simplified models is the distinction between two situations:

1. When the electrode is placed next to the normal or low capacitive section, then the maximum absolute membrane voltage occurs at that section and has the opposite polarity of the stimulus.

2. When the electrode is placed next to the high capacitve section, then the maximum absolute voltage occurs at the neighboring sections and has the same polarity as the stimulus.

In other words, the polarization of the membrane depends not only on the polarity of the stimulus but also on the relative capacitance of the sections. For example, let the firing threshold for a given stimulus $s(t)$ be lower than for the stimulus

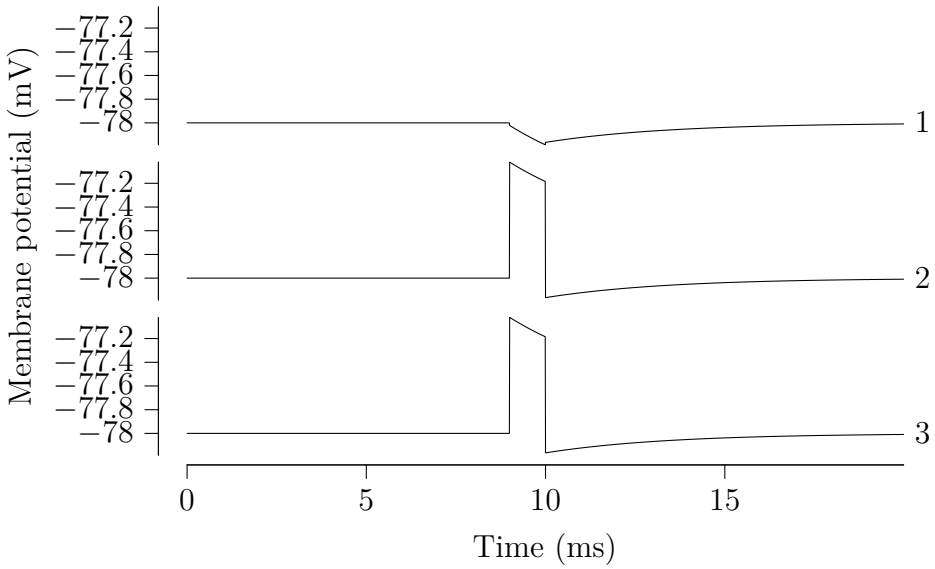

Figure 2.25: Membrane potentials of a simplified neuron model with three compartments during stimulation by an anodic pulse. The first compartment has the highest capacitance.

$-s(t)$ and all segments have a similar capacitance (the 1st case). If we significantly increase the capacitance of the section next to the electrode (the 2nd case), then we get a change of the efficiencies between $s(t)$ and $-s(t)$. In the second case, the detection threshold of the stimulus $s(t)$ would be higher than the threshold for the stimulus $-s(t)$.

Finally, the simulations of the original multi-compartment ANF from Section 2.2.1 show the same effect. This model contains nodes of Ranvier with Hodgkin–Huxley channels. It was stimulated by a sub-threshold triphasic pulse from an electrode that was close to the 5th node of Ranvier (which is the same as the 9th compartment) at the coordinates $x = 1010\,\mu\text{m}$ and $y = 50\,\mu\text{m}$). The stimulus was a symmetric triphasic pulse (CAC) with the duration of each phase of $40\,\mu\text{s}$. Two different configurations of the membrane capacitance were considered:

1. Normal, where the terminal node (the node with the highest capacitance) was the first node of the neuron and was located away from the electrode.

2. Modified, where the terminal node was swapped with the 5th node of Ranvier, i.e., the 9th segment, so that it was located next to the electrode.

In the normal case, the biggest membrane potentials occurred directly next to the electrode as shown in Figure 2.26. The polarity of the membrane voltage was opposite to the stimulus. In the modified case, the side lobes became much more

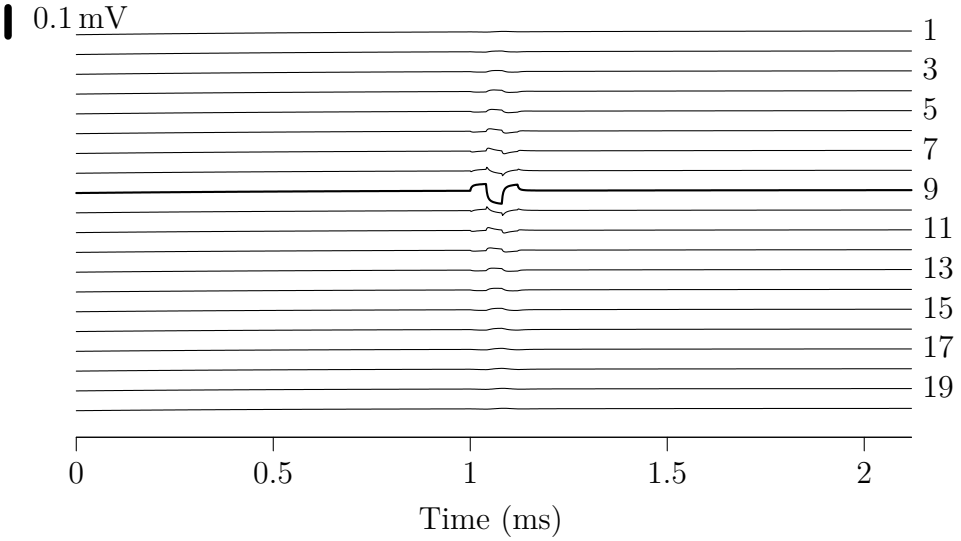

Figure 2.26: Membrane voltages of the normal multicompartment ANF model stimulated with a CAC pulse by an electrode next to the 5th node of Ranvier, i.e., the 9th section.

prominent compared to the main stimulation lobe. The polarity of the side lobes was the same as of the stimulus.

The effect of the membrane capacitance in the complete ANF model is more complex than in the simplified two- and three-compartment models. In the case of the simplified models, the electric field was applied only to a single compartment. In the full model, the field is applied to all compartments, which reduces the effect of the single high-capacitance node on the stimulation. In the above example, the effect was intensified, because of the very short pulses and the time needed to charge the high-capacitance node. Overall, the effect seems to be less prominent in the full model compared to the simplified models. Figure 2.28 shows the actual threshold differences at various electrode positions for a model with a high capacitance node ("terminal" node) in the middle of a neuron. Introduction of the high-capacitance node changed the efficiencies for ACA and CAC pulses for electrode locations around that node. This figure can be compared with Figure 2.21 which shows the same experiment with the terminal node at its usual location.

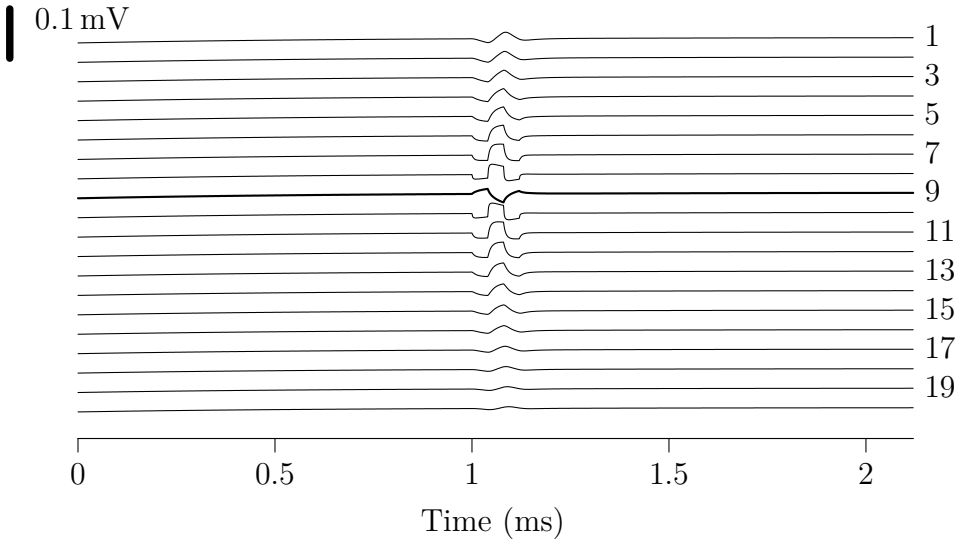

Figure 2.27: Membrane voltages of the modified multicompartment ANF model stimulated with a CAC pulse by an electrode next to the 5th node of Ranvier (the 9th section).

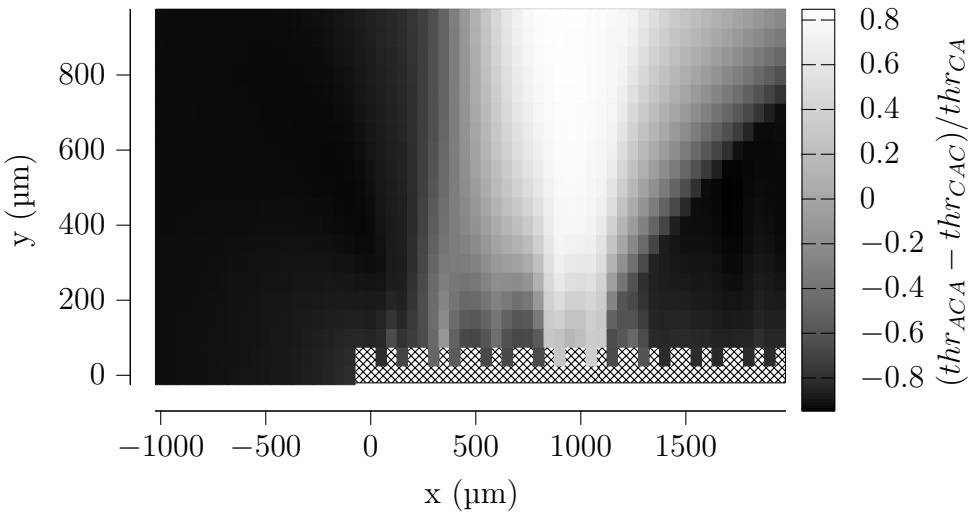

Figure 2.28: Normalized threshold difference between ACA and CAC pulses for various locations of the electrode around a modified ANF. The modified ANF had the terminal node swapped with the 5th node of Ranvier (the 9th section). As a result, there was high-capacitance node in the middle of the neuron. Compare with Figure 2.21, where the terminal node was located at the end of the neuron (1st section).

Chapter 3

Comparison of Globular Bushy Cell Models with Different Levels of Synaptic Depression in *in vivo*-like Simulations

3.1 Introduction

Globular bushy cell (GBC) are located in the ventral cochlear nucleus (VCN), which is the first processing station in the central auditory nervous system. The cochlear nucleus (CN) receives direct inputs from the inner ear through ANFs. In addition to globular bushy cells (GBCs), the population of neurons in VCN is made of several different types: spherical bushy cells, stellate cells, and octopus cells (Osen 1969; Rhode, Oertel, and Smith 1983). Each cell type processes different sound features, e.g., spectrum, temporal fine structure, or signal onset (Recio 2000). The pre-processing of sound by the CN neurons is essential for higher auditory centers to perform their functions, e.g., sound localization (Grothe, Pecka, and McAlpine 2010) or sound identification.

GBCs enhance temporal sound cues which are essential for sound localization. When stimulated with pure tones, their action potentials lock precisely to a certain phase of the signal. Some of the GBCs are experts in phase-locking and reach synchronization levels higher than any ANF. Neurons with such properties are sometimes called "high-sync" neurons (Joris, Carney, et al. 1994). Additionally, they can fire an action potential every stimulus cycle up to 700 Hz, which is more than twice the maximum firing rate for ANFs. GBCs similarly show increased synchronization and entrainment in response to complex sounds (Rhode and S. Greenberg 1994).

Rothman, Young, and Manis (1993) explained the mechanism of high synchronization (temporal precision of spikes) and high entrainment (one spike for each stimulus cycle) by the presence of many converging inputs. GBCs receive their main excitatory inputs from ANFs directly onto the soma through large synapses called modified endbulbs of Held (Spirou, Rager, and Manis 2005). To elicit an action potential, multiple subthreshold ANF input spikes must coincide. As a result, GBC spikes have greater temporal precision than the input action potentials from individual ANFs.

In most *in vitro* experiments, the strength of the excitatory inputs (excitatory postsynaptic currents, EPSC, synaptic strength) is strongly reduced after a presynaptic spike as shown in Figure 3.3. In the time between two input spikes, the synaptic strength recovers and if the pause between stimulations is long enough, it eventually reaches its original value (Yang and Xu-Friedman 2009; Y. Wang and Manis 2008; Yang and Xu-Friedman 2015). This synaptic depression at the endbulb of Held is associated mostly with the depletion of neurotransmitter at the presynaptic site (Friauf, Fischer, and Fuhr 2015) and receptor desensitization (Yang and Xu-Friedman 2008). The level of depression depends strongly on the stimulation frequency (Yang and Xu-Friedman 2009). A similar behavious was observed in a similar auditory synapse in medial nucleus of the trapezoid body, calyx of Held (Taschenberger, Woehler, and Neher 2016). In contrast to *in vitro* experiments, *in vivo* extracellular recordings do not indicate strong variations of synaptic strength at the endbulbs of Held during stimulation (Kuenzel, Nerlich, et al. 2015; Kuenzel, Borst, and Heijden 2011; Young and Sachs 2008; Borst 2010). The few *in vivo* studies of endbulb of Held can be complemented with *in vivo* studies of calyx of Held, that shows slight decrease in synaptic strength only at high stimulation frequencies (Di Guilmi et al. 2014; Lorteije et al. 2009).

Currently, the difference between the *in vitro* and *in vivo* observations is not well understood. In particular, how the different levels of depression influence the firing properties in response to sounds is unclear. Both endbulb and calyx of Held are regarded as "model synapses." It is therefore important to obtain a precise understanding of their operation. In this study, a biophysically plausible computational model of GBCs, which is driven by realistic *in vivo*-like stimuli, is presented. The main goals of the study were:

- To optimize the synaptic parameters of endbulbs of Held to accurately simulate GBCs including "high-sync" neurons (Sections 3.2.1 and 3.2.3).

- To better understand the behavior of synapses with different depression levels (from tonic, through weakly depressing, to strongly depressing as seen in *in vitro* experiments) in *in vivo*-like simulations (Figure 3.5, Sections 3.3.1 and 3.3.3).

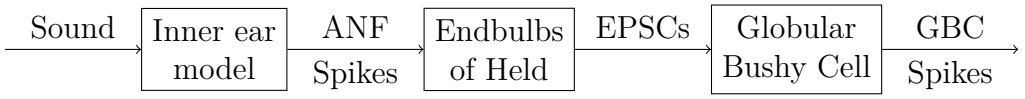

Figure 3.1: Block diagram of the GBC model. ANFs converge onto a soma of a GBC and excite it through large synapses (endbulbs of Held).

- To demonstrate how the higher number of ANF inputs increases the firing rate and the entrainment of bushy cells (Section 3.3.2). Experimental evidence shows similar variability (Spirou, Rager, and Manis 2005; Joris, Carney, et al. 1994).

- To provide a more comprehensive auditory model by combining an inner ear model with a GBC model, that can be used for further processing, e.g., for sound localization models. In this case, it is not sufficient that both models independently generate realistic outputs but also their combination, which provides further constraints.

Some of the results of this chapter were also published in (Rudnicki and Hemmert 2017).

3.2 Methods

3.2.1 Model Overview

The model consisted of three main components: (1) ANF inputs generated by an inner ear model (M. S. A. Zilany, Bruce, and Carney 2014), (2) endbulbs of Held, and (3) a soma of a bushy cell. The general structure is shown in Figure 3.1 and was derived from the previous work of Rothman, Young, and Manis (1993).

First, the sound enters the cat inner ear model by M. S. A. Zilany, Bruce, and Carney (2014) and is converted to ANF spike trains. The model of M. S. A. Zilany, Bruce, and Carney (2014) is a state-of-the-art model capable of generating ANF responses with typical adaptation properties an with realistic phase locking (M. S. A. Zilany, Bruce, P. C. Nelson, et al. 2009). The model includes several processing stages, such as a basilar membrane, inner hair cells, power-law dynamics at the inner hair cell synapses, and spike generators.

Next, a number of ANF spike trains was selected to drive synapses that were attached to the soma of the bushy cell. According to an electron microscopy study by Spirou, Rager, and Manis (2005), the number of ANF inputs shows large variations: between 9 and 69 ANF inputs across a population of 12 bushy cells. GBCs with the number of inputs varying from 10 to 70 per bushy cell were

simulated. The inputs were coming solely from high-spontaneous rate fibers. LSR and MSR fibers were neglected after, because a small number of them does not have significant influence on the firing properties in the simulated experiments (Liberman 1991). The model synapses were instantly activated by ANF input spikes and had an exponential decay of the conductance with a short 0.2 ms time constant (Yang and Xu-Friedman 2009; Cao and Oertel 2010). The summation of multiple synaptic conductances was linear. With respect to synaptic depression, three different synapse types were examined: (1) a tonic synapse model, (2) single exponential recovery synapse with different levels of synaptic depression, and (3) double exponential recovery synapse tuned to *in vitro* experiments (Section 3.2.2).

The final component of the model was the soma of a GBC. The dendritic trees were neglected, because the dendritic inputs are not well known and somatic ANF inputs are the major ones (Spirou, Rager, and Manis 2005). Each GBC was modeled as a single compartment with Hodgkin–Huxley-like channels (Rothman and Manis 2003a; Rothman and Manis 2003b; Rothman and Manis 2003c) described by the following equation:

$$I = C\frac{dV}{dt} + I_{\text{leak}} + I_{\text{Na}} + I_{\text{Kht}} + I_{\text{Klt}} + I_{\text{h}}, \tag{3.1}$$

where I is the membrane current, C is the membrane capacity, V denotes the membrane voltage, I_{Klt} is the fast-activating slow-inactivating low-threshold K^+ current, I_{Kht} is the high-threshold K^+ current, I_{h} is the hyperpolarization-activated cation current, I_{leak} is the leakage current, and I_{Na} is the Na^+ current. The model was derived directly from Rothman and Manis (2003c) with the exception of sodium channels taken from Spirou, Rager, and Manis (2005). The original sodium channels produced unrealistically long refractory periods and needed to be replaced by channels with faster dynamics. The substitution resulted in the absolute refractory period of 0.66 ms. All channel parameters are summarized in Table 1 (Model Type II) of (Rothman and Manis 2003c) and in the Appendix of (Spirou, Rager, and Manis 2005) with the following adjustments. Time constants were corrected for the *in vivo* temperature of 37 °C using $Q_{10} = 2.5$ for sodium and $Q_{10} = 1.5$ for all other channels. To match measured firing thresholds (Yang and Xu-Friedman 2009), the maximum Na^+ channel conductance was increased to 2500 nS.

3.2.2 Modeling of Synaptic Depression

Table 3.1 lists synapse models used in this study.

The tonic synapse was the first and the simplest model that was examined. The synaptic weight was constant and resulted in constant EPSCs that did not depend on the ANF firing rates. Even though endbulbs of Held might not be perfectly

Name	Description
tonic	constant synaptic weight
X%-depressing	synapse with a single exponential recovery depressing by $X\%$ when stimulated at 300 Hz (equation 3.3)
YXF09m	synapse with a double exponential recovery and mean parameters of an endbulb population from *in vitro* experiments by Yang and Xu-Friedman (2009)

Table 3.1: Synapse types

tonic synapses, especially at higher stimulation rates (Borst 2010; Young and Sachs 2008), this model is equivalent to a 0%-depressing synapse and defines the bound of the parameter space.

The second model was a depressing synapse with a single exponential recovery (Tsodyks and Markram 1997) which was referred as X%-depressing synapse throughout this study. The purpose of this model was to examine a wide range of synaptic depressions spanning from strong *in vitro* to weak depression observed in some *in vivo* experiments. The synapses were fitted only in the *in vivo* operational stimulation range. The peak synaptic conductance was proportional to the active internal synaptic resources. Every pre-synaptic spike caused an activation of some synaptic resources. Between the spikes, the synapse could recover exponentially. This process can be expressed iteratively with equation 3.2:

$$g_{n+1} = g_n(1-u)e^{-\Delta t/\tau} + w(1-e^{-\Delta t/\tau}), \tag{3.2}$$

where w is the peak conductance of a completely recovered synapse, u is the fraction of available synaptic resources activated at each stimulation. As stated by Tsodyks and Markram (1997), depending on the physical mechanisms, u can be partially or completely determined by release probability of the neurotransmitter triggered by a presynaptic spike. Δt is the time from the last (n-th) synaptic event, and τ is the synaptic recovery time constant. τ was set to 90 ms based on *in vitro* experiments with *in vivo*-like stimuli of endbulbs (Yang and Xu-Friedman 2015) and calyx of Held (Hermann, Grothe, and Klug 2009). The initial value of g (g_0) was set to $w/(1-u)$ so that g_1 had the peak conductance of w. The depression level $X\%$ is defined as a relative decrease of steady-state synaptic strength s_f between the spontaneous rate (SR) ($f = 50$ Hz) and the driven rate ($f = 300$ Hz). It can be calculated with equation 3.3:

$$X\% = (1 - \frac{s_{300\text{ Hz}}}{s_{50\text{ Hz}}}) \cdot 100. \tag{3.3}$$

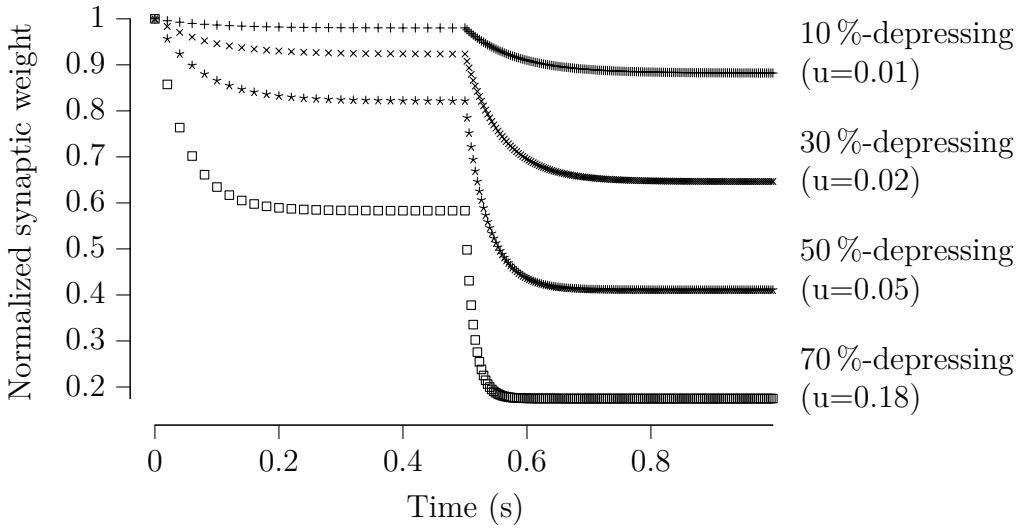

Figure 3.2: Normalized peak synaptic weights of single exponential recovery synapses stimulated at two different frequencies. The stimulation in the first interval (0 s to 0.5 s) was 50 Hz (approx. SR of the input), and 300 Hz (approx. max rate of input) in the second one (0.5 s to 1 s). The steady states in each interval (s_f) were used to calculate the effective depression level ($X\%$) using equation 3.3. All synapses share the same recovery time constant but have different values of u.

The value of $X\%$ can be set by adjusting u in the model, because it directly changes the steady-state synaptic weights (s_f) as shown in Figure 3.2. The stimulation frequencies of 50 Hz and 300 Hz were chosen as they correspond approximately to an input operational range bound by the spontaneous and driven rates of ANFs. In other studies, especially *in vitro*, $X\%$ can have a different meaning and refer to depression relative to an unconditioned synapse. As a result, the depression values are typically much higher in *in vitro* synapses.

The third synapse model was a depressing synapse with a double exponential recovery. It is called YXF09m here, because it is based on the mean *in vitro* data from Yang and Xu-Friedman (2009). The purpose of this model is to replicate behavior of synapses measured *in vitro* and validate them in simulated *in vivo*-like conditions. In their experiments, Yang and Xu-Friedman (2009) observed two exponential components in the recovery of EPSCs. Thus a model based on double exponential recovery, such as (Cook et al. 2003), was a natural match to the experimental data. The model is described by equation 3.4 and the parameters were set to the mean values of the population from (Yang and Xu-Friedman 2009).

$$\begin{aligned} g_{n+1} = k\left(g_n(1-u)e^{-\Delta t/\tau_f} + w(1-e^{-\Delta t/\tau_f})\right) + \\ +(1-k)\left(g_n(1-u)e^{-\Delta t/\tau_s} + w(1-e^{-\Delta t/\tau_s})\right), \end{aligned} \tag{3.4}$$

where w is the peak conductance of a completely recovered synapse, u is the fraction of the available synaptic resources being utilized at presynaptic event. This value was interpreted as the vesicle release probability of 0.6, that was found for endbulbs of Held *in vitro* (Oleskevich, Clements, and Walmsley 2000). Δt is the time from the last (n-th) synaptic event, τ_s (1990 ms) and τ_f (10.9 ms) are the slow and fast synaptic recovery time constants, respectively, and k (0.3) is the fraction of the fast recovery (relative to the slow recovery). The initial value of g (g_0) was set to $w/(1-u)$. The model exhibits different depression levels depending on the stimulation frequency. Figure 3.3 shows normalized EPSC of the model with different values of u for reference that was stimulated at 100 Hz, 200 Hz, and 333 Hz. They grayed area corresponds to the population data obtained in an analogous *in vitro* experiment from Yang and Xu-Friedman (2009).

It is worth to note that Eq. 3.2 describing X%-depressing models can be derived from Eq. 3.4 of the YXF09m model by setting k to 1. Also, the tonic synapse is a special case of X%-depressing model, where $X = 0$. However, because the models have different motivations and were fitted differently, they are presented as three distinct models in this study.

3.2.3 Fitting of synaptic weights

Modeling of GBCs, and "high-sync" neurons in particular, required adjustment of synaptic weights of the endbulbs of Held. The experiments of Joris, Carney, et al. (1994) were used as a reference for this procedure. In our simulations, bushy cells were simulated with a *in vivo*-like stimulation protocol which consists of several steps:

1. A signal was generated. It consisted of 100 gated tones that were repeated every 100 ms and each tone lasted 25 ms. The frequency of the tones was equal to the CF of the stimulated neuron and their intensity was 50 dB re 20 µPa.

2. An inner ear model driven by that signal was used to generate the ANF spike trains.

3. The ANF spike trains were used to stimulate models of endbulbs of Held and GBCs.

4. The output spike trains of GBCs were recorded.

After each simulation, VS, firing rate, and EI were calculated from responses of GBCs. "High-sync" neurons are defined in terms of VS > 0.9 for CF < 700 Hz (Joris, Carney, et al. 1994).

Generally, VS, EI, and SR were calculated for each combination of synapse type T (where $T \in \{$tonic, X%-depressing, YXF09m$\}$), ANF number of inputs N

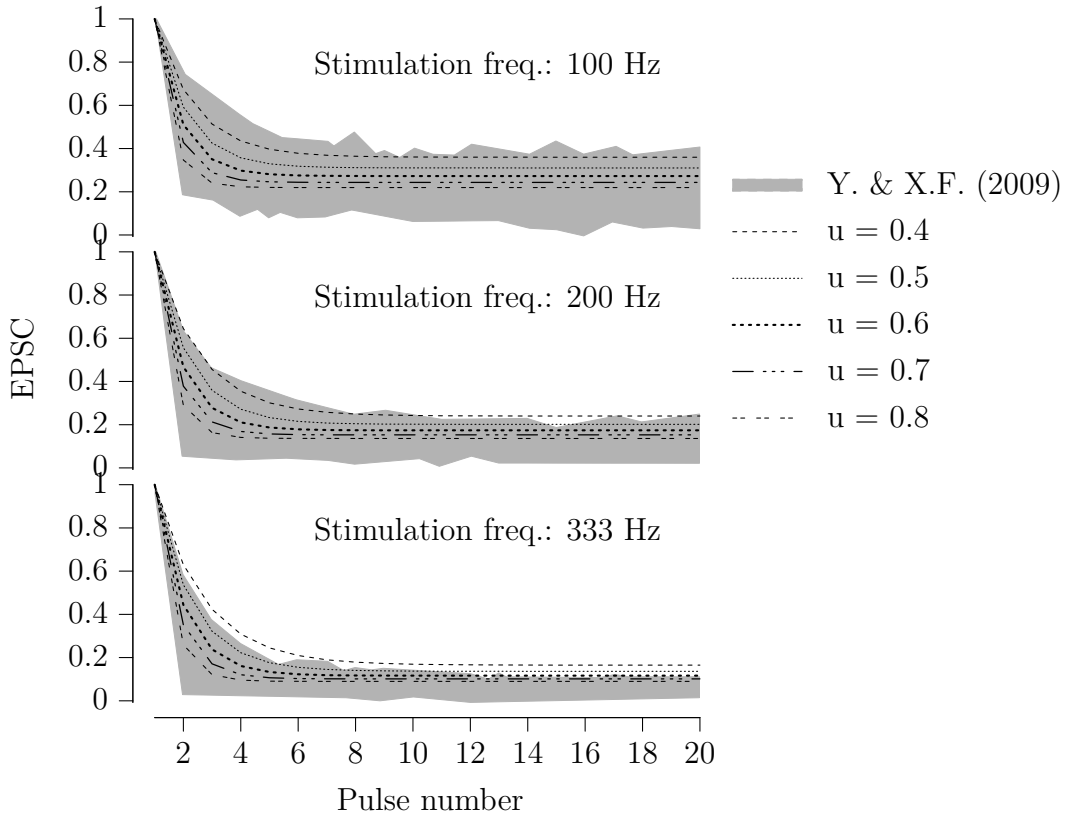

Figure 3.3: Synaptic depression of a double exponential recovery synapses (YXF09m) with different values of u that were stimulated at 100 Hz, 200 Hz, and 333 Hz. Synapse's recovery times constants were equal to the mean population values from *in vitro* experiments of Yang and Xu-Friedman (2009). The selected value of u was 0.6 as measured by Oleskevich, Clements, and Walmsley (2000) *in vitro*. The grayed are represents the population data from Yang and Xu-Friedman (2009).

(where $N \in [10, 70]$), and synaptic weight w. For simplicity, all synaptic weights had equal values for a given GBC. The parameter scan resulted in the following mapping: $(T, N, w) \rightarrow (VS, EI, SR)$. VS, EI, and SR can be seen as functions of w for all combinations of T and N: $VS_{T,N}(w)$, $EI_{T,N}(w)$, $SR_{T,N}(w)$. As an example, results with two synapse types and two different values of N are shown Figure 3.4.

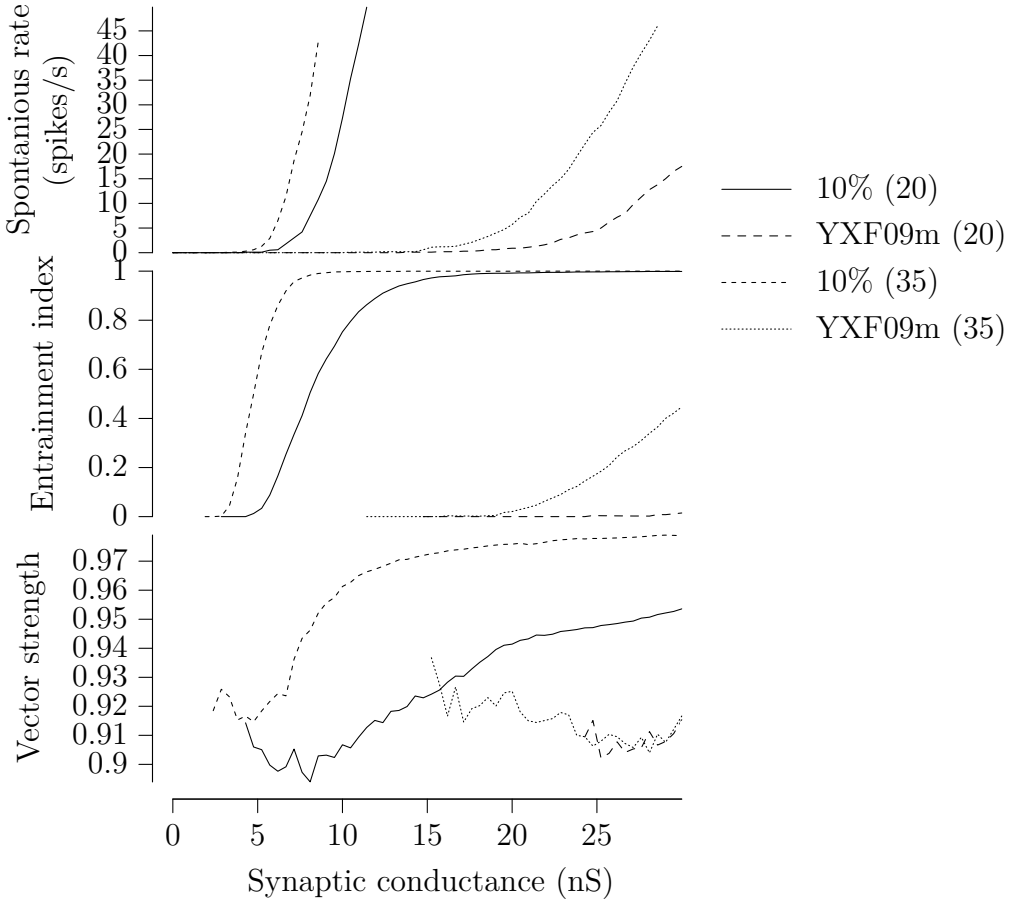

Figure 3.4: SR, EI, and VS as a function of synaptic weight for a combination of two synapse models (10%-depressing and YXF09m) and two different number of ANF inputs (20 and 35). SR and EI increase with increasing synaptic weight. VS also increases with synaptic weight for 10%-depressing synapses, but does not increase for synapses tuned to (Yang and Xu-Friedman 2009). The thin dotted black line marks the desired SR of 7.5 spikes/s (Spirou, Brownell, and Zidanic 1990).

On the one hand, an increase in w causes an increase in VS and EI, which is desirable for GBCs. On the other hand, increasing w can cause unrealistically

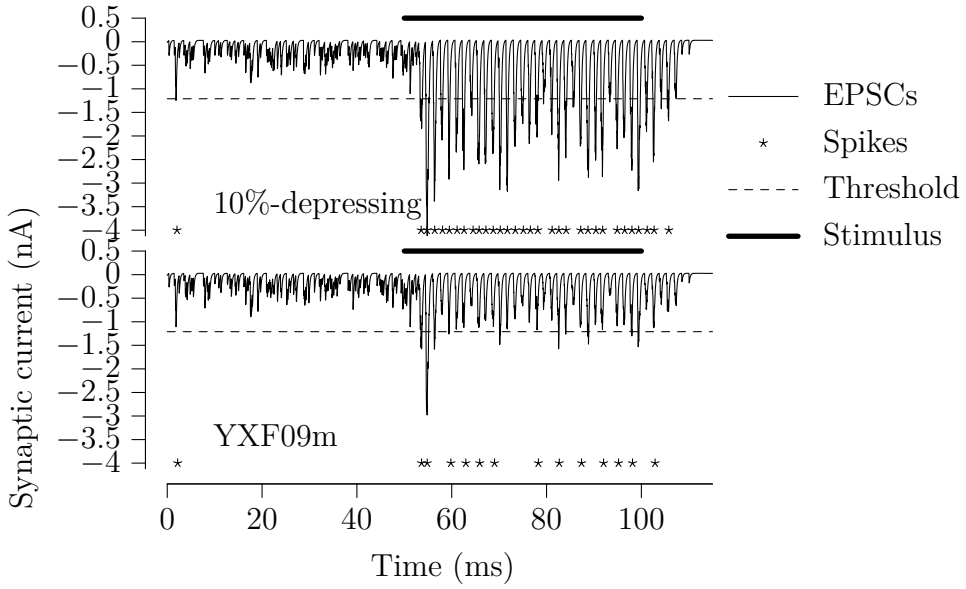

Figure 3.5: Postsynaptic currents of two GBCs with 10%-depressing and YXF09m synapses stimulated with a 50 ms pure tone of 650 Hz (green bar). The dashed line is plotted for reference and indicates a threshold for a single EPSC to initiate an action potential. Red stars indicate action potentials triggered by the stimulation. The less depressing synapses (10%-depressing) produced more action potentials than the more depressing synapses (YXF09m, Table 3.1). The SR for both cells was 7.5 spikes/s.

high SR. As a result, the optimal weights were found by increasing the value of w up to the point where $SR_{T,N}(w)$ crossed the mean experimental SR from Spirou, Brownell, and Zidanic (1990) which equals to (7.5 ± 13.8) spikes/s and is valid only for GBCs with CF <6 kHz. The procedure of finding the best weight w_o is equivalent to Eq. 3.5:

$$w_o = \arg\min_w |SR(w) - SR_t|, \tag{3.5}$$

where SR_t is the target spontaneous rate (7.5 spikes/s). The procedure of finding optimal weights is further discussed in Section 3.4.1.

Figure 3.5 shows postsynaptic currents of two GBCs with 10%-depressing and YXF09m synapses (Table 3.1) having optimal weights. The GBCs were stimulated with a 50 ms pure tone of 650 Hz. Each plot has a corresponding curve in Figure 3.4 with 35 ANF inputs. The optimal synaptic weights can be found in Figure 3.4 at the intersection of the target SR (dotted line, 7.5 spikes/s) and the corresponding curves. The optimal synaptic weights for all analyzed synapse types and number of inputs are plotted in Figure 3.6.

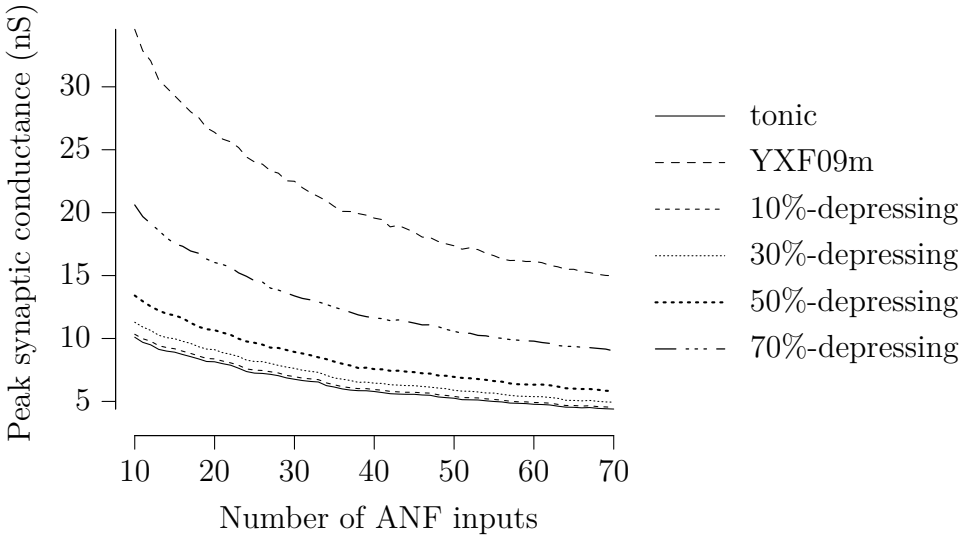

Figure 3.6: Optimal peak synaptic conductance as a function of the number of ANF inputs to a GBC and the synapse type (depression level).

3.2.4 Implementation details

The model of GBCs was implemented in the NEURON simulation environment (Carnevale and Hines 2006) and can be freely accessed, studied, and improved at `https://github.com/mrkrd/cochlear_nucleus` (Rudnicki and Hemmert 2017–). Python programming language was used to manage the simulations and analyze the data. The model input was generated using the free *cochlea* Python library, which was made publicly available at (Rudnicki and Hemmert 2009–). Specifically, the library includes the inner ear model of M. S. A. Zilany, Bruce, and Carney (2014).

3.3 Results

This study mainly aimed to investigate the influence of different synapse types (tonic, with single, and with double exponential recovery), depression levels (0 % to 70 %), and the number of ANF inputs (10 to 70) on the firing properties of bushy cells. The input *in vivo*-like stimulation patterns were used to analyze responses of the GBCs. The reference data came primarily from *in vivo* experiments of Joris, Carney, et al. (1994).

3.3.1 Influence of Synaptic Depression on Synchronization and Entrainment

In the first set of simulations, I examined how different synapse types and depression levels influence synchronization and entrainment for cells with different CFs. the number of ANF inputs was kept constant, so every GBC was connected to 40 HSR fibers. The stimulus was a train of 100 ramped pure tones (50 ms, 60 dB re 20 µPa) at CF (Joris, Carney, et al. 1994).

Consistently with previous studies (Xu-Friedman and Regehr 2005; Joris and Smith 2008; Rothman, Young, and Manis 1993), GBCs improved phase locking relative to ANFs in the low-frequency range up to approximately 1.5 kHz. Synchronization was similar for all synaptic models and depression levels, in good agreement with experimental data. However, there was a large difference between entrainment for synapses with different depression levels. The EI was unrealistically low for depression levels >50 % between 400 Hz and 800 Hz. The synapse with *in vitro*-like depression and double exponential recovery (Yang and Xu-Friedman 2009) failed to drive GBCs above 400 spikes/s. Synapses with depression levels from 0 % to 50 % produced EI in the range of the reference data.

3.3.2 Influence of the Number of Inputs on Synchronization and Entrainment

Spirou, Rager, and Manis (2005) found a large variability (9 to 69) of ANF inputs converging onto the soma of individual GBCs. To examine the influence of the number of inputs on phase locking and entrainment, different convergence patterns were analyzed. The number of input ranged from 20 to 50 for a 10%-depressing synapse. Because "high-sync" neurons are of the main interest, this study focused on bushy cells with average and high numbers of inputs. Figure 3.8 shows both the VS and EI for the simulated GBCs. For reference, the original experimental data from (Joris, Carney, et al. 1994) (triangles and stars) and simulated ANFs (dotted line) was included in the plots. Figure 3.8 shows that the number of inputs has a strong effect on entrainment. High EI values for CFs up to 700 Hz could be reached only with a large number (50) of converging ANFs; smaller numbers of inputs caused a degradation of the EI. The change of entrainment due to a variation in the number of ANF inputs reflects the variability of the experimental data. The entire range of the measured data points was covered merely using a simple variation of the number of ANF inputs. It is further quantified in Section 3.3.3 where all data points were fitted to models by changing the number of ANF inputs. Compared to entrainment, the number of inputs had a smaller effect on phase locking, with a decreased number of ANF inputs leading to only a slight decrease of the VS.

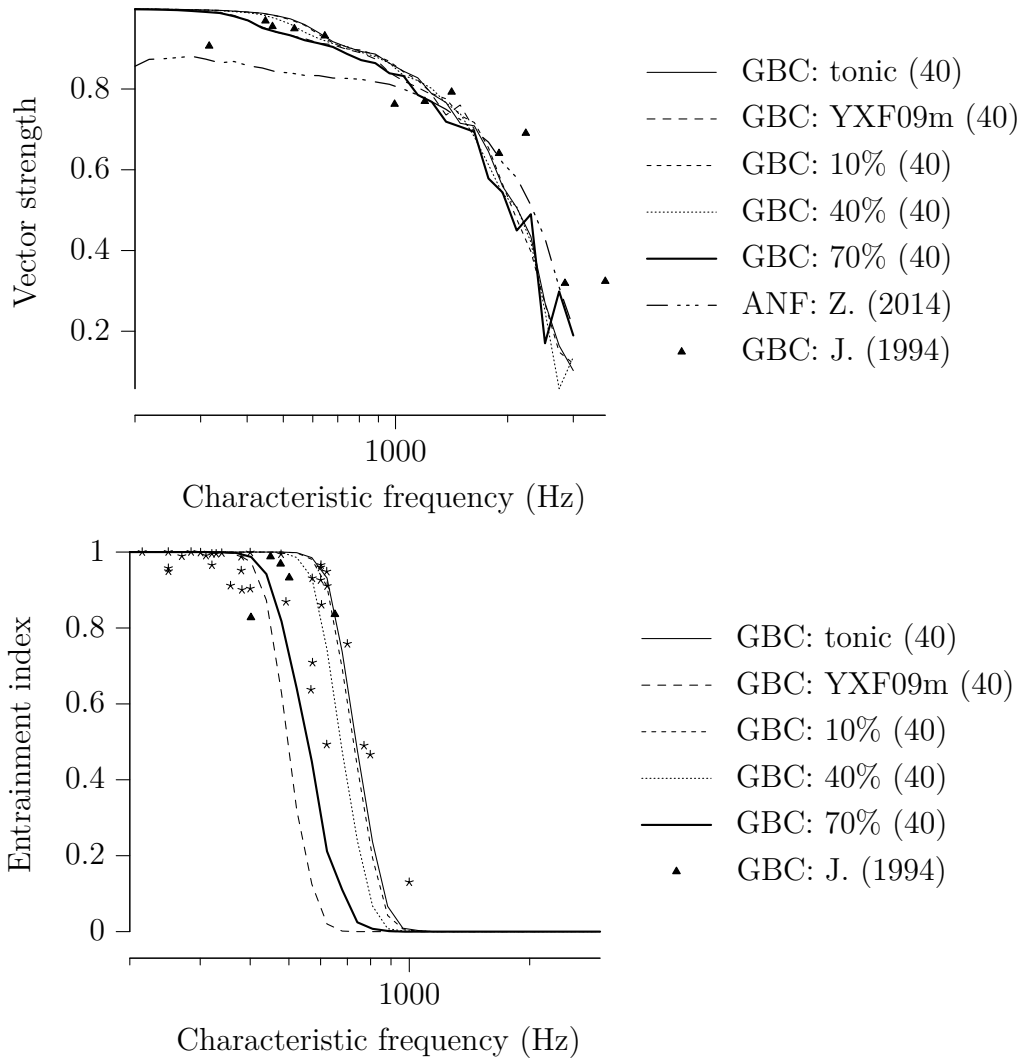

Figure 3.7: Influence of synaptic depression on synchronization and entrainment. The points in the plots represent experimental data digitized from (Joris, Carney, et al. 1994). Each GBC was excited by 40 high SR ANFs. The VS of the simulated ANFs by M. S. A. Zilany, Bruce, and Carney (2014) is shown in the upper panel.

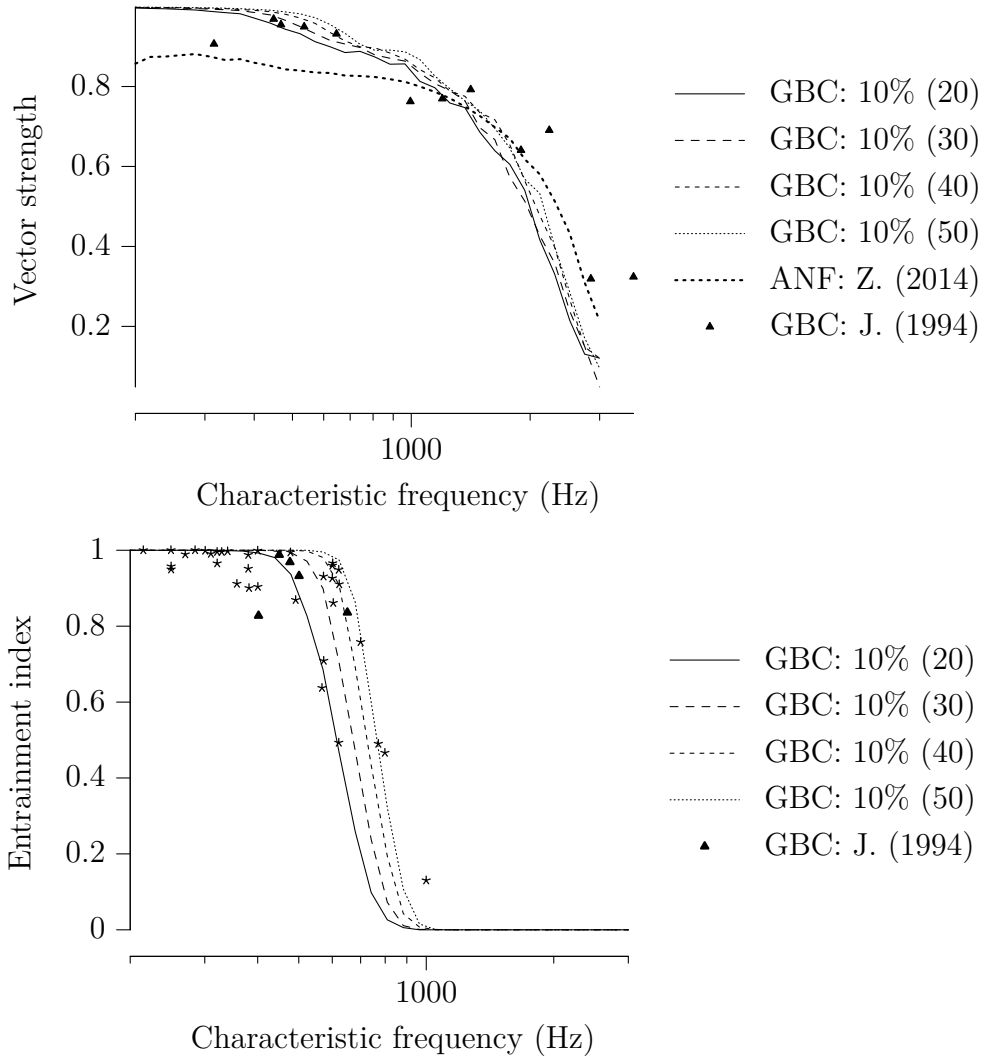

Figure 3.8: Influence of the number of ANF inputs (20, 30, 40, and 50) on synchronization and entrainment. While the number of inputs only slightly influenced the VS, the effect on EI was strong. The variability of the experimental data can be explained in the model by the variation in the number of inputs to GBC. The upper panel shows the VS of the simulated input ANFs from M. S. A. Zilany, Bruce, and Carney (2014). The experimental reference data for GBCs is from Joris, Carney, et al. (1994).

3.3.3 Fitting the Number of Inputs and the Type of Synapse to Individual Data Points of Entrainment Index

Previous simulations showed that VS does not change significantly for different synapse types (depression levels, Figure 3.7) or the number of ANF inputs (Figure 3.8). At the same time, EI strongly depends on both. To have better insight into the combined effect of the parameters, each synapse type was fitted to every experimental data point from the EI plot from Joris, Carney, et al. (1994). The same data points are plotted in the lower panels of Figure 3.7 and Figure 3.8. The results of the fitting are shown in Figure 3.9 where gray levels encode the number of ANF inputs that was necessary to fit the data for each model. For clarity, only the frequencies in the transition region (CF >500 Hz), in which EI degrades, was plotted. Data in the low frequency region (CF <500 Hz) could be reproduced by any synapse model given enough ANF inputs, which is also visible in Figure 3.7 and Figure 3.8. The possible number of ANF inputs varied from 10 to 70 as observed by Spirou, Rager, and Manis (2005). They also discovered that the majority of GBCs receive 23 or less inputs. This constraint holds only for a few fitted GBCs in the transition region and is possible for synapses with small depression levels (0 % to 20 %). Other fitted GBCs required more inputs. Fields filled with pattern mean that it was not possible to fit the model to the given EI at the given CF. Models with depression > 50 % clould no longer reproduce data points with the highest CFs. The simulations also show that all (except one) EI data points could be reproduced by the less depressing models by varying the number of ANF inputs. SR of all modeled GBCs was set to 7.5 spikes/s. For completeness, Supplementary Material shows additional results for GBC models with higher SR.

3.3.4 Receptive Fields

It is not unusual that high-CF bushy cells have asymmetric receptive fields (Rhode 2008). It is because, they tend to phase lock to low-frequency high-intensity sounds and exhibit high firing rates at low frequencies.

In the simulation shown below, a high-CF bushy cell (CF = 5.6 kHz) was stimulated with pure tones and measured the average firing rate. Rhode (2008) conducted similar experiments and measured the receptive fields of several GBCs *in vivo*. In their study, animals were stimulated with a wide range of frequencies (0.1 kHz to 10 kHz) and intensities (0 dB re 20 µPa to 90 dB re 20 µPa). In Figure 3.10, the experimental data was plotted together with simulated results for tonic and strongly depressing synapses. Each line represents the firing rate for a given sound intensity from 0 dB re 20 µPa to 90 dB re 20 µPa in 10 dB increments. The reference data are shown by dotted lines and the model data by solid lines.

The tonic synapses could appropriately drive a bushy cell at the CF and low-

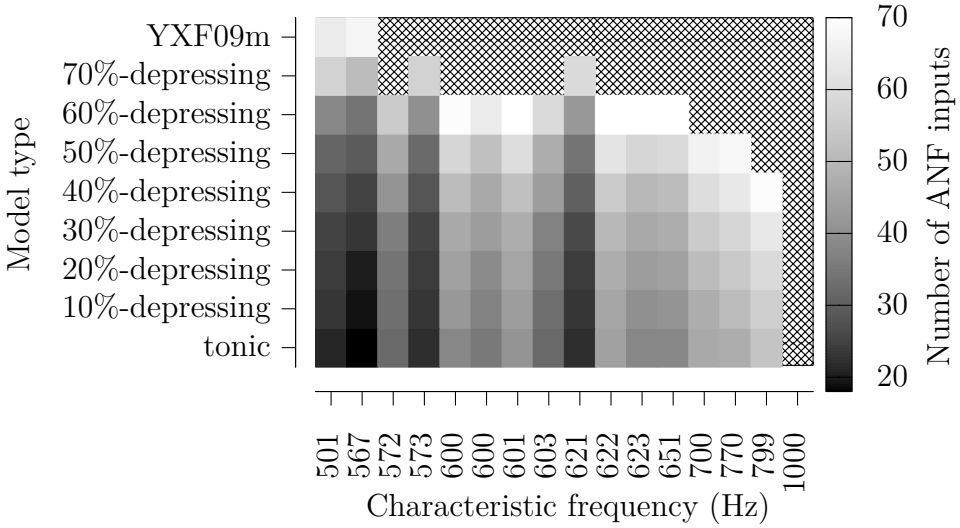

Figure 3.9: Fitting of the number of ANF inputs for every synapse type to EI data point from Joris, Carney, et al. (1994). Only data points with CF >500 Hz are shown for clarity. Gray levels encode the number of ANF inputs that were necessary to fit the data. Each data point is represented as a tuple (CF, EI) on the horizontal axis. The EI data points are also shown in the lower panels of Figure 3.7 and Figure 3.8. A white field means that no fit was possible for a given synapse type.

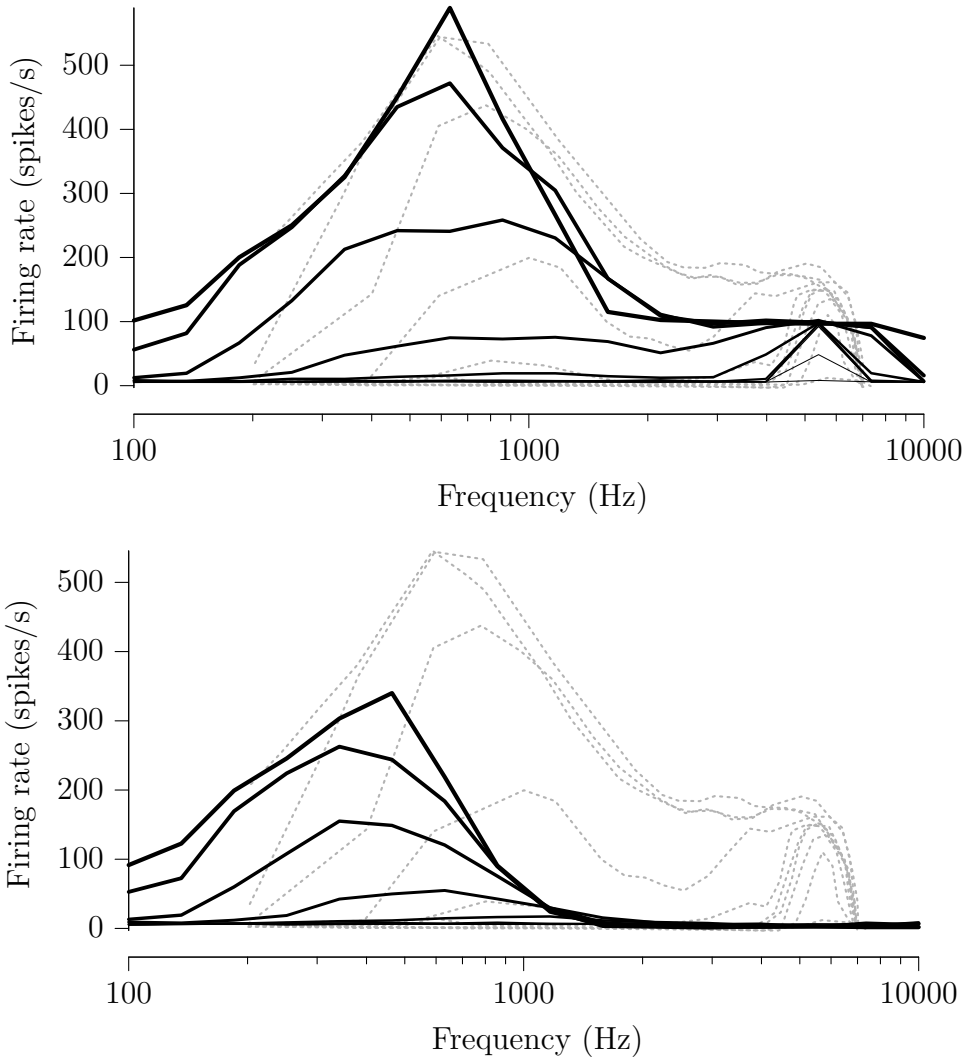

Figure 3.10: Receptive field maps for a GBC model (CF = 5.6 kHz) with tonic (upper panel) and strongly depressing (lower panel) synapses. Each line is an iso-intensity curve as a function of frequency. Intensities varied from 0 dB re 20 µPa to 90 dB re 20 µPa in 10 dB increments. The dotted black lines represent the experimental data from (Rhode 2008). High-CF neurons show higher entrainment for low-frequency sounds than for the tones at the CF. Therefore, at high sound levels, firing rates increase for frequencies below the CF. Only the model with tonic synapses could reproduce the measured receptive fields.

frequency tail. The 20 dB dynamic range of the model with tonic synapses was realistic, and the shape of the iso-intensity curves coincides quite well with the experimental data. However, strongly depressing synapses could not drive the neuron at the CF, showing a response only at the low-frequency tail where the response was driven by the slower ANF input rates.

3.3.5 Globular Bushy Cells with High Spontaneous Rates

Generally, GBCs can have various SRs (Rhode 2008). However, Spirou, Brownell, and Zidanic (1990) and Smith, Joris, and Yin (1993) observed correlation between SR and characteristic frequency (CF). They noticed that low-CF neurons tend to have low SR. This property was used throughout the chapter, which focused on low-CF (LSR) neurons. Here, results of GBC simulations with higher SRs (20 spikes/s and 50 spikes/s) are presented.

Figure 3.11 and Figure 3.12 show fitting of each synaptic model in the study to individual EI data points from Joris, Carney, et al. (1994). GBCs models in Figure 3.11 had the SR of 20 spikes/s and 50 spikes/s in Figure 3.12. Gray levels indicate the number of ANF inputs that was necessary to replicate a given EI at the given CF. Pattern indicates that no fit was possible. For clarity, only data from the transition region (CF >500 Hz) is shown, because the data for lower CF could be reproduced by all models.

Results show that GBCs with higher SRs require require less synaptic inputs for a given synapse type to replicate each data point. Additionally, GBCs with YXF09m synapses, modeled directly from *in vitro* experiments of Yang and Xu-Friedman (2009), could produce valid entrainment for some data points in the transition region. Finally, the data point at 1 kHz could be also replicated but only by synapses with limited depression and large number of ANF inputs at higher SRs.

3.4 Discussion

GBCs play a direct role in the sound localization pathway (Grothe, Pecka, and McAlpine 2010). They are highly specialized for that function because of fast channel kinetics and fast synapses. Together with multiple inputs from ANFs, such specialized features enable them to enhance the precision of temporal coding. The investigation showed how to optimally adjust synaptic weights for endbulbs of Held with different levels of depression to produce realistic GBC responses including "high-sync" neurons. Additionally, simulations showed that synapses with depression greater than 50 % can reproduce less data points than synapses with smaller depression. The depression is likely to be weaker (0 % to 20 %),

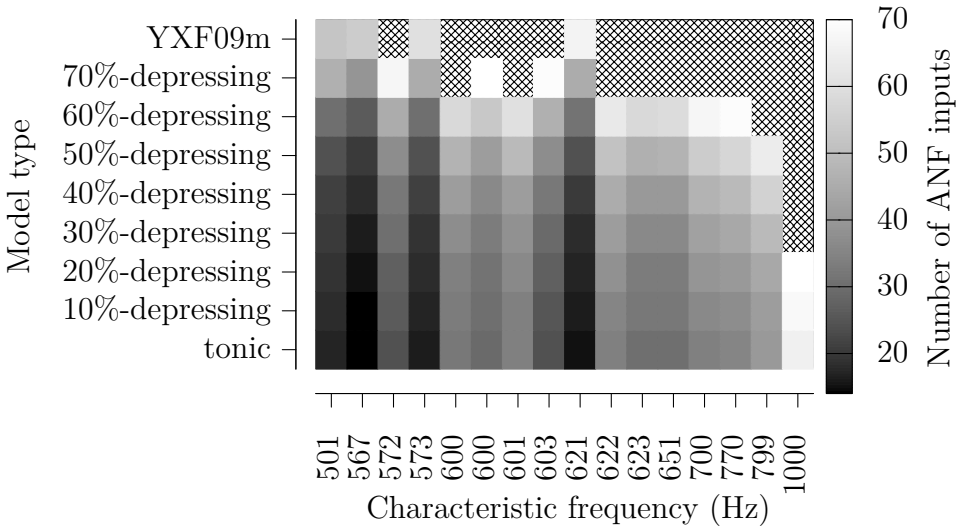

Figure 3.11: Fitting of the number of ANF inputs for every synapse type to individual EI data point from Joris, Carney, et al. (1994). Only data points with CF >500 Hz are shown for clarity. Gray levels encode the number of ANF inputs that were necessary to fit the data. Each data point is represented as a tuple (CF, EI) on the horizontal axis. The EI data points are also shown in the main manuscript in Figure 7 and Figure 8. White fields mean that no fit was possible for a given synapse type. The SR of GBC models was set to 20 spikes/s.

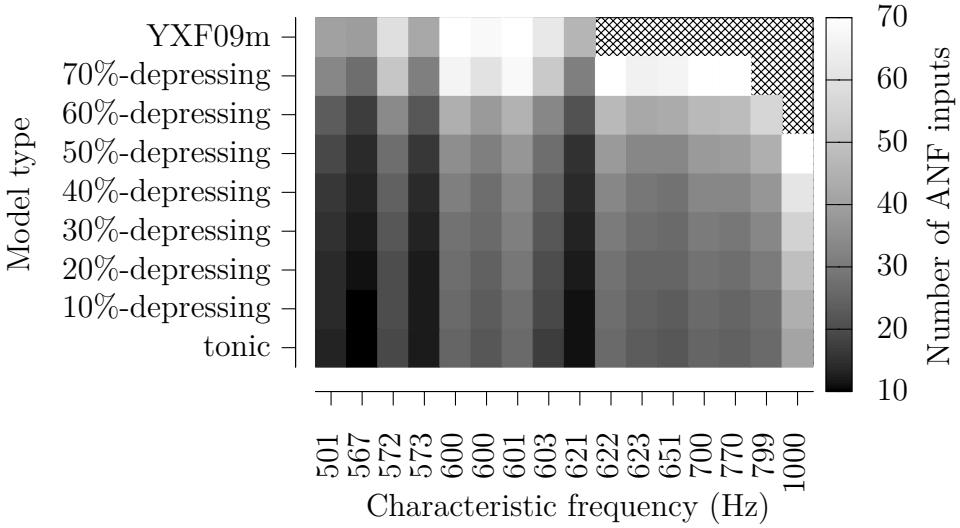

Figure 3.12: Fitting of the number of ANF inputs for every synapse type to individual EI data point from Joris, Carney, et al. (1994). Only data points with CF >500 Hz are shown for clarity. Gray levels encode the number of ANF inputs that were necessary to fit the data. Each data point is represented as a tuple (CF, EI) on the horizontal axis. The EI data points are also shown in the main manuscript in Figure 7 and Figure 8. White fields mean that no fit was possible for a given synapse type. The SR of GBC models was set to 50 spikes/s.

because strongly depressing synapses require much more ANF inputs. Synapses with exponential recovery mechanisms fitted to *in vitro* experiments with paired-pulse stimuli did not operate properly with *in vivo*-like stimuli in the most of the transition region (CF >500 Hz). It indicates that synaptic mechanisms which counteract vesicle depletion are activated *in-vivo*. It also shows that even though giant synapses have been studied in great detail before, it is still important to examine them as a part of a larger system, what provides further constrains. Finally, variation of the number of ANF inputs and synaptic depression can reproduce variability of entrainment observed *in vivo*. Last but not least, the modeled GBCs can generate realistic spike trains using a code that is freely available at `https://github.com/mrkrd/cochlear_nucleus` (Rudnicki and Hemmert 2017–) for researchers who are interested in investigating neuronal processing at higher stages of the auditory pathway, especially in sound localization (Encke and Hemmert 2015; Encke and Hemmert 2018).

3.4.1 Adjustment of Synaptic Weights

The model consisted of three main components: ANF inputs, endbulbs of Held and a GBC soma. The properties of ANF inputs and GBC soma had been well studied before. An accurate biophysical models with fixed parameters from M. S. A. Zilany, Bruce, and Carney (2014) and Rothman and Manis (2003c) was used. The inner ear model of M. S. A. Zilany, Bruce, and Carney (2014) allowed us to generate realistic *in vivo*-like ANF spike trains. GBC soma, despite being relatively realistic, still lacked features, such as multiple compartments and inhibitory inputs. In particular, inhibitory inputs might play an important role in GBCs as they do in spherical bushy cells (Keine and Rübsamen 2015; Nerlich et al. 2014; Kuenzel, Nerlich, et al. 2015). A phenomenological synapse models were used, which enabled to easily modify model parameters in a controllable way. As a result, the influence of various synaptic properties on the input-output characteristic of the system was analyzed. Consequentially, it was not possible to examine the exact biophysical mechanisms of depression.

Synaptic weights were fitted separately for each combination of synapse type and the number of synapses (ANF inputs). The main objective was to achieve large VS and EI while keeping the SR realistic. While the SR of GBCs can vary a lot (Rhode 2008), Spirou, Brownell, and Zidanic (1990) and Smith, Joris, and Yin (1993) observed correlation between SR and CF. They noticed that GBCs at low CFs tend to have low SR and GBCs at high CFs have higher spontaneous activity. Because the model was adjusted for GBCs with low CFs it might not be valid for GBCs with higher CFs and SRs. Additionally, Kopp-Scheinpflug et al. (2008) showed indirectly similar pattern, where principal neurons in medial nucleus of the trapezoid body (MNTB) with low CF tend to have lower SRs than neurons

with high CFs for various species. Firing rates of MNTB neurons are related to GBCs, because they are directly driven by GBCs through calyxes of Held which work as relays (Borst and Soria van Hoeve 2012). However, the SRs of MNTB neurons were higher than SRs of GBCs.

Because the VS and EI (as well as driven rate) are a non-decreasing function of synaptic weights (Figure 3.4), the SR was the limiting factor during the parameter scan. The SR was set to 7.5 spikes/s which was the average SR of GBCs with CF <6 kHz from Spirou, Brownell, and Zidanic (1990). The optimal synaptic weights for various numbers of ANF inputs and levels of synaptic depression are shown in Figure 3.6. The plot shows that the weights decrease with increasing number of ANF inputs to the asymptote of 0. Additionally, synapses with stronger depression have larger synaptic weights. The weights in the plot represent the initial synaptic conductance which is reduced during synaptic operation.

Rothman, Young, and Manis (1993) presented a study of a bushy cell model with tonic synapses that was strongly influential for the design of the current model. The authors performed a detailed parameter space scan varying the number of inputs and synaptic strengths. Their model could reproduce all typical peristimulus time histograms of bushy cells (PL, PL_N, On) and improve synchronization. The main differences with the presented study were lower number of ANF inputs (1 to 20) and consideration of tonic synapses only. The model of Rothman, Young, and Manis (1993) most successfully captured the properties of spherical bushy cells, whereas the presented model focused on GBCs. Furthermore, Kuenzel, Nerlich, et al. (2015) and Nerlich et al. (2014) showed advancements in modeling of spherical bushy cells which included inhibition and dynamic synapses to better explain *in vitro* and *in vivo* experiments.

Spirou, Rager, and Manis (2005) presented a detailed biophysical model of GBCs. They combined structural data from electron microscopy with physiological data about vesicle release probability, synaptic depression, and receptor kinetics from Graham (2001). The model was tuned to closely reflect physiological data and successfully reproduced peristimulus time histograms of various GBCs. However, this model failed to improve the temporal precision for depressing synapses, with none of the simulated cells achieving a synchronization index larger than 0.9. In contrast, improved phase locking was one of the main goals of the presented model. Finally, various depression levels for phenomenological synapse models were also examined.

3.4.2 Levels of Depression in *in vivo*-like Simulations

Three different types of models of endbulb of Held are presented: tonic, with single, and with double exponential recovery synapse. Tonic synapses were reported in some earlier *in vivo* studies of endbulbs (Borst 2010; Young and Sachs 2008;

Kuenzel, Borst, and Heijden 2011) and calyxes (Lorteije et al. 2009) of Held. They also represent a boundary case when analyzing depression, because they are equivalent to 0%-depressing synapses. Simple depressing synapses with single exponential recovery allowed us to study a whole range of depression levels (0 % to 70 %). Finally, depressing synapse with double exponential recovery represented an average synapse from *in vitro* experiments, where the data was fitted to a double exponential function, see Figure 3.3 (Yang and Xu-Friedman 2009). All synapse models were purely phenomenological, i.e., they did not attempt to explain the mechanism of depression. It allowed us to easily manipulate synapse parameters and observe the influence of the depression on firing properties in *in vivo*-like stimulations.

A qualitative comparison of two synapses is shown in Figure 3.5. It shows synaptic currents of a weakly depressing (10%-depressing) and a strongly depressing (YXF09m, Table 3.1) synapse during spontaneous and driven activity. First, the responses during the spontaneous activity look very similar. This is a direct result of the optimization where all synapses were fitted to have a specific SR. Second, the average amplitude of the synaptic currents is smaller compared to the 10%-depressing synapse. The peaks often do not reach the threshold necessary to generate a single action potential. As a result, there are many failures in generating action potentials. The strong difference in the driven region between both synapses is expected, because they represent the two extreme cases: one of the least and one of the most depressing synapses in the study. The other depression levels are expected to lie between them and are shown next.

Figure 3.7 shows how different synapse types and levels of depression influence firing properties of GBCs in *in vivo*-like simulations. Interestingly, the depression level had little effect on phase locking. All GBC spike trains had VS greater than VS of ANF trains for frequencies <1 kHz, which is also observed *in vivo*. The results quantify how EI degrades with increasing synaptic depression. It is consistent with Figure 3.5 where the strongly depressing synapse was not able to drive GBCs to high firing rates. For the given number of ANF inputs (40), the maximum depression was approximately 50 % to 60 %. Stronger depression levels caused EI to be lower than the EI of the reference data. The interplay between the depression level and the number of ANF inputs is explained in the next paragraph.

Figure 3.9 shows fitting results of every depression model to individual EI data points in the transition region (CF <500 Hz) from Joris, Carney, et al. (1994). The allowed number of ANF inputs was in the range of 10 to 70 (Spirou, Rager, and Manis 2005). If no fit was found, the corresponding field was left blank. Additional results including GBCs with higher SRs (20 spikes/s and 50 spikes/s) are shown in the Supplementary Material. First of all, in the low frequency region (not shown in Figure 3.9, but visible in Figure 3.7) all data could be reproduced by all

examined synapses. It is consistent with *in vitro* observations of a large variability of the depressing synapses (Yang and Xu-Friedman 2009). However, the double exponential recovery synapse, that was tuned explicitly to *in vitro* data, did not reach the desired entrainment for GBCs with CFs >500 Hz, which could have two explanations:

1. The synaptic properties depend on the stimulus, e.g., a synapse might have different recovery time constants for paired-pulse (often used in slices) and ongoing (*in vivo*-like) stimuli as observed by Yang and Xu-Friedman (2015).

2. Physiological conditions *in vitro* and *in vivo* are responsible for different synaptic properties as suggested by Lorteije et al. (2009).

Therefore, for the *in vitro* synapse model to properly operate in *in vivo* conditions, requires either (a) adjustment of the synaptic parameters for the *in vivo* condition, or (b) a development of a more complex model (including the actual bio-physiological processes). This result also suggests that slice measurements of synaptic parameters cannot be easily adopted to *in vivo* conditions.

The finding above is consistent with many *in vivo* observations of calyx of Held, where there was a small depression observed (T. Wang, Rusu, et al. 2013; T. Wang, de Kok, et al. 2015; Di Guilmi et al. 2014) or no evidence of synaptic depression (Lorteije et al. 2009). Also, Kuenzel, Borst, and Heijden (2011) and Young and Sachs (2008) did not observe evidence of strong synaptic depression *in vivo* in endbulbs of Held. Hermann, Grothe, and Klug (2009) observed reduction (but not abolition) of the synaptic depression *in vitro* using conditioning with spontaneous activity. They concluded that calyxes of Held operate in chronic synaptic depression *in vivo*. A similar explanation came from Friauf, Fischer, and Fuhr (2015) where they proposed that *in vivo* synapses are in their normal stimulation range and the *in vitro* synapses are in a "manic" state due to lack of the spontaneous stimulation. Additionally, a possibly similar effect *in vivo* was shown by Di Guilmi et al. (2014) and T. Wang, de Kok, et al. (2015) where calyxes associated with LSR (<20 Hz) MNTB neurons had larger synaptic depression (23 %) than HSR neurons (8 %). The difference between *in vivo* and *in vitro* synapses could be also partially explained by adjusting the Ca^{2+} concentration. Yang and Xu-Friedman (2015) showed large changes in synaptic depression by varying Ca^{2+} concentration from 1 mmol l^{-1} to 2 mmol l^{-1} which resulted in depression varying from 0 % to >50 %. Lorteije et al. (2009) observed reduction of the synaptic depression *in vitro* when varying Ca^{2+} concentration. They also noted that deviations in Ca^{2+} concentration was not enough to explain the difference between *in vitro* and *in vivo* synapses. Additionally, Yang and Xu-Friedman (2015) showed that not only the depression levels, but also time constant are different between *in vitro* and *in vivo* synapses, which suggest a different mode of operation *in vitro* and *in vivo*.

3.4.3 Number of Auditory Nerve Fiber Inputs

In the simulations, the number of ANF inputs was varied from 10 to 70 similarly to the observations of Spirou, Rager, and Manis (2005). Figure 3.8 show that on the one hand, the number of ANF inputs did not significantly influence VS in pure tone stimulations. On the other hand, EI was strongly influenced by the number of ANF inputs. Figure 3.9 shows most EI data points can be reproduced by varying the number of ANF inputs for synapses with depression smaller than 50 %. In addition, Spirou, Rager, and Manis (2005) observed that the majority of GBC received less than 23 inputs, which could be reached only by some synapses in the transition region (CF >500 Hz) with low synaptic depression (0 % to 20 %).

Chapter 4

Summary

This thesis describes sound processing in the early states of the mammalian auditory system. It concentrates on two types of neurons in the auditory pathway (ANFs and GBCs) and a synaptic connection between them (endbulb of Held). Computational models of ANFs and GBCs are based on Hodgkin–Huxley-like channels and try to closely reflect empirical data. In most cases, the models were fitted to one set of experiments and verified by another experimental setup. This approach enhances the plausibility of the models and accuracy of their predictions.

Chapter 2 describes simulations of a multi-compartment ANF model. The same model was used both for synaptic and electrical stimulation. It was derived from two other models of Schwarz and Eikhof (1987) and Bade (2009). Schwarz and Eikhof (1987) provided the basis for the membrane ion channels. They were based on the temperature corrected Hodgkin–Huxley channels. They were used later to simulate ANFs by Mino et al. (2004) and Negm and Bruce (2008). The morphological structure of the model was derived from Bade (2009). It was however simplified by removing the soma and the dendrite. On the whole, the model was a straight cable of alternating nodes of Ranvier and myelinated internodes.

The main motivation behind the model was to verify, if a single relatively simple multi-compartment model can be used both for synaptic and electrical stimulation. In all experiments the structure and the parameters of the model were constant.

For the synaptic stimulation, a phenomenological synapse was attached to the terminal node. The synapse was carefully adjusted to *in vitro* experiments by Li et al. (2009). It was driven by a phenomenological model of a cochlea (Holmberg 2007), which provided *in vivo*-like input. Overall the hybrid cochlea–ANF model delivered realistic spike trains in most simulated experiments. The rates of the output spikes were correct for all tested frequencies. This result should however not be overrated, because the many properties came from the model of the cochlea and were correctly proxied by the ANF model. It is also an important result and means that the ANF model does not distort the rates when it is properly adjusted.

The temporal properties of the spike trains were worsened compared to the original inner ear model with a spike generator.

In all simulations of the electrical stimulation, all parameters of the ANF model were constant. Only the position of the electrode was adjusted depending on the experiment. In the initial experiments, the position of the electrode was based on the dimensions on the cochlea of a cat. Further experiments involved CIs in human subjects, so the position was adjusted accordingly. The results of the electrical simulations showed that the model can correctly reproduce stimulation thresholds for various pulse shapes of *in vivo*. The simulations showed that this property can be used inversely to find the optimal position of the electrode in the model based on the thresholds of various pulse shapes. The dynamic ranges of a single fibers in response to trains of pulses were correct. The maximum firing rate of 1000 Hz in the rate-level simulations is consistent with some ANFs. However, it seems to be too high for the majority of ANFs from the experiments Shepherd (1999). The model was also used to simulate psychoacoustic experiments with CI patients. Those simulations were based on the assumption that psychoacoustic thresholds could be directly compared with the firing thresholds in simulated ANFs. The results provided accurate relationship between thresholds for CAC and ACA pulses for the middle and the apical CI electrodes. On average, the patients were able to hear the difference in the loudness (close to the threshold) between ACA and CAC at the middle, but not at the apical electrodes. Quite remarkably, the model provided a possible anatomical explanation of the psychoacoustic results. It showed that this behavior could be explained by a segment with a large capacity in the neuron. Such discontinuity in the capacitance could come from a local demyelination of a degenerated ANF or from a demyelination soma in human spiral ganglion.

To sum up, this simple multi-compartment Hodgkin–Huxley model can successfully simulate both synaptic and electrical stimulation of ANFs. However, it has some limitations that could be addressed in the future versions:

1. High jitter in the synaptic stimulation.

2. High maximum firing rate in the electrical stimulation.

3. Adaptation of the firing rate, which are necessary when examining higher firing rates, especially in electrical stimulations (Negm and Bruce 2008; Woo, Miller, and Abbas 2009).

4. Improved morphological structure (e.g. inclusion of a soma) and detailed electrical field calculations could be beneficial for accuracy of cochlear implant stimulations (Rattay, Leao, and Felix 2001; Rattay, Lutter, and Felix 2001).

Chapter 3 focused on GBCs, which are located in the first auditory station in the central nervous system: cochlear nucleus. They receive inputs directly from

ANFs. GBCs are directly involved in sound localization and are characterized by primary-like PSTH responses with a notch after the initial onset, excellent phase-locking, and better entrainment than ANFs (Rhode 2008). Particularly interesting are large excitatory synapses located on their somas which are called endbulbs of Held. Depending on the experimental study, they show different short-term synaptic depression. On the one hand, *in vitro* studies usually show large depression (>50 %). On the other hand, most *in vivo* experiments show much smaller depression (10 % to 20 %). The model included realistic *in vivo*-like spike trains of an auditory nerve, endbulb of Held synapses, and a soma of a GBC with Hodgkin–Huxley-like specialized ion channels (Rothman and Manis 2003a; Rothman and Manis 2003b; Rothman and Manis 2003c).

The initial goal was to optimize the synaptic weights to reproduce excellent temporal properties of GBCs ("high-sync" neurons). The synapses were fitted for each combination of the depression level (0 % to 70 %) and the number of ANF inputs (10 to 70). Additionally, a synapse that was explicitly fitted to an average synapse from *in vitro* experiments was examined. The main objectives of the optimization were to maximize VS and EI while keeping the SR close to the relatively low empirical values. Keeping the SR relatively low was somewhat controversial. On the one hand, Spirou, Brownell, and Zidanic (1990) and Smith, Joris, and Yin (1993) showed that the majority of GBCs have low SR. On the other hand, there's an overall large variability in the SR and many GBCs have large SR (Rhode 2008) (also private conversations with J. G. G. Borst). As a result, the main focus of the chapter was set to GBCs with low SR. For reference, GBCs with high SR were also examined. Simulations of both low and high SR gave a full picture of the neuron population. Generally, it was possible to adjust synaptic weights for a wide range of depression levels and the number of inputs which is consistent with experimental observations (Joris, Carney, et al. 1994).

Interestingly, neither the depression level nor the number of ANF inputs (above certain value) had a strong impact on the synchronization (VS). However, the entrainment (EI) was strongly influenced by both. The effect of the depression level on the entrainment was shown qualitatively on two synapses with the same SR. The strongly depressing synapses became quickly too weak to drive the GBC and initiate APs. Simulation data showed gradual degradation in entrainment with increasing synaptic depression. Surprisingly, synapses that were fitted explicitly to the *in vitro* slice experiments, were not able to reach realistic entrainment during *in vivo*-like stimulation. Experimental evidence of the different synaptic properties *in vitro* and *in vivo* was also presented by Yang and Xu-Friedman (2015). This result could have two explanations. First, the synaptic properties depend on the stimulus being used, e.g., synapses recovers differently from ongoing *in vivo*-like stimuli than from paired-pulse stimuli often used *in vitro*. Second, different conditions

in vivo and *in vitro* make a significant impact on synaptic operation. Therefore, using an *in vitro* fitted synapse in *in vivo* conditions requires either adjustment of the synapse to the new conditions, or development of a more complex model with biophysical mechanisms. The results show that a synapse fitted to *in vitro* experiments cannot be easily adopted to *in vivo*-like simulations.

Finally, the parameter scan showed the interplay between the depression level and the number of ANF inputs. The increasing depression level requires increase in the number of ANF inputs to generate realistic entrainment. Even very high depression levels (50 % and more) could provide realistic entrainment given enough ANFs as input (35 and more). In fact, no single depression level could result in valid EIs for the whole range of the number of ANF inputs observed *in vivo* (9–69, Spirou, Rager, and Manis (2005)). It suggests that a variability of the depression level is necessary to cover the observed entrainment levels *in vivo*. The same was true for simulations of GBCs with higher SR. This result is consistent with observations of large variability of the depression levels and the number of ANF inputs in experiments (Yang and Xu-Friedman 2009; Spirou, Rager, and Manis 2005). However, taking into account that the majority of GBCs have approximately 20 inputs (Spirou, Rager, and Manis 2005), it is likely that the majority of synapses have rather low depression levels (10 % to 20 %). According to the simulations, higher depression levels would cause unrealistically low entrainment in those cells.

While this study gives an overview of how the synaptic parameters (synaptic depression, number of synapses) influence the *in vivo*-like stimulations, it does not suggest any mechanistic explanations of the phenomena. The next logical step is to use biophysical models (Bracciali et al. 2009; Graham 2001) and try to better explain discrepancy between *in vivo* and *in vitro* depression levels. Another unexplored possibility of improvement is inclusion of dendritic and inhibitory inputs. It would be beneficial, because not much is known about the contribution of the dendritic inputs to the firing properties of GBCs. The influence of the inhibitory inputs on GBCs is not well understood neither. However, it was examined experimentally in spherical bushy cells (SBCs) in the CN by Keine and Rübsamen 2015. Inhibition acted as gain control and increased temporal precision of the output in the SBCs.

Appendix A

Equations of the Spiral Ganglion Neuron

Each segment of the SG neuron was modeled with Hodgkin–Huxley-type equations from Schwarz and Eikhof (1987). The segments corresponding to the nodes of Ranvier contained sodium, potassium, and leak channels. The internodes contained only leak channels. The membrane current I of a node of Ranvier from Equation 2.1 can be expanded to

$$I(t) = C\frac{dV}{dt} + \bar{g}_{\mathrm{Na}} m^3 h (V - E_{\mathrm{Na}}) + \bar{g}_{\mathrm{K}} n^4 (V - E_{\mathrm{K}}) + g_{\mathrm{leak}} (V - E_{\mathrm{leak}}), \qquad \text{(A.1)}$$

where V is the voltage across the membrane, C is the capacity of the segment. E_{leak}, E_{K}, and E_{Na} are reversal potentials. g_{leak}, $\bar{g}_{\mathrm{Na}}$, and $\bar{g}_{\mathrm{K}}$ are peak conductances for leak, Na^+, and K^+ channels respectively. Finally, n, m, and h are the gating variables and are described by the following differential equations:

$$\frac{dn}{dt} = \alpha_n(V)(1 - n) - \beta_n(V)n \qquad \text{(A.2)}$$

$$\frac{dm}{dt} = \alpha_m(V)(1 - m) - \beta_m(V)m \qquad \text{(A.3)}$$

$$\frac{dh}{dt} = \alpha_h(V)(1 - h) - \beta_h(V)h, \qquad \text{(A.4)}$$

Parameter	Value
Length L	$1\,\mu m$
Axial resistivity R_a	$100\,\Omega\,cm$
Diameter d	$1.5\,\mu m$
Capacitance c_m	$0.9\,\mu F\,cm^{-2}$
Peak Na^+ channel conductance $\bar{g}_{Na}$	$0.3238\,S\,cm^{-2}$
Peak K^+ channel conductance $\bar{g}_K$	$0.1046\,S\,cm^{-2}$
Leakage conductance g_{leak}	$1 \times 10^{-5}\,S\,cm^{-2}$

Table A.1: SG neuron model parameters of the nodes of Ranvier.

The α and β functions were measured empirically (Hodgkin and Huxley 1952; Schwarz and Eikhof 1987) and are shown below:

$$\alpha_n(V) = \frac{0.02(35 - V)}{\exp(\frac{35-V}{10}) - 1} \tag{A.5}$$

$$\alpha_m(V) = \frac{0.49(25.41 - V)}{\exp(\frac{25.41-V}{6.06}) - 1} \tag{A.6}$$

$$\alpha_h(V) = \frac{0.09(27.74 + V)}{\exp(\frac{27.74+V}{9.06}) - 1} \tag{A.7}$$

$$\beta_n(V) = \frac{0.05(V - 10)}{\exp(\frac{V-10}{10}) - 1} \tag{A.8}$$

$$\beta_m(V) = \frac{1.04(V - 21)}{\exp(\frac{V-21}{9.41}) - 1} \tag{A.9}$$

$$\beta_h(V) = \frac{3.7}{1 + \exp(\frac{56-V}{12.5})}. \tag{A.10}$$

All α and β functions were scaled by the temperature coefficient Q_{10} of 2.9. The resting potential V_{rest} was $-78\,mV$.

The values of node of Ranvier parameters and internode parameters are shown in Tables A.1 and A.2 respectively.

The implementation of the SG neuron model is available online at (Rudnicki and Hemmert 2018–).

Parameter	Value
Length L	$250\,\mu m$
Axial resistivity R_a	$100\,\Omega\,cm$
Diameter d	$1.5\,\mu m$
Capacitance c_m	$1 \times 10^{-3}\,\mu F\,cm^{-2}$
Leakage conductance g_{leak}	$1 \times 10^{-5}\,S\,cm^{-2}$

Table A.2: SG neuron model parameters of the internodes.

Appendix B

Equations of the Globular Bushy Cell

The model of the GBC was a single compartment representing a soma with specialized Hodgkin–Huxley-type ion channels. The shape of the soma was a sphere with a diameter of 20 µm. The total membrane current I was equal to

$$I = C\frac{dV}{dt} + I_{\text{leak}} + I_{\text{Na}} + I_{\text{Kht}} + I_{\text{Klt}} + I_{\text{h}}, \tag{B.1}$$

where V is the voltage across the membrane, C is the capacitance of the membrane, I_{leak} is the leakage current, I_{Na} is the Na^+ current, I_{Klt} is the fast-activating slow-inactivating low-threshold K^+ current, I_{Kht} is the high-threshold K^+ current, and I_{h} is the hyperpolarization-activated cation current.

The leak current I_{leak} was equal to

$$I_{\text{leak}} = g_{\text{leak}}(V - E_{\text{leak}}), \tag{B.2}$$

where g_{leak} was the leak conductance and E_{leak} was the leakage equilibrium potential.

The Na^+ current I_{Na} was based on the paper from Spirou, Rager, and Manis (2005) and was equal to

$$I_{\text{Na}} = \bar{g}_{\text{Na}} m^3 h (V - E_{\text{Na}}), \tag{B.3}$$

where $\bar{g}_{\text{Na}}$ is the peak conductance of the Na^+ channels, m and h are the activation and inactivation gating variables, and E_{Na} is the reversal potential for Na^+. m and

h had the following voltage-dependent rate constants:

$$\alpha_m(V) = \frac{0.36(V+49)}{1-\exp\left(-\frac{V+49}{3}\right)} \tag{B.4}$$

$$\beta_m(V) = \frac{-0.4(V+58)}{1-\exp\left(\frac{V+58}{20}\right)} \tag{B.5}$$

$$\alpha_h(V) = \frac{2.4}{1+\exp(\frac{V+68}{3})} + \frac{0.8}{1+\exp(V+61.3)} \tag{B.6}$$

$$\beta_h(V) = \frac{3.6}{1+\exp\left(-\frac{V+21}{10}\right)}. \tag{B.7}$$

The high-threshold K^+ current I_{Kht} was based on Rothman and Manis (2003c) and equaled to

$$I_{\text{Kht}} = \bar{g}_{\text{Kht}}(0.85n^2 + 0.15p)(V - E_{\text{Kht}}), \tag{B.8}$$

where $\bar{g}_{\text{Kht}}$ was the peak conductance of the channels, n and p were the gating variables, and $\bar{E}_{\text{Kht}}$ was the reversal potential of I_{Kht}. The gating variables n and p were calculated from

$$\frac{dn}{dt} = \frac{(n_\infty - n)}{\tau_n} \quad \text{and} \quad \frac{dp}{dt} = \frac{(p_\infty - p)}{\tau_p}, \tag{B.9}$$

where

$$n_\infty = \frac{1}{\sqrt{1+\exp\left(-\frac{V+15}{5}\right)}} \tag{B.10}$$

$$p_\infty = \frac{1}{\sqrt{1+\exp\left(-\frac{V+23}{6}\right)}} \tag{B.11}$$

$$\tau_n = \frac{100}{11\exp\left(\frac{V+60}{24}\right) + 21\exp\left(-\frac{V+60}{23}\right)} + 0.7 \tag{B.12}$$

$$\tau_p = \frac{100}{4\exp\left(\frac{V+60}{32}\right) + 5\exp\left(-\frac{V+60}{22}\right)} + 5. \tag{B.13}$$

The low-threshold K^+ current I_{Klt} was based on Rothman and Manis (2003c) and was equal to

$$I_{\text{Klt}} = \bar{g}_{\text{Klt}} w^4 z (V - E_{\text{Klt}}), \tag{B.14}$$

where $\bar{g}_{\text{Klt}}$ was the peak conductance of the channels, w and z were the gating variables, and $\bar{E}_{\text{Klt}}$ was the reversal potential of I_{Klt}. The gating variables w and z were calculated from

$$\frac{dw}{dt} = \frac{(w_\infty - w)}{\tau_w} \quad \text{and} \quad \frac{dz}{dt} = \frac{(z_\infty - z)}{\tau_z}, \tag{B.15}$$

where

$$w_\infty = \frac{1}{\sqrt[4]{1+\exp\left(-\frac{V+48}{6}\right)}} \tag{B.16}$$

$$z_\infty = \frac{0.5}{1+\exp\left(\frac{V+71}{10}\right)} + 0.5 \tag{B.17}$$

$$\tau_w = \frac{100}{6\exp\left(\frac{V+60}{6}\right) + 16\exp\left(-\frac{V+60}{45}\right)} + 1.5 \tag{B.18}$$

$$\tau_z = \frac{1000}{\exp\left(\frac{V+60}{20}\right) + \exp\left(-\frac{V+60}{8}\right)} + 50. \tag{B.19}$$

The hyperpolarization-activated cation current I_h was based on Rothman and Manis (2003c) and was equal to

$$I_\mathrm{h} = \bar{g}_\mathrm{h} r (V - E_\mathrm{h}), \tag{B.20}$$

where $\bar{g}_\mathrm{h}$ was the peak conductance of the channels, r was the gating variable, and E_h was the reversal potential of I_h. The gating variables w and z were calculated from

$$\frac{dr}{dt} = \frac{(r_\infty - r)}{\tau_r} \tag{B.21}$$

where

$$r_\infty = \frac{1}{1+\exp\left(\frac{V+76}{7}\right)} \tag{B.22}$$

$$\tau_r = \frac{100000}{237\exp\left(\frac{V+60}{12}\right) + 17\exp\left(-\frac{V+60}{14}\right)} + 25. \tag{B.23}$$

All model parameters are summarized in Table B.1. Most of the parameters were derived from the model Type II of Rothman and Manis (2003c). The ceNa+ channels were taken from Spirou, Rager, and Manis (2005).

The implementation of the GBC neuron model is available online at (Rudnicki and Hemmert 2017–).

Parameter	Value
Diameter (L & d)	20 µm
Capacitance c_m	0.9 µF cm^{-2}
Peak Na^+ channel conductance $\bar{g}_{Na}$	2500 nS
Peak high-threshold K^+ channel conductance $\bar{g}_{Kht}$	150 nS
Peak low-threshold K^+ channel conductance $\bar{g}_{Klt}$	200 nS
Peak hyperpolarization-activated cation channel conductance $\bar{g}_h$	20 nS
Leakage conductance g_{leak}	2 nS
Q_{10} of Na^+ channels	2.5
Q_{10} of other channels	1.5

Table B.1: Parameters of the GBC model.

Appendix C

Software Repositories

The source code of the models and libraries written for the purpose of the thesis is available online in git repositories. The software is released under the GNU General Public License v3 and available on GitHub.

- `https://github.com/mrkrd/cochlea` contains the source code of the inner ear models including Holmberg (2007) and M. S. A. Zilany, Bruce, and Carney (2014). All models take an array representing sound as input and return spike trains or synaptic vesicle events as output. They were used in both main Chapters (2 and 3) of the thesis.

- `https://github.com/mrkrd/spiral_ganglion` implements a multicompartment Hodgkin–Huxley-type model of an ANF. It contains a phenomenological model of an IHC synapse that can be combined with an inner ear model. It also contains a model of an electrode and conducting medium that can be used to electrically stimulate the ANF. The model takes the IHC synaptic vesicle events or electrical potential as input, and returns membrane voltages or spike trains as output. It was used in Chapter 2.

- `https://github.com/mrkrd/cochlear_nucleus` implements a Hodgkin–Huxley-type model of a GBC. It also contains various phenomenological models of endbulb of Held synapses. The model takes ANF spike trains as input and returns GBC spike trains as output. It was used in Chapter 3.

- `https://github.com/mrkrd/thorns` is an auxiliary library that contains functions to analyze and visualize spike trains. It also implements routines that help to parallelize computations and cache the results.

List of Figures

List of Tables

Bibliography

Bade, P. W. (2009). "Modelling of Auditory Nerve Fibers in the Simulation Environment NEURON". MA thesis. Technische Universität München.

Bai, S., J. Encke, R. Weiss, K. Achterhold, F. Boehnke, K. Braun, and W. Hemmert (2017). "Reconstruction of a high-resolution cochlear model for cochlear implant research". In: *2017 Conference on Implantable Auditory Prostheses*.

Bear, M. F., B. W. Connors, and M. A. Paradiso (2007). *Neuroscience: exploring the brain*. Third. Lippincott Williams & Wilkins.

Borst, J. G. G. (2010). "The low synaptic release probability in vivo". In: *Trends in neurosciences* 33.6, pp. 259–266. ISSN: 1878-108X. DOI: 10.1016/j.tins.2010.03.003.

Borst, J. G. G. and J. Soria van Hoeve (2012). "The calyx of Held synapse: from model synapse to auditory relay." In: *Annual review of physiology* 74, pp. 199–224. ISSN: 1545-1585. DOI: 10.1146/annurev-physiol-020911-153236.

Bracciali, A., M. Brunelli, E. Cataldo, and P. Degano (2009). "Formal Models of the Calyx of Held". In: *Algorithmic Bioprocesses*. Springer Science+Business Media, pp. 331–366. DOI: 10.1007/978-3-540-88869-7_18.

Briaire, J. J. and J. H. Frijns (2000). "Field patterns in a 3D tapered spiral model of the electrically stimulated cochlea". In: *Hearing research* 148.1, pp. 18–30.

Bruce, I. C., Y. Erfani, and M. S. Zilany (2018). "A phenomenological model of the synapse between the inner hair cell and auditory nerve: Implications of limited neurotransmitter release sites". In: *Hearing Research* 360, pp. 40–54. DOI: 10.1016/j.heares.2017.12.016.

Burden, R. L. and J. D. Faires (1985). "Numerical Analysis". In: PWS Publishers. Chap. 2.1 The Bisection Algorithm.

Cao, X.-J. and D. Oertel (2010). "Auditory Nerve Fibers Excite Targets Through Synapses That Vary in Convergence, Strength, and Short-Term Plasticity". In: *Journal of Neurophysiology* 104.5, pp. 2308–2320. DOI: 10.1152/jn.00451.2010.

Carnevale, N. T. and M. L. Hines (2006). *The NEURON Book*. Cambridge, UK: Cambridge University Press. ISBN: 0521843219. DOI: 10.1017/cbo9780511541612.

Cook, D. L., P. C. Schwindt, L. A. Grande, and W. J. Spain (2003). "Synaptic depression in the localization of sound". In: *Nature* 421.6918, pp. 66–70. ISSN: 0028-0836. DOI: 10.1038/nature01248.

Dayan, P. and L. F. Abbott (2005). *Theoretical Neuroscience: Computational and Mathematical Modeling of Neural Systems*. Ed. by T. J. Sejnowski and T. Poggio. MIT PR. 480 pp. ISBN: 0262541858.

Di Guilmi, M. N., T. Wang, C. G. Inchauspe, I. D. Forsythe, M. D. Ferrari, A. M. J. M. van den Maagdenberg, J. G. G. Borst, and O. D. Uchitel (2014). "Synaptic gain-of-function effects of mutant Cav2.1 channels in a mouse model of familial hemiplegic migraine are due to increased basal [Ca2+]i." eng. In: *J. Neurosci.* 34.21, pp. 7047–7058. DOI: 10.1523/JNEUROSCI.2526-13.2014.

Dillon, H. (2001). *Hearing Aids*. Thieme. ISBN: 1-58890-052-5.

Drachman, D. A. (2005). "Do we have brain to spare?" In: *Neurology* 64 (12), pp. 2004–2005. ISSN: 1526-632X. DOI: 10.1212/01.WNL.0000166914.38327.BB.

Durand, D. M. (2000). "Electric Stimulation of Excitable Tissue". In: *Biomedical Engineering Handbook*. Ed. by J. D. Bronzino. 2 Sub. CRC Press LLC. ISBN: 084930461X.

Encke, J., S. Bai, N. Baehr, and W. Hemmert (2017). "A biophysical model of the auditory nerve based on high-resolution microct scans". In: *2017 Conference on Implantable Auditory Prostheses*.

Encke, J. and W. Hemmert (2015). "The Relative Timing of Inhibitory and Excitatory Currents Tunes the Shift of Best ITD in a Detailed Mammalian MSO Network Model." In: *The Auditory Model Workshop*. Oldenburg, Germany.

Encke, J. and W. Hemmert (2018). "Extraction of Inter-Aural Time Differences Using a Spiking Neuron Network Model of the Medial Superior Olive". In: *Frontiers in Neuroscience* 12, pp. 1–12. DOI: 10.3389/fnins.2018.00140.

Finley, C. C. et al. (1988). "Comparative studies of speech processing strategies for cochlear implants". In: *The Laryngoscope* 98.10, p. 10691077. DOI: 10.1288/00005537-198810000-00009.

Frank, G., W. Hemmert, and A. W. Gummer (1999). "Limiting dynamics of high-frequency electromechanical transduction of outer hair cells". In: *Proceedings of the National Academy of Sciences* 96.8, pp. 4420–4425. ISSN: 0027-8424. DOI: 10.1073/pnas.96.8.4420.

Friauf, E., A. U. Fischer, and M. F. Fuhr (2015). "Synaptic plasticity in the auditory system: a review." eng. In: *Cell Tissue Res* 361.1, pp. 177–213. DOI: 10.1007/s00441-015-2176-x.

Xu-Friedman, M. A. and W. G. Regehr (2005). "Dynamic-Clamp Analysis of the Effects of Convergence on Spike Timing. I. Many Synaptic Inputs". In: *J Neurophysiol* 94.4, pp. 2512–2525. ISSN: 0022-3077. DOI: 10.1152/jn.01307.2004.

Frijns, J., S. de Snoo, and J. ten Kate (1996). "Spatial selectivity in a rotationally symmetric model of the electrically stimulated cochlea". In: *Hearing Research* 95.1–2, pp. 33–48. ISSN: 0378-5955. DOI: 10.1016/0378-5955(96)00004-4.

Geddes, L. A. and L. E. Baker (1967). "The specific resistance of biological material–a compendium of data for the biomedical engineer and physiologist." eng. In: *Med Biol Eng* 5.3, pp. 271–293.

Geisler, C. D., L. Deng, and S. R. Greenberg (1985). "Thresholds for primary auditory fibers using statistically defined criteria." In: *The Journal of the Acoustical Society of America* 77.3, pp. 1102–1109. ISSN: 0001-4966.

Gelfand, S. A. (2010). *Hearing: An Introduction to Psychological and Physiological Acoustics*. Informa Healthcare. ISBN: 978-1-4200-8865-6.

Gerstner, W. and W. M. Kistler (2002). *Spiking Neuron Models*. Cambridge University Press (CUP). DOI: 10.1017/cbo9780511815706.

Gifford, R. H., J. K. Shallop, and A. M. Peterson (2008). "Speech Recognition Materials and Ceiling Effects: Considerations for Cochlear Implant Programs". In: *Audiology and Neurotology* 13.3, pp. 193–205. DOI: 10.1159/000113510.

Goldwyn, J. H., N. S. Imennov, M. Famulare, and E. Shea-Brown (2011). "Stochastic differential equation models for ion channel noise in Hodgkin-Huxley neurons". In: *Physical Review E* 83.4, pp. 1–16. DOI: 10.1103/physreve.83.041908.

Graham, B. (2001). "A computational model of synaptic transmission at the calyx of Held". In: *Neurocomputing* 38-40.1-4, pp. 37–42. ISSN: 09252312. DOI: 10.1016/S0925-2312(01)00476-3.

Gray, H. (1918). *Anatomy of the human body*. Lea & Febiger.

Grothe, B., M. Pecka, and D. McAlpine (2010). "Mechanisms of Sound Localization in Mammals". In: *Physiological Reviews* 90.3, pp. 983–1012. ISSN: 1522-1210. DOI: 10.1152/physrev.00026.2009.

Hatsushika, S., R. K. Shepherd, Y. C. Tong, G. M. Clark, and S. Funasaka (1990). "Dimensions of the scala tympani in the human and cat with reference to cochlear implants." eng. In: *Ann Otol Rhinol Laryngol* 99.11, pp. 871–876. DOI: 10.1177/000348949009901104.

Heil, P. and A. J. Peterson (2015). "Basic response properties of auditory nerve fibers: a review." eng. In: *Cell Tissue Res.* DOI: 10.1007/s00441-015-2177-9.

Hermann, J., B. Grothe, and A. Klug (2009). "Modeling Short-Term Synaptic Plasticity at the Calyx of Held Using In Vivo-Like Stimulation Patterns". In: *J Neurophysiol* 101.1, pp. 20–30. DOI: 10.1152/jn.90243.2008.

Hertzano, R. et al. (2008). "A Myo6 mutation destroys coordination between the myosin heads, revealing new functions of myosin VI in the stereocilia of mammalian inner ear hair cells." In: *PLoS genetics* 4 (10), e1000207. ISSN: 1553-7404. DOI: 10.1371/journal.pgen.1000207.

Hodgkin, A. L. and A. F. Huxley (1952). "A quantitative description of membrane current and its application to conduction and excitation in nerve." In: *The Journal of physiology* 117.4, pp. 500–544. ISSN: 0022-3751.

Holmberg, M. (2007). "Speech Encoding in the Human Auditory Periphery: Modeling and Quantitative Assessment by Means of Automatic Speech Recognition". PhD thesis. Technical University Darmstadt.

Hossain, W. A., S. D. Antic, Y. Yang, M. N. Rasband, and D. K. Morest (2005). "Where is the spike generator of the cochlear nerve? Voltage-gated sodium channels in the mouse cochlea." eng. In: *J Neurosci* 25.29, pp. 6857–6868. DOI: 10.1523/JNEUROSCI.0123-05.2005.

Howell, W. H. (1911). *A text-book of physiology for medical students and physicians*. Philadelphia, London, W.B. Saunders company.

Ilberg, C. A. von, U. Baumann, J. Kiefer, J. Tillein, and O. F. Adunka (2011). "Electric-acoustic stimulation of the auditory system: a review of the first decade." eng. In: *Audiol Neurootol* 16 Suppl 2, pp. 1–30. DOI: 10.1159/000327765.

Jesteadt, W. (1980). "An adaptive procedure for subjective judgments." eng. In: *Percept. Psychophys.* 28.1, pp. 85–88. DOI: 10.3758/bf03204321.

Johnson, D. H. (1980). "The relationship between spike rate and synchrony in responses of auditory-nerve fibers to single tones." In: *The Journal of the Acoustical Society of America* 68.4, pp. 1115–1122. ISSN: 0001-4966.

Jones, E., T. Oliphant, P. Peterson, et al. (2001–). *SciPy: Open source scientific tools for Python*.

Joris, P. X., L. H. Carney, P. H. Smith, and T. C. Yin (1994). "Enhancement of neural synchronization in the anteroventral cochlear nucleus. I. Responses to tones at the characteristic frequency." In: *Journal of neurophysiology* 71.3, pp. 1022–1036. ISSN: 0022-3077.

Joris, P. X. and P. H. Smith (2008). "The volley theory and the spherical cell puzzle." In: *Neuroscience* 154.1, pp. 65–76. ISSN: 0306-4522. DOI: 10.1016/j.neuroscience.2008.03.002.

Joris, P. X. and T. C. T. Yin (1992). "Responses to amplitude-modulated tones in the auditory nerve of the cat". In: *The Journal of the Acoustical Society of America* 91.1, pp. 215–232.

Karg, S. A., M. Rudnicki, C. Lackner, and W. Hemmert (2013). "Effect of pulse polarity in biphasic and triphasic pulses". In: *2013 Conference on Implantable Auditory Prostheses*.

Keine, C. and R. Rübsamen (2015). "Inhibition shapes acoustic responsiveness in spherical bushy cells." eng. In: *J Neurosci* 35.22, pp. 8579–8592. DOI: 10.1523/JNEUROSCI.0133-15.2015.

Kiang, N. Y. (1965). *Discharge Patterns of Single Fibers in the Cat's Auditory Nerve*. Tech. rep. Massachusetts Inst of Tech Cambridge Research Lab of Electronics. DOI: 10.1037/008081.

Kiefer, J., S. Hohl, E. Stürzebecher, T. Pfennigdorff, and W. Gstöettner (2001). "Comparison of Speech Recognition with Different Speech Coding Strategies (SPEAK, CIS, and ACE) and Their Relationship to Telemetric Measures of Compound Action Potentials in the Nucleus CI 24M Cochlear Implant System:Comparación del reconocimiento del lenguaje utilizando diferentes estrategias (SPEAK, CIS y ACE) y su relación con mediciones telemétricas de potenciales de acción compuestos, con el sistema de implante coclear nucleus CI24M". In: *International Journal of Audiology* 40.1, pp. 32–42. DOI: 10.3109/00206090109073098.

Kopp-Scheinpflug, C., S. Tolnai, M. Malmierca, and R. Rübsamen (2008). "The medial nucleus of the trapezoid body: comparative physiology." eng. In: *Neuroscience* 154.1, pp. 160–170. DOI: 10.1016/j.neuroscience.2008.01.088.

Kral, A. (1998). "Spatial resolution of cochlear implants: the electrical field and excitation of auditory afferents". In: *Hearing Research* 121.1-2, pp. 11–28. ISSN: 03785955. DOI: 10.1016/S0378-5955(98)00061-6.

Kuenzel, T., J. G. G. Borst, and M. van der Heijden (2011). "Factors controlling the input-output relationship of spherical bushy cells in the gerbil cochlear nucleus." In: *The Journal of neuroscience : the official journal of the Society for Neuroscience* 31.11, pp. 4260–4273. ISSN: 1529-2401. DOI: 10.1523/JNEUROSCI.5433-10.2011.

Kuenzel, T., J. Nerlich, H. Wagner, R. Rübsamen, and I. Milenkovic (2015). "Inhibitory properties underlying non-monotonic input-output relationship in low-frequency spherical bushy neurons of the gerbil." eng. In: *Front Neural Circuits* 9, p. 14. DOI: 10.3389/fncir.2015.00014.

Li, G., E. Keen, D. Andor-Ardo, A. J. Hudspeth, and H. von Gersdorff (2009). "The Unitary Event Underlying Multiquantal EPSCs at a Hair Cell's Ribbon Synapse". In: *Journal of Neuroscience* 29.23, pp. 7558–7568. ISSN: 1529-2401. DOI: 10.1523/JNEUROSCI.0514-09.2009.

Liberman, M. C. (1991). "Central projections of auditory-nerve fibers of differing spontaneous rate. I. Anteroventral cochlear nucleus". In: *The Journal of Comparative Neurology* 313.2, pp. 240–258. ISSN: 1096-9861. DOI: 10.1002/cne.903130205.

Lorteije, J. A. M., S. I. Rusu, C. Kushmerick, and J. G. G. Borst (2009). "Reliability and Precision of the Mouse Calyx of Held Synapse". In: *Journal of Neuroscience* 29.44, pp. 13770–13784. ISSN: 1529-2401. DOI: 10.1523/JNEUROSCI.3285-09.2009.

Magnusson, L. (2010). "Comparison of the fine structure processing (FSP) strategy and the CIS strategy used in the MED-EL cochlear implant system: Speech intelligibility and music sound quality". In: *International Journal of Audiology* 50.4, pp. 279–287. DOI: 10.3109/14992027.2010.537378.

Malmivuo, J. and R. Plonsey (1995). "Bioelectromagnetism - Principles and Applications of Bioelectric and Biomagnetic Fields". In: Oxford University Press. Chap. Source-Field Models.

Markram, H. (2006). "The Blue Brain Project". In: *Nature Reviews Neuroscience* 7.2, pp. 153–160. DOI: 10.1038/nrn1848.

Mino, H., J. T. Rubinstein, C. A. Miller, and P. J. Abbas (2004). "Effects of Electrode-to-Fiber Distance on Temporal Neural Response With Electrical Stimulation". In: *IEEE Transactions on Biomedical Engineering* 51.1, pp. 13–20. ISSN: 0018-9294. DOI: 10.1109/TBME.2003.820383.

Negm, M. H. and I. C. Bruce (2008). "Effects of Ih and IKLT on the response of the auditory nerve to electrical stimulation in a stochastic Hodgkin-Huxley model". In: *2008 30th Annual International Conference of the IEEE Engineering in Medicine and Biology Society*. Vancouver, BC: IEEE, pp. 5539–5542. ISBN: 978-1-4244-1814-5. DOI: 10.1109/IEMBS.2008.4650469.

Negm, M. H. and I. C. Bruce (2014). "The Effects of HCN and KLT Ion Channels on Adaptation and Refractoriness in a Stochastic Auditory Nerve Model". In: *IEEE Transactions on Biomedical Engineering* 61.11, pp. 2749–2759. DOI: 10.1109/tbme.2014.2327055.

Nelson, M. and J. Rinzel (2003). "The Hodgkin-Huxley Model". In: *The Book of GENESIS*. Ed. by J. M. Bower and D. Beeman. Internet Edition. Chap. 4, pp. 29–50.

Nerlich, J., T. Kuenzel, C. Keine, A. Korenic, R. Rübsamen, and I. Milenkovic (2014). "Dynamic fidelity control to the central auditory system: synergistic glycine/GABAergic inhibition in the cochlear nucleus." eng. In: *J Neurosci* 34.35, pp. 11604–11620. DOI: 10.1523/JNEUROSCI.0719-14.2014.

NIH Consens Statement (1995). *Cochlear Implants in Adults and Children*. Tech. rep. 2. National Institutes of Health.

O'Brien, G. E. and J. T. Rubinstein (2016). "The development of biophysical models of the electrically stimulated auditory nerve: Single-node and cable models." In: *Network (Bristol, England)* 27 (2-3), pp. 135–156. ISSN: 1361-6536. DOI: 10.3109/0954898X.2016.1162338.

Oleskevich, S., J. Clements, and B. Walmsley (2000). "Release probability modulates short-term plasticity at a rat giant terminal". In: *The Journal of Physiology* 524.2, pp. 513–523. ISSN: 0022-3751. DOI: 10.1111/j.1469-7793.2000.00513.x.

Oliphant, T. E. (2007). "Python for Scientific Computing". In: *Computing in Science & Engineering* 9.3, pp. 10–20. DOI: 10.1109/mcse.2007.58.

Osen, K. K. (1969). "Cytoarchitecture of the cochlear nuclei in the cat". In: *The Journal of Comparative Neurology* 136.4, pp. 453–483. ISSN: 1096-9861. DOI: 10.1002/cne.901360407.

Palmer, A. R. and I. Russell (1986). "Phase-locking in the cochlear nerve of the guinea-pig and its relation to the receptor potential of inner hair-cells". In: *Hearing Research* 24.1, pp. 1–15. ISSN: 0378-5955. DOI: 10.1016/0378-5955(86)90002-X.

Peterson, A. J. and P. Heil (2017). "A simple model of the inner-hair-cell ribbon synapse accounts for mammalian auditory-nerve-fiber spontaneous spike times". In: *Hearing Research*, pp. 1–27. DOI: 10.1016/j.heares.2017.09.005.

Popper, A. N. and R. R. Fay, eds. (1992). *The Mammalian Auditory Pathway: Neurophysiology*. Springer New York. DOI: 10.1007/978-1-4612-2838-7.

Postlethwaite, M., M. H. Hennig, J. R. Steinert, B. P. Graham, and I. D. Forsythe (2007). "Acceleration of AMPA receptor kinetics underlies temperature-dependent changes in synaptic strength at the rat calyx of Held." In: *The Journal of physiology* 579.Pt 1, pp. 69–84. ISSN: 0022-3751. DOI: 10.1113/jphysiol.2006.123612.

Ranck Jr, J. (1975). "Which elements are excited in electrical stimulation of mammalian central nervous system: a review." eng. In: *Brain Res* 98.3, pp. 417–440. DOI: 10.1016/0006-8993(75)90364-9.

Rattay, F., R. N. Leao, and H. Felix (2001). "A model of the electrically excited human cochlear neuron. II. Influence of the three-dimensional cochlear structure on neural excitability". In: *Hearing Research* 153.1-2, pp. 64–79. ISSN: 0378-5955. DOI: 10.1016/S0378-5955(00)00257-4.

Rattay, F., P. Lutter, and H. Felix (2001). "A model of the electrically excited human cochlear neuron: I. Contribution of neural substructures to the generation and propagation of spikes". In: *Hearing Research* 153.1-2, pp. 43–63. ISSN: 0378-5955. DOI: 10.1016/S0378-5955(00)00256-2.

Recio, A. (2000). "Representation of vowel stimuli in the ventral cochlear nucleus of the chinchilla". In: *Hearing Research* 146.1-2, pp. 167–184. ISSN: 03785955. DOI: 10.1016/S0378-5955(00)00111-8.

Rhode, W. S. (2008). "Response patterns to sound associated with labeled globular/bushy cells in cat". In: *Neuroscience* 154.1, pp. 87–98. ISSN: 03064522. DOI: 10.1016/j.neuroscience.2008.03.013.

Rhode, W. S. and S. Greenberg (1994). "Encoding of amplitude modulation in the cochlear nucleus of the cat". In: *Journal of Neurophysiology* 71.5, pp. 1797–1825.

Rhode, W. S., D. Oertel, and P. H. Smith (1983). "Physiological response properties of cells labeled intracellularly with horseradish peroxidase in cat ventral cochlear nucleus". In: *The Journal of Comparative Neurology* 213.4, pp. 448–463. ISSN: 1096-9861. DOI: 10.1002/cne.902130408.

Rieke, F., D. Warland, R. de Ruyter van Steveninck, and W. Bialek (1999). *Spikes: exploring the neural code*. Cambridge, MA, USA: MIT Press. ISBN: 0-262-18174-6.

Robles, L. and M. A. Ruggero (2001). "Mechanics of the mammalian cochlea." In: *Physiological reviews* 81 (3), pp. 1305–1352. ISSN: 0031-9333.

Rothman, J. S., E. D. Young, and P. B. Manis (1993). "Convergence of auditory nerve fibers onto bushy cells in the ventral cochlear nucleus: implications of a computational model". In: *J Neurophysiol* 70.6, pp. 2562–2583. ISSN: 0022-3077.

Rothman, J. S. and P. B. Manis (2003a). "Differential Expression of Three Distinct Potassium Currents in the Ventral Cochlear Nucleus". In: *J Neurophysiol* 89.6, pp. 3070–3082. ISSN: 0022-3077. DOI: 10.1152/jn.00125.2002.

Rothman, J. S. and P. B. Manis (2003b). "Kinetic Analyses of Three Distinct Potassium Conductances in Ventral Cochlear Nucleus Neurons". In: *J Neurophysiol* 89.6, pp. 3083–3096. DOI: 10.1152/jn.00126.2002.

Rothman, J. S. and P. B. Manis (2003c). "The Roles Potassium Currents Play in Regulating the Electrical Activity of Ventral Cochlear Nucleus Neurons". In: *J Neurophysiol* 89.6, pp. 3097–3113. ISSN: 0022-3077. DOI: 10.1152/jn.00127.2002.

Rubinstein, J. (1993). "Axon termination conditions for electrical stimulation". In: *IEEE Transactions on Biomedical Engineering* 40.7, pp. 654–663. DOI: 10.1109/10.237695.

Rudnicki, M. and W. Hemmert (2009–). *cochlea: Inner Ear Models in Python*. https://github.com/mrkrd/cochlea.

Rudnicki, M. and W. Hemmert (2017). "High Entrainment Constrains Synaptic Depression Levels of an In vivo Globular Bushy Cell Model". In: *Frontiers in Computational Neuroscience* 11, pp. 1–11. DOI: 10.3389/fncom.2017.00016.

Rudnicki, M. and W. Hemmert (2017–). *cochlear_nucleus: Computational Models of Globular Bushy Cells in the Ventral Cochlear Nucleus*. https://github.com/mrkrd/cochlear_nucleus.

Rudnicki, M. and W. Hemmert (2018–). *spiral_ganglion: Computational Models of an Auditory Nerve Fiber*. https://github.com/mrkrd/spiral_ganglion.

Rudnicki, M., O. Schoppe, M. Isik, F. Völk, and W. Hemmert (2015). "Modeling auditory coding: from sound to spikes". In: *Cell and Tissue Research* 361.1, pp. 159–175. DOI: 10.1007/s00441-015-2202-z.

Rutherford, M. A. and T. Moser (2015). "The Ribbon Synapse Between Type I Spiral Ganglion Neurons and Inner Hair Cells". In: *The Primary Auditory Neurons of the Mammalian Cochlea*. Springer Nature, pp. 117–156. DOI: 10.1007/978-1-4939-3031-9_5.

Schwarz, J. R. and G. Eikhof (1987). "Na currents and action potentials in rat myelinated nerve fibres at 20 and 37 °C". In: *Pflügers Archiv* 409 (6), pp. 569–577. ISSN: 0031-6768. DOI: 10.1007/BF00584655.

Shepherd, R. K. (1999). "Electrical stimulation of the auditory nerve: II. Effect of stimulus waveshape on single fibre response properties". In: *Hearing Research* 130.1-2, pp. 171–188. ISSN: 03785955. DOI: 10.1016/S0378-5955(99)00011-8.

Shepherd, R. K. and E. Javel (1997). "Electrical stimulation of the auditory nerve. I. Correlation of physiological responses with cochlear status". In: *Hearing Research* 108.1-2, pp. 112–144. ISSN: 03785955. DOI: 10.1016/S0378-5955(97)00046-4.

Skinner, M. W. et al. (1994). "Evaluation of a new spectral peak coding strategy for the Nucleus 22 Channel Cochlear Implant System." In: *The American journal of otology* 15 Suppl 2, pp. 15–27. ISSN: 0192-9763.

Smith, P. H., P. X. Joris, and T. C. T. Yin (1993). "Projections of physiologically characterized spherical bushy cell axons from the cochlear nucleus of the cat: Evidence for delay lines to the medial superior olive". In: *The Journal of Comparative Neurology* 331.2, pp. 245–260. ISSN: 1096-9861. DOI: 10.1002/cne.903310208.

Smith, P. H. and G. A. Spirou (2002). "From the Cochlea to the Cortex and Back". In: *Integrative Functions in the Mammalian Auditory Pathway*. Springer Nature, pp. 6–71. DOI: 10.1007/978-1-4757-3654-0_2.

Spirou, G. A., W. E. Brownell, and M. Zidanic (1990). "Recordings from cat trapezoid body and HRP labeling of globular bushy cell axons". In: *J Neurophysiol* 63.5, pp. 1169–1190.

Spirou, G. A., J. Rager, and P. B. Manis (2005). "Convergence of auditory-nerve fiber projections onto globular bushy cells". In: *Neuroscience* 136.3, pp. 843–863. ISSN: 0306-4522. DOI: 10.1016/j.neuroscience.2005.08.068.

Sumner, C. J., E. A. Lopez-Poveda, L. P. O'Mard, and R. Meddis (2003). "Adaptation in a revised inner-hair cell model". In: *Acoustical Society of America Journal* 113, pp. 893–901. DOI: 10.1121/1.1515777.

Sumner, C. J., E. A. Lopez-Poveda, L. P. O'Mard, and R. Meddis (2002). "A revised model of the inner-hair cell and auditory-nerve complex". In: *The Journal of the Acoustical Society of America* 111.5, pp. 2178–2188.

Taschenberger, H., A. Woehler, and E. Neher (2016). "Superpriming of synaptic vesicles as a common basis for intersynapse variability and modulation of synaptic strength." In: *Proceedings of the National Academy of Sciences of the United States of America* 113 (31), E4548–E4557. ISSN: 1091-6490. DOI: 10.1073/pnas.1606383113.

Tsodyks, M. V. and H. Markram (1997). "The neural code between neocortical pyramidal neurons depends on neurotransmitter release probability". In: *Proceedings of the National Academy of Sciences* 94.2, pp. 719–723. ISSN: 0027-8424. DOI: 10.1073/pnas.94.2.719.

van 't Hoff, J. H. (1898). *Lectures on Theoretical and Physical Chemistry*. Vol. 1. Edward Arnold.

Wang, T., L. de Kok, R. Willemsen, Y. Elgersma, and J. G. G. Borst (2015). "In vivo synaptic transmission and morphology in mouse models of Tuberous sclerosis, Fragile X syndrome, Neurofibromatosis type 1, and Costello syndrome." eng. In: *Front Cell Neurosci* 9, p. 234. DOI: 10.3389/fncel.2015.00234.

Wang, T., S. I. Rusu, B. Hruskova, R. Turecek, and J. G. G. Borst (2013). "Modulation of synaptic depression of the calyx of Held synapse by GABAB receptors and spontaneous activity". In: *The Journal of Physiology* 591.19, pp. 4877–4894. DOI: 10.1113/jphysiol.2013.256875.

Wang, Y. and P. B. Manis (2008). "Short-Term Synaptic Depression and Recovery at the Mature Mammalian Endbulb of Held Synapse in Mice". In: *J Neurophysiol* 100.3, pp. 1255–1264. DOI: 10.1152/jn.90715.2008.

Webster, D. B., A. N. Popper, and R. R. Fay, eds. (1992). *The Mammalian Auditory Pathway: Neuroanatomy*. Springer New York. DOI: 10.1007/978-1-4612-4416-5.

Wiener, F. M. and D. A. Ross (1946). "The Pressure Distribution in the Auditory Canal in a Progressive Sound Field". In: *Journal of the Acoustical Society of America* 18.2, pp. 401–408. DOI: 10.1121/1.1916378.

Wilson, B. S. (2004). "Engineering Design of Cochlear Implants". In: *Cochlear Implants: Auditory Prostheses and Electric Hearing*. Springer New York, pp. 14–52. DOI: 10.1007/978-0-387-22585-2_2.

Wilson, B. S. and M. F. Dorman (2008). "Cochlear implants: A remarkable past and a brilliant future". In: *Hearing Research* 242.1-2, pp. 3–21. DOI: 10.1016/j.heares.2008.06.005.

Wilson, B. S., C. C. Finley, D. T. Lawson, R. D. Wolford, D. K. Eddington, and W. M. Rabinowitz (1991). "Better speech recognition with cochlear implants". In: *Nature* 352.6332, pp. 236–238. DOI: 10.1038/352236a0.

Woo, J., C. A. Miller, and P. J. Abbas (2009). "The Dependence of Auditory Nerve Rate Adaptation on Electric Stimulus Parameters, Electrode Position, and Fiber Diameter: A Computer Model Study". In: *Journal of the Association for Research in Otolaryngology* 11.2, pp. 283–296. ISSN: 1438-7573. DOI: 10.1007/s10162-009-0199-2.

Yang, H. and M. A. Xu-Friedman (2008). "Relative Roles of Different Mechanisms of Depression at the Mouse Endbulb of Held". In: *J Neurophysiol* 99.5, pp. 2510–2521. DOI: 10.1152/jn.01293.2007.

Yang, H. and M. A. Xu-Friedman (2009). "Impact of synaptic depression on spike timing at the endbulb of held." In: *Journal of neurophysiology* 102.3, pp. 1699–1710. ISSN: 0022-3077. DOI: 10.1152/jn.00072.2009.

Yang, H. and M. A. Xu-Friedman (2015). "Skipped-stimulus approach reveals that short-term plasticity dominates synaptic strength during ongoing activity." eng. In: *J Neurosci* 35.21, pp. 8297–8307. DOI: 10.1523/JNEUROSCI.4299-14.2015.

Young, E. D. and M. B. Sachs (2008). "Auditory nerve inputs to cochlear nucleus neurons studied with cross-correlation". In: *Neuroscience* 154.1, pp. 127–138. ISSN: 03064522. DOI: 10.1016/j.neuroscience.2008.01.036.

Zeng, F.-G., A. N. Popper, and R. R. Fay, eds. (2004). *Cochlear Implants: Auditory Prostheses and Electric Hearing*. Springer New York. DOI: 10.1007/978-0-387-22585-2.

Zhang, F., C. A. Miller, B. K. Robinson, P. J. Abbas, and N. Hu (2007). "Changes Across Time in Spike Rate and Spike Amplitude of Auditory Nerve Fibers Stimulated by Electric Pulse Trains". In: *Journal of the Association for Research in Otolaryngology* 8.3, pp. 356–372. ISSN: 1438-7573. DOI: 10.1007/s10162-007-0086-7.

Zilany, M. S. A., I. C. Bruce, and L. H. Carney (2014). "Updated parameters and expanded simulation options for a model of the auditory periphery." eng. In: *J Acoust Soc Am* 135.1, pp. 283–286. DOI: 10.1121/1.4837815.

Zilany, M. S. A., I. C. Bruce, P. C. Nelson, and L. H. Carney (2009). "A phenomenological model of the synapse between the inner hair cell and auditory nerve: long-term adaptation with power-law dynamics." In: *The Journal of the Acoustical Society of America* 126.5, pp. 2390–2412. ISSN: 1520-8524. DOI: 10.1121/1.3238250.